DISSERTATION | DOCTORAL THESIS

Titel | Title

Interactions of multiple particles via coherent scattering

verfasst von | submitted by

Manuel Reisenbauer BSc MSc

angestrebter akademischer Grad | in partial fulfilment of the requirements for the degree of

Doktor der Naturwissenschaften (Dr.rer.nat.)

Wien | Vienna, 2026

Studienkennzahl lt. Studienblatt | Degree programme code as it appears on the student record sheet:	UA 796 605 411
Dissertationsgebiet lt. Studienblatt | Field of study as it appears on the student record sheet:	Physik
Betreut von | Supervisor:	Univ.-Prof. Dr. Markus Aspelmeyer
Mitbetreut von | Co-Supervisor:	Dr. Uros Delic BSc MSc

INTERACTIONS OF MULTIPLE PARTICLES VIA COHERENT SCATTERING

MANUEL REISENBAUER

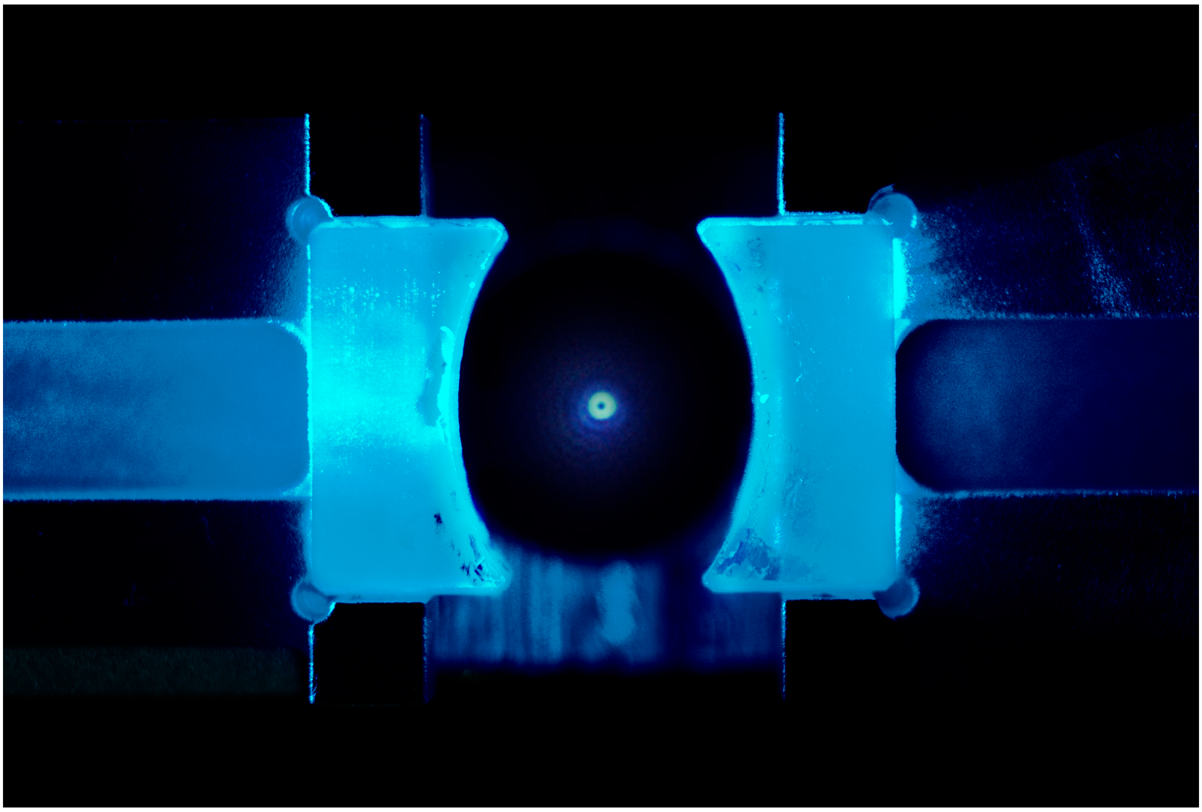

Things you can do with balls that scatter like dipoles.

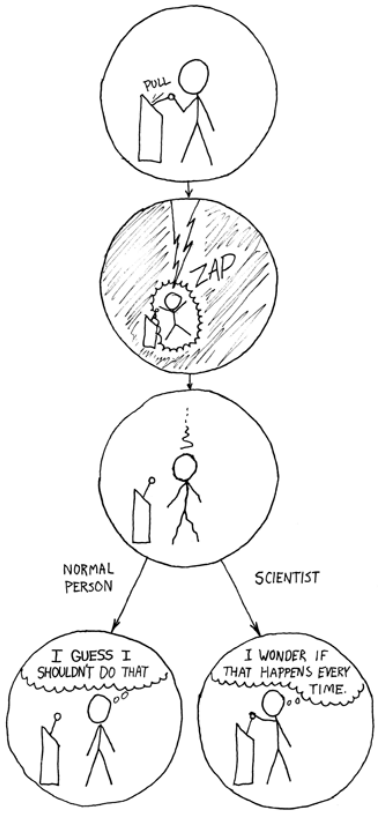

https://xkcd.com/242

Manuel Reisenbauer: *Interactions of multiple particles via coherent scattering,*
Things you can do with balls that scatter like dipoles.

Dedicated to all the particles lost to the void.
2018 – 2024

Dedicated to my mental health. I had no use for it anyways.

ABSTRACT

In the Rayleigh regime, an optically trapped dielectric nanoparticle acts as an induced electric dipole whose coherently scattered radiation depends on its center of mass motion. This dipole field can be interfaced with other systems, establishing a controllable coupling. This thesis exploits that mechanism in two complementary projects.

Part I couples a single nanoparticle to a high-finesse optical cavity via the coherent scattering interaction. Operating in the resolved sideband regime, we cool the motional along the cavity axis to its quantum ground state, preparing the ground state of a levitated nanoparticle at room temperature for the first time.

Part II interfaces the coherently scattered dipole field of one trapped nanoparticle with a second nanoparticle held in a parallel optical tweezer. The resulting light-induced dipole–dipole interaction is intrinsically nonlinear, non-reciprocal, and non-Hermitian. We observe signatures of $\mathcal{PT}$-symmetry breaking and a transition to mechanical lasing in the collective motion.

ZUSAMMENFASSUNG

Im Rayleigh Regime verhält sich ein optisch gefangenes dielektrisches Nanoteilchen als induzierter elektrischer Dipol, dessen kohärent gestreute Strahlung seine Schwerpunktsbewegung kodiert. Dieses Dipolfeld kann mit anderen Systemen gekoppelt werden und stellt so eine kontrollierbare Kopplung her. Diese Dissertation nutzt diesen Mechanismus in zwei komplementären Projekten aus.

Teil I koppelt ein einzelnes Nanoteilchen über die "coherent scattering" Interaction an eine Mode eines optischen Hohlraumstrahlers. Im seitenbandaufgelösten Regime kühlen wir die Bewegung entlang der Hohlraumstrahlerachse in den quantenmechanischen Grundzustand und erzeugen damit erstmals den Grundzustand eines levitierten Nanopartikels bei Raumtemperatur.

Teil II koppelt das kohärent gestreute Dipolfeld eines gefangenen Nanoteilchens an ein zweites Nanoteilchen, das in einer parallelen optischen Falle gehalten wird. Die resultierende lichtinduzierte Dipol-Dipol-Wechselwirkung ist intrinsisch nichtlinear, nichtreziprok und nicht-hermitesch. Wir beobachten Signaturen einer $\mathcal{PT}$- Symmetriebrechung sowie einen Übergang zu mechanischem Lasing in der kollektiven Bewegung.

ACKNOWLEDGMENTS

First and foremost, I want to thank my supervisor Markus for inspiring and motivating me through genuine enthusiasm and positivity. Some of your scientific fervor rubbed off on me, for which I am deeply grateful. I am equally grateful to my co-supervisor, Uros, who taught me much of what I know today. I hope my endless questions didn't annoy you too much. Thank you for not leaving me after only two months learning how to operate your setup.

I would like to acknowledge all my colleagues I had the pleasure to work with. Thank you to Ralph for giving me the friendship ticket. You opened the door to the Aspelmeyer group for me. Thank you, Kahan, for sharing all the gummy bears with me during the long measurement nights. You were easily the best lab partner I could have asked for (the worst quantum cup opponent however!). Thank you Yurie. Ranting with you about random topics kept me sane (mostly). Thank you to Livia and Murad. Building a completely new setup and starting a new project with you was an absolute pleasure. A special shoutout to Klemens, who saved me from a theory-induced mental break. You helped me when I needed it most, in a way no one else could, or would.

Finally thank you to Steffi. You were always there to support me when things got tough, celebrate with me when they went well, and somehow keep me sane throughout it all. You make everything in my life better. Thank you for helping me get through this chapter of my life. I would not have made it without you.

CONTENTS

1 INTRODUCTION

Quantum optomechanics studies the interaction between light and motion, combining the excellent control of optical fields established in quantum optics with mechanical oscillators. Three principal applications are typically highlighted: precision sensing, coherent transduction across frequency domains, and the use of optomechanical platforms to investigate fundamental questions in physics.

For sensing applications, the measurement precision of quantum optics, combined with the susceptibility of mechanical oscillators to forces, accelerations, and displacements, allows detection of extremely weak signals. Demonstrated applications include force sensing [50], displacement sensing [116], mass sensing [114], accelerometry [69], and magnetometry [29]. LIGO and Virgo's gravitational wave detections [1] are among the most prominent demonstrations of optomechanical sensing. Beyond these milestones, optomechanical sensors are being developed or proposed for dark matter searches [20, 88, 89], tests of short range deviations from Newton's law [11, 52], and precision probes of charge neutrality of matter and fractional charges [3, 90].

As a coherent bridge between light and mechanics, optomechanics is well suited for transduction. To date, many distinct degrees of freedom have been linked, from the motion of atoms [91] and the vibrations of membranes [124] to the center of mass motion of kg-scale mirrors [2], with electromagnetic frequencies spanning microwave to optical [46]. Because mechanical modes can interact coherently across this spectrum, they can act as intermediaries linking otherwise incompatible technologies, with potential applications in quantum computation, information processing, and communication [67].

We use optical tweezers as our optomechanical platform, which have emerged as versatile tools in physics and biology [54, 129]. By tightly focusing a laser beam, an optical tweezer creates a potential well that traps and moves polarizable objects. Near the focus, a dielectric is drawn toward the intensity maximum by the gradient force, which can dominate other forces and allows for stable trapping. In levitated optomechanics, the trap is purely optical, eliminating the need for clamping to a bulk substrate. Consequently, dissipation is dominated by scattering of trapping light and by damping due to residual background gas, the latter of which can be greatly reduced in ultrahigh vacuum. As a result, mechanical quality factors can be extremely high. Although clamped devices can also achieve high quality factors, levitated platforms provide a large dynamic range of tunable damping rates and oscillation frequencies.

Because the trapping potential is generated solely by optical fields, the potential can be engineered with high speed and precision. Nonlinear and time-dependent potentials are readily implemented [4, 27, 57, 104, 106, 140], and complex landscapes with multiple stable trapping sites can be created to confine several objects in close proximity [10, 31, 41, 138]. Such configurations enable studies of complex interactions and collective dynamics in arrays of levitated oscillators [6, 107, 128], .

The work presented in this thesis focuses on the center of mass motion of silica nanoparticles. The wavelength of the trapping light is much larger than the particle size, so the particle behaves as an induced electric dipole in the optical field, which radiates a dipole pattern. This scattering provides a versatile mechanism for coupling the nanoparticle's motion to other optical modes and degrees of freedom.

This thesis is organized into two parts, each addressing a distinct project. In both projects, the nanoparticle's dipole scattering serves as the mechanism that couples its motion to other systems. In Part i the dipole scattering is interfaced with a cavity mode, coupling the particle motion to the cavity via the coherent scattering interaction, which we use to cool the particle motion to its quantum ground state. Part ii investigates light-induced dipole–dipole interactions between two levitated nanoparticles and the resulting nonlinear, non-Hermitian collective dynamics.

Part I

CAVITY OPTOMECHANICS VIA COHERENT SCATTERING

*Do it as sh***y as you can and go back to the lab!*

— Uroš Delić

2 CAVITY OPTOMECHANICS: INTRODUCTION

In levitated cavity optomechanics, the optomechanical interaction couples the center of mass motion of a levitated oscillator to the electromagnetic field of an optical cavity. This coupling enables laser cooling of objects that lack accessible internal transitions [9]. While laser cooling has enabled the preparation of complex quantum states in atomic systems [94], extending such control to mesoscopic, levitated solids opens new opportunities for investigating fundamental questions in physics [109]. A requirement for these efforts is the preparation of a sufficiently pure initial state, the motional ground state.

While other mechanical systems have been cooled to the ground state [22, 95, 123], technical limitations have prevented this for levitated particles. Prior efforts using active feedback cooling were limited to occupancies of approximately 4 motional quanta, and cavity cooling experiments were limited to ~ 2100 motional quanta [7, 44, 66, 85, 87]. The coherent scattering interaction [21, 47, 83, 93, 131] was introduced into the field of levitated optomechanics to overcome technical challenges of dispersive cavity cooling [85], notably co-trapping and heating from laser phase noise.

In this chapter, we present the culmination of a decade-long effort: ground-state cooling of a nanoparticle's center-of-mass motion. We achieve this using resolved-sideband cooling mediated by coherent scattering in a room-temperature environment. These results provides a pathway to preparing and studying complex quantum states in the mesoscopic regime.

Since these findings were published, many more advances employing the same approach have been reported, including cooling multiple degrees of freedom of a single particle [32, 99, 103, 127] and cooling and coupling multiple particles within the same cavity mode [36].

3 THEORY FOR CAVITY LEVITATION

In this chapter, I will discuss the theory needed to understand the presented experiment. Beginning in section 3.1, I briefly introduce the quantum harmonic oscillator and the concept of sideband thermometry, which was used to verify ground state cooling. I will then discuss the properties of optical cavities in section 3.2. Section 3.3 gives an introduction to optical trapping of nanoparticles and position detection via the optical tweezer. Finally, in section 3.4, I will provide the theory for the optical interaction of a nanoparticle with a cavity via coherent scattering and give a model for the detection of the motion via the light scattered into the cavity.

3.1 SIDEBAND THERMOMETRY

Sideband thermometry provides a calibration-free estimate of the mean occupation of a harmonic oscillator in equilibrium with a thermal bath. It is independent of calibration factors as it only uses the ratio of power spectral densities. This section is meant to give basic definitions used throughout this thesis and illustrate the concept. A detailed model of the particle detection is given in a later section.

3.1.1 *Quantum Harmonic Oscillator*

Many physical systems can be approximated exceptionally well by harmonic oscillators. The excitation of a single high finesse cavity mode and small amplitude motion of a particle trapped in an optical tweezer are among such examples. The derivations in this chapter closely follow the derivation detailed in [132]. The Hamiltonian governing the dynamics of a harmonic oscillator is

$$\hat{H} = \frac{\hat{p}^2}{2m} + \frac{k\hat{x}^2}{2} \tag{1}$$

where $\hat{x}$ is the position operator, $\hat{p}$ is the momentum operator, m is the oscillators mass and $k = m\Omega^2$ is the spring constant with the oscillation frequency Ω. This equation can be rewritten using the ladder operators

$$\hat{x} = \sqrt{\frac{\hbar}{2m\Omega}}\left(a^\dagger + a\right) \tag{2}$$

$$\hat{p} = i\sqrt{\frac{\hbar m\Omega}{2}}\left(a^\dagger - a\right), \tag{3}$$

where a is the annihilation operator and $a^\dagger$ is the creation operator, into $\hat{H} = \hbar\Omega(a^\dagger a + 1/2)$. The ladder operators obey the commutation relation $[a, a^\dagger] = 1$. If one starts with a harmonic oscillator in the Fock state with n phonons $|n\rangle$, the operators add or subtract one phonon

$$a\,|n\rangle = \sqrt{n}\,|n-1\rangle \tag{4}$$

$$a^\dagger\,|n\rangle = \sqrt{n+1}\,|n+1\rangle\,. \tag{5}$$

Once all phonons are extracted from the state, it is in the ground state $|0\rangle$, with $a\,|0\rangle = 0$. When the oscillator is in thermal equilibrium with its environment, the probability $p(n)$ of finding it at energy level n is given by Bose–Einstein statistics

$$p(n) = exp\left(-\frac{\hbar\Omega n}{k_B T}\right)\left[1 - exp\left(-\frac{\hbar\Omega}{k_B T}\right)\right], \tag{6}$$

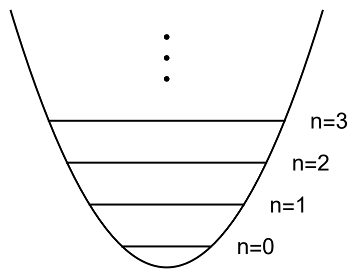

Figure 1: Harmonic oscillator energy levels are equally spaced.

where k_B is the Boltzmann constant, and T is the temperature of the environment. The mean occupation of the oscillator is this state is given by

$$\bar{n} = \sum_{n=0}^{\infty} np(n) = \left[\exp\left(\frac{\hbar\Omega}{k_B T}\right) - 1\right]^{-1}, \tag{7}$$

which can be simplified in the classical limit $k_B T \gg \hbar\Omega$ to

$$\bar{n} = \frac{k_B T}{\hbar\Omega}. \tag{8}$$

3.1.2 *Independent-Oscillator Model*

To model a system coupled to a thermal bath, we introduce a spring-like coupling to each of an ensemble of independent bath oscillators [45, 132]. The Hamiltonian for this configuration is given by

$$\hat{H} = \hat{H}_{sys} + \hat{H}_{sys-bath}, \tag{9}$$

where the the system is described by a particle in a potential $\hat{V}(\hat{x})$. The individual parts are

$$\hat{H}_{sys} = \frac{\hat{p}^2}{2m} + \hat{V}(\hat{x}) \tag{10}$$

$$\hat{H}_{sys-bath} = \sum_j \left[\frac{\hat{p}_j^2}{2m_j} + \frac{k_j}{2}(\hat{x}_j - \hat{x})^2\right], \tag{11}$$

where $\hat{p}_j, \hat{x}_j, m_j$, and k_j are momentum, position, mass, and spring constant of the j-th bath mode. From the Hamiltonian, we can derive the equations of motion

$$m\ddot{\hat{x}} = -\frac{\partial \hat{V}(\hat{x})}{\partial \hat{x}} + \sum_j k_j(\hat{x}_j - \hat{x}) \tag{12}$$

$$m_j\ddot{\hat{x}}_j = -k_j(\hat{x}_j - \hat{x}). \tag{13}$$

Inserting the general solution of the second equation into the first yields

$$m\ddot{\hat{x}} + \int_{-\infty}^{t} dt'\mu(t-t')\dot{\hat{x}}(t') + \frac{\partial \hat{V}(\hat{x})}{\partial \hat{x}} = \hat{F}(t), \tag{14}$$

where $\hat{F}(t)$ is a stochastic force and $\mu(t)$ is a memory kernel which characterizes the timescales on which the bath force loses correlations. The integral can be solved to get

$$\int_{-\infty}^{t} dt'\mu(t-t')\dot{\hat{x}}(t') = k_{bath}\hat{x}(t) + m\int_{-\infty}^{\infty} dt'\gamma(t-t')\dot{\hat{x}}(t'), \tag{15}$$

which lets us simplify equation (14) to get the quantum Langevin equation

$$m\ddot{\hat{x}} + m\int_{-\infty}^{t} dt'\gamma(t-t')\dot{\hat{x}}(t') + \frac{\partial \hat{V}(\hat{x})}{\partial \hat{x}} = \hat{F}(t). \tag{16}$$

The spring constant induced by the environment is absorbed into the potential $\hat{V}(\hat{x}) \to \hat{V}(\hat{x}) + k_{bath}\hat{x}^2$. In the limit of linear damping, one can set $\gamma(t) = \gamma\delta(t)$ and evaluate the integral to obtain the quantum Markovian Langevin equation

$$m\ddot{\hat{x}} + m\gamma\dot{\hat{x}} + \frac{\partial \hat{V}(\hat{x})}{\partial \hat{x}} = \hat{F}(t), \tag{17}$$

which generalizes to an arbitrary observable $\mathcal{O}$:

$$\dot{\hat{\mathcal{O}}} = \frac{1}{i\hbar}\left[\hat{\mathcal{O}}, \hat{H}_{sys}\right] - \frac{1}{i\hbar}\left[\hat{\mathcal{O}}, \hat{x}\right]\hat{F}(t) + \frac{m}{2i\hbar}\left\{\left[\hat{\mathcal{O}}, \hat{x}\right], \gamma\dot{\hat{x}}\right\}, \tag{18}$$

where $\{a, b\} = ab + ba$ is the anticommutator. By using the Hamiltonian from equation (1), we retrieve the equations of motion for the harmonic oscillator

$$\dot{\hat{Q}} = \Omega\hat{P} \tag{19}$$
$$\dot{\hat{P}} = -\Omega\hat{Q} - \gamma\hat{P} + \sqrt{2\gamma}\hat{P}_{in}, , \tag{20}$$

where the dimensionless position and momentum operators are introduced

$$\hat{Q} = \sqrt{\frac{m\Omega}{\hbar}}\hat{x} = \frac{1}{\sqrt{2}}\left(a^\dagger + a\right) \tag{21}$$
$$\hat{P} = \sqrt{\frac{1}{\hbar m\Omega}}\hat{p} = \frac{i}{\sqrt{2}}\left(a^\dagger - a\right), \tag{22}$$

and the stochastic force is expressed via the input momentum

$$\hat{P}_{in}(t) = \frac{i}{\sqrt{2}}\left(a_{in}^\dagger(t) - a_{in}(t)\right) = \frac{\hat{F}(t)}{\sqrt{2m\Omega\hbar\gamma}}. \tag{23}$$

Combining equation (19) and (20) yields the equation for the position

$$\ddot{\hat{Q}} + \gamma\dot{\hat{Q}} + \Omega^2\hat{Q} = \sqrt{2\gamma}\Omega\hat{P}_{in}, \tag{24}$$

which is easily solved in Fourier space

$$\hat{Q}(\omega) = \sqrt{2\gamma}\chi(\omega)\hat{P}_{in}(\omega), \tag{25}$$

where $\chi(\omega)$ is the mechanical susceptibility defined by

$$\chi(\omega) = \frac{\Omega}{\Omega^2 - \omega^2 - i\omega\gamma}. \tag{26}$$

The susceptibility quantifies how strong the oscillator will respond to external forcing at frequency ω.

3.1.3 *Fluctuation-Dissipation Theorem and Power Spectral Density*

We have now simplified a system coupled to an ensemble of bath modes to a system with damping γ and a force by the environment $\hat{F}(t)$ [18, 19]. For systems in thermal equilibrium with a bath at temperature T, the fluctuation-dissipation theorem establishes a link between the random force $\hat{F}(t)$ acting on the system and the dissipation γ. In the classical limit, it is given by [70]

$$S_{FF}(\omega) = 2\gamma m k_B T, \tag{27}$$

where $S_{FF}(\omega)$ is the power spectral density of the force. For a classical complex variable $h(t)$ the power spectral density is defined by

$$S_{hh}(\omega) = \lim_{\tau\to\infty} \frac{1}{\tau} \langle h_\tau^*(\omega) h_\tau(\omega) \rangle, \tag{28}$$

where $h_\tau(\omega)$ is the windowed Fourier of $h(t)$ defined by

$$h_\tau(\omega) = \int_{-\tau/2}^{\tau/2} h(t) e^{i\omega t} dt. \tag{29}$$

The (non-windowed) Fourier transform is recovered for $\tau \to \infty$. Using the Wiener–Khinchin theorem [24], one gets a relation between the Fourier transform and the auto correlation function

$$S_{hh}(\omega) = \int_{-\infty}^{\infty} d\tau e^{i\omega\tau} \langle h^*(t+\tau) h(t) \rangle_{t=0} = \int_{-\infty}^{\infty} d\omega' \left\langle h^*(-\omega) h(\omega') \right\rangle. \tag{30}$$

The power spectral density can be generalized to a quantum operator $\mathcal{O}$

$$S_{\mathcal{O}\mathcal{O}}(\omega) = \lim_{\tau\to\infty} \frac{1}{\tau} \left\langle \hat{\mathcal{O}}_\tau^\dagger(\omega) \hat{\mathcal{O}}_\tau(\omega) \right\rangle, \tag{31}$$

which can again be related to the autocorrelation function using the Wiener–Khinchin theorem

$$\begin{aligned} S_{\mathcal{O}\mathcal{O}}(\omega) &= \int_{-\infty}^{\infty} d\tau e^{i\omega\tau} \left\langle \hat{O}^{\dagger}(t+\tau)\hat{O}(t) \right\rangle_{t=0} \\ &= \int_{-\infty}^{\infty} d\omega' \left\langle \hat{O}^{\dagger}(-\omega)\hat{O}(\omega') \right\rangle \end{aligned} \quad (32)$$

$$\begin{aligned} S_{\mathcal{O}^{\dagger}\mathcal{O}^{\dagger}}(\omega) &= \int_{-\infty}^{\infty} d\tau e^{i\omega\tau} \left\langle \hat{O}(t+\tau)\hat{O}^{\dagger}(t) \right\rangle_{t=0} \\ &= \int_{-\infty}^{\infty} d\omega' \left\langle \hat{O}(\omega)\hat{O}^{\dagger}(\omega') \right\rangle . \end{aligned} \quad (33)$$

A major difference to the classical case is that the operators do not commute in general $\left[\hat{O}^{\dagger}(t+\tau), \hat{O}(t)\right] \neq 0$, which has the consequence that the power spectral density is not symmetric in general $S_{\mathcal{O}\mathcal{O}}(\omega) \neq S_{\mathcal{O}\mathcal{O}}(-\omega)$.

3.1.4 *Sideband Thermometry*

We want to establish a connection between the power spectral density of the particle position S_{QQ} and its mean occupation $\bar{n}$. We look at a simplified version of the Hamiltonian presented in the last chapter [132]

$$\hat{H} = \hat{H}_0 + \hat{q}\hat{F} \quad (34)$$

where $\hat{H}_0$ is the bare Hamiltonian $\hat{H}_0 = \hbar\Omega a^{\dagger} a + \hat{H}_{bath}$, $\hat{H}_{bath}$ is the Hamiltonian of the thermal bath and $\hat{F}$ is the random force exerted from the thermal bath. The force can cause the oscillator to jump one energy level up from $|n\rangle$ to $|n+1\rangle$. The probability $P_{n\to n+1}$ that this transition happens can be calculated using first-order perturbation theory [28]. The initial state is assumed to be separable $|\psi(0)\rangle = |\psi_{sys}(0)\rangle \otimes |\psi_{bath}\rangle$ and the interaction is assumed to be weak enough that it stays separable during the whole time evolution. Since the bath modes are typically not accessible, we sum over them to get the probability

$$P_{n\to n+1} = \frac{x_{zp}^2(n+1)}{\hbar^2} \int\int_0^t d\tau_1 d\tau_2 e^{i\Omega(\tau_2-\tau_1)} \left\langle \hat{F}(\tau_1)\hat{F}(\tau_2) \right\rangle . \quad (35)$$

The upward-going transition rate is the derivative of the transition probability and given by

$$\gamma_{n\to n+1} = \frac{x_{zp}^2}{\hbar^2}(n+1)S_{FF}(-\Omega), \quad (36)$$

where the autocorrelation of the force is rewritten as the power spectral density S_{FF}. The downward-going transition rate can be obtained in an analogous way

$$\gamma_{n\to n-1} = \frac{x_{zp}^2}{\hbar^2} n S_{FF}(\Omega). \quad (37)$$

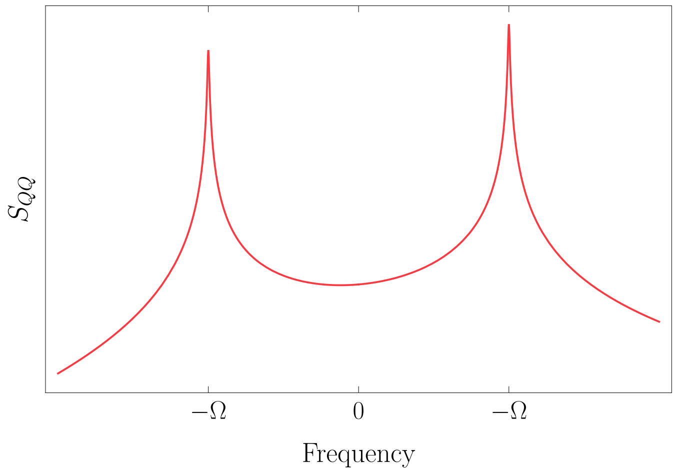

Figure 2: Power spectral density $S_{QQ}(\omega)$ plotted for positive and negative frequencies. The asymmetry of the sidebands at $-\Omega$ and Ω can be used to determine the oscillators mean occupation.

For an oscillator in thermal equilibrium with its environment, the total rate at which it gains energy and loses energy must be the same according to the concept of detailed balance. For a harmonic oscillator in thermal equilibrium, the transition from level n to $n+1$, and vice versa, must satisfy

$$p(n)\gamma_{n\to n+1} = p(n+1)\gamma_{n+1\to n}, \tag{38}$$

where $p(n)$ is the probability of finding the oscillator in level n. Using Equations (6), (7), (36), and (37), one gets a relation between the power spectral densities of the force $\hat{F}$ and the mean occupation number

$$\frac{S_{FF}(\Omega)}{S_{FF}(-\Omega)} = 1 + \frac{1}{\bar{n}}. \tag{39}$$

With this result, we can revisit the position of a harmonic oscillator, as given in Equation (25). The power spectral density $S_{QQ}(\omega)$ is plotted in Figure 2. The values at the sideband frequencies $\pm\Omega$ are given by

$$S_{QQ}(\Omega) = 2\gamma\,|\chi(\Omega)|^2\, S_{P_{in}P_{in}}(\Omega) \tag{40}$$

$$S_{QQ}(-\Omega) = 2\gamma\,|\chi(-\Omega)|^2\, S_{P_{in}P_{in}}(-\Omega), \tag{41}$$

where the input momentum is given in Equation (23). We can finally rewrite the ratio of the sidebands as

$$\frac{S_{QQ}(\Omega)}{S_{QQ}(-\Omega)} = \frac{|\chi(\Omega)|^2}{|\chi(-\Omega)|^2}\frac{S_{P_{in}P_{in}}(\Omega)}{S_{P_{in}P_{in}}(-\Omega)} = \frac{|\chi(\Omega)|^2}{|\chi(-\Omega)|^2}\frac{\bar{n}+1}{\bar{n}}. \tag{42}$$

Since $|\chi(\omega)|$ is symmetric in ω, one retrieves the same result as given in Equation (39), expressed through the power spectral density of the position. The concept presented here provides a method for measuring the mean occupation of a thermal harmonic oscillator. Because it only depends on the ratio of the power spectral density, evaluated at the two sidebands $\pm\Omega$, it is independent of a proper calibration of the spectrum. This principle is applied in the experiment of Chapter 4, where the mechanical motion is indirectly measured via an optical cavity. Section 3.4.2 presents the theoretical model for the cavity detection.

3.2 OPTICAL CAVITY THEORY

This section introduces the theory for optical cavities in a near-confocal symmetrical configuration, focusing on the relevant parameter regime. In Section 3.2.1, I derive the quantum Langevin equation for a single driven cavity mode. Then, in Section 3.2.2, I discuss the classical optical properties of such cavities to motivate the single-mode treatment.

3.2.1 *Quantum Description*

To get a quantum description of the cavity field, one associates a quantum harmonic oscillator with each mode [79]. The total cavity field is the sum over all supported modes. For a near-confocal, high finesse cavity, the modes are spatially and spectrally well separated, a motivation for which will be provided in the next section. We focus on a single TEM_{00} cavity mode with resonance frequency ω_{cav}. The electric field of that mode can be expressed as $\mathbf{E}_{cav} = \mathbf{E}^+ + \mathbf{E}^-$ with

$$\mathbf{E}^+ = \sqrt{\frac{\hbar\omega_{cav}}{2\varepsilon_0 V_{cav}}} f(\mathbf{r})\mathbf{e}_p \hat{a} e^{-i\omega_{cav}t}, \tag{43}$$

$$\mathbf{E}^- = \sqrt{\frac{\hbar\omega_{cav}}{2\varepsilon_0 V_{cav}}} f^*(\mathbf{r})\mathbf{e}_p \hat{a}^\dagger e^{i\omega_{cav}t}, \tag{44}$$

where ε_0 is the vacuum permittivity, V_{cav} is the cavity mode volume, $f(\mathbf{r})$ is the cavity mode function (the normalized classical electric field), and $\mathbf{e}_p$ is the polarization vector. The magnetic field is given by $\mathbf{B}_{cav} = \mathbf{B}^+ + \mathbf{B}^-$ with

$$\mathbf{B}^\pm = \frac{1}{\omega_{cav}} \mathbf{k} \times \mathbf{E}^\pm. \tag{45}$$

The Hamiltonian can be constructed in an analogous way to the classical one by

$$H_{cav} = \frac{1}{2}\int_V dV \left[\varepsilon_0 E_{cav}\cdot E_{cav} + \frac{1}{\mu_0} B_{cav}\cdot B_{cav}\right] = \hbar\omega_{cav}(\hat{a}^\dagger\hat{a} + \frac{1}{2}). \tag{46}$$

Interaction with an environment is modeled by adding free modes H_B and an interaction term H_{int}, which are given by [49]

$$\begin{aligned} H &= H_{cav} + H_B + H_{int} && (47)\\ H_B &= \hbar \int_{-\infty}^{\infty} d\omega \omega c^\dagger(\omega) c(\omega) && (48)\\ H_{int} &= i\hbar \int_{-\infty}^{\infty} d\omega \sqrt{\frac{\kappa(\omega)}{2\pi}} \left(c^\dagger(\omega) a - a^\dagger c(\omega) \right). && (49) \end{aligned}$$

The thermal bath H_B is modeled by an infinite sum of harmonic oscillators with annihilation operators $c(\omega)$, which obey

$$[c(\omega), c^\dagger(\omega')] = \delta(\omega - \omega'). \tag{50}$$

The coupling of the bath to the system is given by $\kappa(\omega)$. We can derive and solve the Heisenberg equations of motion for $c(\omega)$ and a to get the Langevin equation

$$\dot{a} = -i\omega_{cav} a - \frac{\kappa}{2} a - \sqrt{\kappa} c_{in}(\omega), \tag{51}$$

where the first Markov approximation was used, which makes the coupling $\kappa(\omega) = \kappa$ frequency independent. The input field is defined by

$$c_{in}(t) = \frac{1}{\sqrt{2\pi}} \int d\omega e^{-i\omega(t-t_0)} c_0(\omega), \tag{52}$$

which satisfies the commutation relation $[c_{in}(t), c_{in}^\dagger(t')] = \delta(t - t')$, and $c_0 = c(t_0)$. A second solution of the equations of motion including output fields can be found and is given by

$$\dot{a} = -i\omega_{cav} a + \frac{\kappa}{2} a - \sqrt{\kappa} c_{out}(t), \tag{53}$$

where the output field is defined by

$$c_{out}(t) = \frac{1}{\sqrt{2\pi}} \int d\omega e^{-i\omega(t-t_1)} c_1(\omega). \tag{54}$$

The input and output fields are linked by the identity

$$c_{out}(t) - c_{in}(t) = \sqrt{\kappa} a(t). \tag{55}$$

While these fields are typically treated as vacuum states at optical frequencies, a cavity driven by a strong laser is more accurately modeled with a high-amplitude coherent state as the input. The cavity drive is formally introduced into the Hamiltonian (47) by applying the displacement operator $D(\alpha_D(t)) = \exp(\alpha_D(t) c^\dagger(\omega_D) - \alpha^*(t) c(\omega_D))$.

The driven Hamiltonian H^D in a frame rotating with the coherent drive is given by

$$\begin{aligned} H^D &= \hbar\omega_{cav}\left(a^\dagger a + \frac{1}{2}\right) - \hbar\omega_D a^\dagger a \quad (56) \\ &+\hbar\int d\omega(\omega-\omega_D)c^\dagger(\omega)c(\omega) \\ &+i\hbar\int d\omega\sqrt{\frac{\kappa}{2\pi}}\left(c^\dagger(\omega)a - a^\dagger c(\omega)\right) \\ &+i\hbar E_D\left(a - a^\dagger\right), \quad (57) \end{aligned}$$

where the cavity drive $E_D = \sqrt{P_{in}\kappa_{in}/\hbar\omega_D}$ is given by the power of the incident laser P_{in}, and κ_{in} quantifies the coupling of the drive mode to the cavity mode. From the Hamiltonian, we can derive the Langevin equation for the driven cavity mode

$$\dot{a} = -i\Delta a - \frac{\kappa}{2}a - \sqrt{\kappa}c_{in} - E_D. \quad (58)$$

The external modes $c(\omega)$ include both accessible channels, such as light transmitted through the mirrors, and inaccessible ones, such as light scattered or absorbed within the cavity. It can be useful to separate these modes and define distinct couplings, such that $\kappa = \kappa_{in} + \kappa_0$.

3.2.2 *Optical Properties*

To motivate the single mode treatment of the previous section and give an expression for the cavity mode function, I provide classical theory for optical cavities. The theory focuses on a symmetric, near-confocal cavity, which is the configuration used in the presented experiment. The cavity consists of two spherical mirrors with radii of curvature $R_1 = R_2 = R$ and reflectivities $r_1 = r_2 = r$, separated by a distance of $L \geqslant R$. The modes supported by this configuration are Hermite-Gaussian beams. The electric field inside the cavity is given by [133]

$$\begin{aligned} E(x,y,z) = \frac{2E_0 w_0}{w(z)}\exp\left(-\frac{x^2+y^2}{w^2(z)}\right)H_m\left(\frac{\sqrt{2}x}{w(z)}\right)H_n\left(\frac{\sqrt{2}y}{w(z)}\right) \\ \times\exp\left(-i(m+n+1)\arctan\left(\frac{z}{z_0}\right)\right)\cos\left(kz+\frac{k(x^2+y^2)}{2R(z)}\right), \quad (59) \end{aligned}$$

which leads to an intensity distribution

$$\begin{aligned} I(x,y,z) = |E|^2 = \frac{4E_0^2 w_0^2}{w^2(z)}\exp\left(-\frac{2(x^2+y^2)}{w^2(z)}\right)H_m^2\left(\frac{\sqrt{2}x}{w(z)}\right) \\ \times H_n^2\left(\frac{\sqrt{2}y}{w(z)}\right)\cos^2\left(kz+\frac{k(x^2+y^2)}{2R(z)}\right), \quad (60) \end{aligned}$$

with the order of the mode given by the indices m, n of the Hermite polynomial $H_m(x)$. The fundamental mode is the Gaussian beam with $m = n = 0$, i.e., the TEM_{00} mode. The functions $w(z)$ and $R(z)$ are the beam size and the radius of curvature of the wave fronts of the Gaussian beam at position z. They are given by

$$w(z) = w_0 \sqrt{1 + \left(\frac{z}{z_0}\right)^2}, \tag{61}$$

$$R(z) = z \left[1 + \left(\frac{z_0}{z}\right)^2\right]. \tag{62}$$

The beam waist is w_0 and the Rayleigh range is given by

$$z_0 = \frac{\pi w_0^2}{\lambda}. \tag{63}$$

The argument of the last exponential in Equation (59) is the Gouy phase. For the TEM_{00} mode it is

$$\zeta(z) = \arctan\left(\frac{z}{z_0}\right). \tag{64}$$

The resonance frequency of each mode is determined by the length of the cavity and the Gouy phase

$$\nu_{qnm} = \frac{c}{2L}\left(q + \frac{(m+n+1)}{\pi}\Delta\zeta\right), \tag{65}$$

where the Gouy phase difference $\Delta\zeta$ for the symmetric cavity is

$$\Delta\zeta = 2\arctan\left(\frac{L}{2R - L}\right). \tag{66}$$

Two adjacent modes with the same order (i.e., with the same m and n) are separated by the free spectral range (FSR), which is given by

$$\nu_{FSR} = \frac{c}{2L}, \tag{67}$$

where c is the speed of light. For a confocal cavity $(L = R)$, all modes satisfying $m + n = \text{odd}$ have a degenerate resonance frequency, while all modes satisfying $m + n = \text{even}$ share another. This degeneracy is lifted in the near-confocal configuration $L > R$. Each resonance has a linewidth κ given by the losses of the cavity. Losses can be introduced by absorption inside the cavity, transmission through the cavity end mirrors, and scattering out of the cavity mode. For a high finesse cavity $\mathcal{F} \gg 1$, the linewidth is given by

$$\kappa = 2\pi\frac{\nu_{FSR}}{\mathcal{F}}, \tag{68}$$

where $\mathcal{F} = \pi\sqrt{|r|}/(1 - |r|)$. The mode volume V_{cav} of the cavity is a

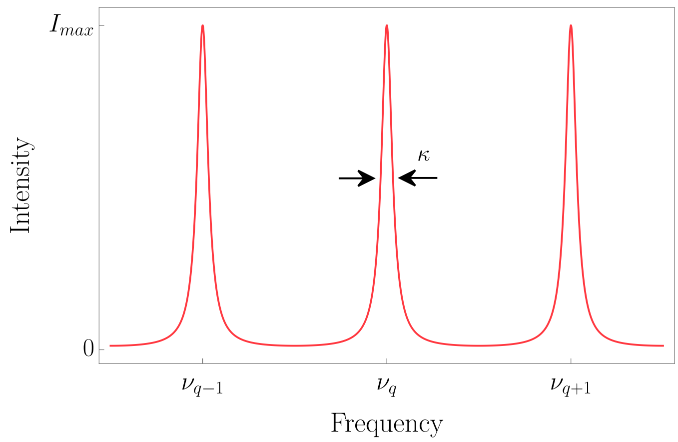

Figure 3: Mode structure of the fundamental cavity modes. Individual modes are spaced by one free spectral range ν_{FSR}. Each resonance has a linewidth of κ.

measure for the extent of a cavity mode normalized to its intensity and can be calculated by

$$V_{cav} = \int_V \frac{I(x, y, z)}{I_{max}} dV, \tag{69}$$

where $I(x, y, z) = |E(x, y, z)|^2$ is the intensity of the cavity mode and I_{max} is its maximum. The integration is done over the full volume that is occupied by the cavity mode.
The polarization of the cavity mode was ignored in the discussion above. It was assumed that the electric field aligns with the polarization of the cavity modes. Generally, the orthogonal polarization will also be supported by the cavity. Due to birefringence, the optical properties of the mirrors can be different for light with orthogonal polarization. This can affect the reflectivities of the mirrors and the optical length of the cavity. Therefore, the resonance frequencies, the free spectral range, and the cavity linewidth can be slightly shifted.

3.3 OPTICAL TRAPPING

Optical tweezers are a successful tool across many applications and research fields [54, 100]. This section treats the specific case of levitating sub-wavelength dielectric particles in vacuum. Stable trapping arises from two main contributions. First, the electromagnetic field provides a trapping potential and a non-conservative scattering force. Second, collisions with the surrounding gas create a thermal bath, which prevents the particle motion from heating up. While electrostatic forces represent a third potential interaction channel, they are ignored in this description because the particles are typically discharged before the experiment or carry too few charges to have a measurable effect. In this section, I will first cover the tight focusing of a Gaussian laser beam, then make a harmonic approximation of the trapping potential. I then discuss various heating and damping mechanisms before discussing methods for detecting the particle's motion using the tweezer light.

3.3.1 *Tight Focusing*

In this section, we consider a dielectric ball in a tightly focused laser beam. The radius of the dielectric is assumed to be much smaller than the wavelength, $a \ll \lambda$, of the illuminating field $\mathbf{E}$. In this case, the field induces a dipole moment $\mathbf{p}$ in the material. The field interacts with the dipole to generate the cycle-averaged force on the particle [92]

$$\langle \mathbf{F} \rangle = \frac{\alpha'}{2} \sum_i \mathrm{Re}\left[\underline{E}_i^* \nabla \underline{E}_i\right] + \frac{\alpha''}{2} \sum_i \mathrm{Im}\left[\underline{E}_i^* \nabla \underline{E}_i\right], \tag{70}$$

where the sum is taken over $i = x, y, z$, $\underline{\mathbf{E}}$ is the complex amplitude of the field, and $\langle \cdot \rangle$ denotes the time average. The polarizability $\alpha = \alpha' + i\alpha''$ is assumed to be frequency independent. For the induced dipole of a spherical dielectric, it is given by

$$\alpha = \alpha_0 \left(1 - i\frac{k^3}{6\pi\varepsilon_0}\alpha_0\right), \quad \text{with} \tag{71}$$

$$\alpha_0 = 3V\varepsilon_0 \frac{\varepsilon_p - \varepsilon_m}{\varepsilon_p + 2\varepsilon_m}, \tag{72}$$

where $k = 2\pi/\lambda$, ε_0 is the vacuum permittivity, ε_p is the relative permittivity of the dielectric particle, $\varepsilon_m = 1$ is the relative permittivity of the surrounding medium, which is assumed to be vacuum, and the volume of the particle is given by V. The first term of the force given in Equation (70) arises due to the gradient of the field and can be rewritten as $\langle \mathbf{F}_{grad} \rangle = (\alpha'/4)\nabla(\underline{\mathbf{E}}^* \cdot \underline{\mathbf{E}})$. This is called the gradient force and can be associated with a potential. It points toward the local maximum of the intensity distribution of the electric field. The second term cannot be associated with a potential but with a momentum transfer from the electromagnetic field to the particle. For fields with uniform helicity, it can be rewritten as $\langle \mathbf{F}_{scatt} \rangle = \sigma/c \langle \mathbf{S} \rangle$, where $\sigma = \alpha'' k/\varepsilon_0$ is the absorption cross-section and $\langle \mathbf{S} \rangle$ is the averaged Poynting vector. It is called the scattering force and points in the direction of propagation of the illuminating field. In order to have a stable trapping configuration, the gradient force must overcome the scattering force. In a single beam tweezer trap, high gradients along beam propagation can be achieved by tightly focusing a laser beam. A simple treatment using Gaussian optics is not possible, since the

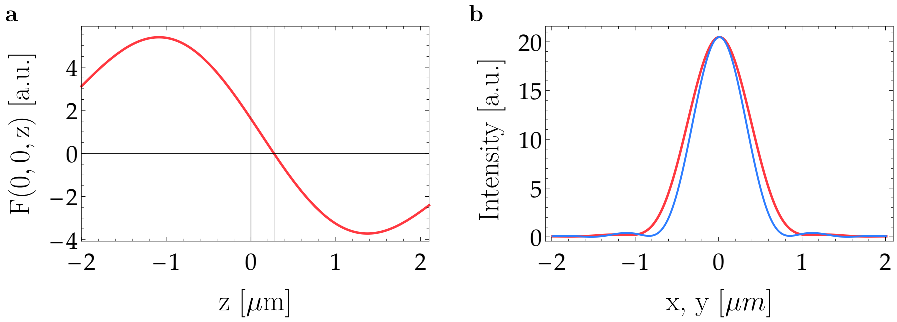

Figure 4: a. Force along z direction on the optical axis ($x = y = 0$). The scattering force shifts the stable trapping position from the beam waist at $z = 0$ to $z = z_{eq}$. **b.** Intensity distribution $|E(x, 0, z_{eq})|^2$ (red) and $|E(0, y, z_{eq})|^2$ (blue) along x and y direction in the plane of $z = z_{eq}$. Due to strong focusing the width of the distribution is different along and across the polarization of the input beam.

paraxial approximation cannot be made. The electric field distribution near the focus of an aplanatic lens can be calculated to be [92]

$$\mathbf{E}(\rho, \varphi, z) = -\frac{ikf}{2} E_0 e^{-ikf} \begin{bmatrix} I_{00} + I_{02}\cos(2\varphi) \\ I_{02}\sin(2\varphi) \\ -2iI_{01}\cos(\varphi) \end{bmatrix}. \tag{73}$$

The distance ρ and angle φ are defined by $x = \rho\cos\varphi$ and $y = \rho\sin\varphi$, k is the wavenumber, f is the focal length of the lens, and I_{00}, I_{01}, and I_{02} are defined in Equations (308), (309) and (310) in Appendix E. In this configuration, the average scattering force will point in the positive z direction only and shift the stable trapping position away from the focal point to $z = z_{eq}$. The calculated force for a spherical silica nanoparticle of radius $r = 105$ nm trapped by a Gaussian beam with waist of $w_0 = 4$ mm by a lens with NA $= 0.77$ and $f = 3.1$ mm is shown in Figure 4 together with the intensity distribution along the x and y directions in the trapping plane $z = z_{eq}$. Near the focus, the initial rotational symmetry of the input Gaussian beam is broken. The width of the intensity distribution along and across the direction of polarization of the input beam is non-degenerate. The intensity distribution is also no longer Gaussian. Side maxima emerge, which do not disturb the trapping of one particle but may introduce significant trap overlap when placing multiple traps close to each other.

3.3.2 *Harmonic Approximation*

For small displacements from the equilibrium position, $\rho, z \ll k$, the local trapping potentials can be approximated by harmonic potentials. The scattering force will be ignored for the following discussion, since it adds only a tiny correction to the stiffness of the harmonic potential. In the harmonic approximation, we aim to express the trapping potential as

$$U_h(x,y,z) = \frac{m}{2}\left(\Omega_x^2 x^2 + \Omega_y^2 y^2 + \Omega_z^2 z^2\right) \quad (74)$$

$$\approx -\frac{\alpha'}{4}\left(\mathbf{E}^* \cdot \mathbf{E}\right). \quad (75)$$

Details of the calculation can be found in Appendix E. The potential simplifies to

$$\begin{aligned} U_h(x,y,z) = -\frac{\alpha'}{4}\frac{P_0 k^2 f^2}{\varepsilon_0 c \pi w_0^2}\Big[&\left({i_{00}^{z}}^2 + 2 i_{00} i_{00}^{zz}\right) z^2 \\ &+ \left(2 i_{00} i_{00}^{\rho\rho} - 2 i_{00} i_{02}^{\rho\rho}\right) y^2 \\ &+ \left(2 i_{00} i_{00}^{\rho\rho} + 2 i_{00} i_{02}^{\rho\rho} + 4 {i_{01}^{\rho}}^2\right) x^2\Big], \end{aligned} \quad (76)$$

where all higher order and mixed terms were omitted. The electric field was replaced by the incident power of a Gaussian beam $|E_0|^2 = 4P_0/(\varepsilon_0 c \pi w_0^2)$. The definitions of the integrals i_{00}^{z}, i_{00}, i_{00}^{zz}, $i_{00}^{\rho\rho}$, $i_{02}^{\rho\rho}$, and i_{01}^{ρ} can be found in Appendix E. We can read off the oscillation frequencies for the respective center of mass motion as

$$\Omega_x = \frac{kf}{w_0}\sqrt{-\frac{\alpha'}{m}\frac{P_0}{\varepsilon_0 c \pi}\left(i_{00} i_{00}^{\rho\rho} + i_{00} i_{02}^{\rho\rho} + 2 {i_{01}^{\rho}}^2\right)}, \quad (77)$$

$$\Omega_y = \frac{kf}{w_0}\sqrt{-\frac{\alpha'}{m}\frac{P_0}{\varepsilon_0 c \pi}\left(i_{00} i_{00}^{\rho\rho} - i_{00} i_{02}^{\rho\rho}\right)}, \quad (78)$$

$$\Omega_z = \frac{kf}{w_0}\sqrt{-\frac{\alpha'}{2m}\frac{P_0}{\varepsilon_0 c \pi}\left({i_{00}^{z}}^2 + 2 i_{00} i_{00}^{zz}\right)}. \quad (79)$$

For an effective numerical aperture of $NA_{eff} = 0.7$, this gives frequencies of $(\Omega_x, \Omega_y, \Omega_z)/2\pi = (287.1, 305.6, 72.2)$ kHz, which match the measured oscillation frequencies. The root-mean-square displacement for a particle in a harmonic trap is given by

$$i_{rms} = \sqrt{\frac{2 k_B T}{m \Omega_i^2}} \quad \text{, for } i = x, y, z, \quad (80)$$

which, for the above parameters and a bath temperature of $T = 300$ K, is $(x_{rms}, y_{rms}, z_{rms}) = (19, 18, 75)$ nm. The error made by the harmonic approximation on the force acting on the particle for these displacements is less than 3% compared to the full calculation. Especially, once the particle motion is cooled, the harmonic approximation is valid.

3.3.3 *Heating and Damping Mechanisms*

In the previous section, we have approximated the trapped particle by a damped, driven harmonic oscillator. In typical levitation experiments, the total damping and heating rates arise from various sources, including classical laser intensity noise, physical shaking of the trap [115], and black-body radiation [23]. Laser phase noise may lead to heating when it is coupled to the motion via a cavity [38, 85, 102]. In this section, I will discuss heating and damping originating from the surrounding gas and photon recoil in more detail.

GAS: The center of mass motion of the trapped particle can be modeled by a driven, damped harmonic oscillator whose equaion of motion is given by Equation (17)

$$m\ddot{x} + m\gamma\dot{x} + m\Omega_x^2 x = F_{th}(t). \tag{81}$$

At higher pressures the damping rate γ and the fluctuating force $F_{th}(t)$ are dominated by effects from collisions with background gas molecules. In the regime where the mean free path of the gas molecules is larger than the radius of the particle, the gas collision contribution can be described by [23, 42]

$$\gamma_{gas} = \frac{16}{\pi}\frac{p}{v_{gas} r \rho}, \tag{82}$$

where p is the pressure of the background gas, ρ is the density of the trapped sphere, and the mean speed of the gas molecules is $v_{gas} = 8k_B T_{gas}(\pi m_{gas})$, with the temperature T_{gas} and the molecular mass m_{gas} of the gas. Some care needs to be taken when considering the temperature of the thermal bath provided by the surrounding gas. Due to a residual imaginary part in the particle's permittivity ϵ, some light is absorbed by the material, which leads to an increase of its internal temperature T_{int} [23]. A gas molecule impinging on the particle has an initial temperature T_{im}. When it hits the particle, some energy is exchanged from the surface of the particle with the molecule, increasing the molecule's temperature. Finally, the molecule will emerge from the particle with a higher temperature T_{em}. One can use a two-bath model to describe this interaction [58, 86], where one finds an effective center-of-mass temperature T_{CM} and damping coefficient γ_{CM}

$$T_{CM} = \frac{T_{im}\gamma_{im} + T_{em}\gamma_{em}}{\gamma_{em} + \gamma_{im}} \tag{83}$$

$$\gamma_{CM} = \gamma_{im} + \gamma_{em}. \tag{84}$$

Here, γ_{im} and γ_{em} are the damping coefficients associated with the thermal bath given by the impinging gas molecules and emerging gas molecules, respectively.

PHOTON RECOIL: The recoil of the fluctuating number of photons in the trapping light adds a damping rate γ_{recoil} and a heating rate Γ_{recoil} of [61–64, 108]

$$\gamma^i_{recoil} = \xi_i \frac{4}{5}\frac{\hbar k^2 r_0}{m\omega}, \tag{85}$$

$$\Gamma^{i}_{recoil} = \frac{\xi_i}{10} \frac{P_{scatt}\omega_0}{mc^2\Omega_i}, \tag{86}$$

where the magnitude depends on the direction of motion $i = (x, y, z)$ via the factor $\xi_i = (1, 2, (2 + A))$, where A is an additional contribution for a scatterer polarized by a traveling wave [121]. The wavenumber of the scattered photons is given by $k = \omega/c$, the mass of the particle is m, and r_0 is given by

$$r_0 = \frac{P_0}{3\pi^2 w_0} \frac{\alpha_0^2\omega^3}{\hbar\varepsilon_0^2 c^4}. \tag{87}$$

The total power of the incoming Gaussian laser beam is given by P_0, its waist is w_0, and α_0 is the polarizability of the particle given in Equation (72). The total scattered power is $P_{scatt} = \sigma(\omega)I_0$, and the scattering cross section is $\sigma(\omega) = k^4\alpha_0^2/(6\pi\varepsilon_0^2)$. The recoil heating rate can become dominant for low enough pressures.

3.3.4 *Tweezer detection*

In this section, I will discuss the detection of the center of mass of the levitated nanoparticle and present the two commonly used methods in optical levitation. The discussion closely follows the results presented in [121].

FORWARD DETECTION: In the Rayleigh approximation, the particle is assumed to be a point dipole trapped in a tightly focused Gaussian beam. The scattered light by the dipole in the far field can be approximated by

$$\mathbf{E}_{sc}(\mathbf{r}) = \mathbf{E}_{dip}(\mathbf{r}) \exp\left[-ik(\mathbf{r}_0\mathbf{n}_r - Az_0)\right], \tag{88}$$

where $\mathbf{E}_{dip}$ is the field radiated by a dipole at the origin, and the factor A is only dependent on the numerical aperture of the trapping lens. The phase of the scattered field is linearly dependent on the particle's position, which can be measured by an interferometer. The ideal measurement would involve interfering this scattered field with a perfectly mode-matched local oscillator, which would achieve the Heisenberg limit for all spatial modes. In practice, this is unfeasible since the scattered power is distributed into the full solid angle $d\Omega$ according to

$$dp_{dip} = \frac{3}{8\pi} P_{dip}(1 - \sin^2\theta\cos^2\theta)d\Omega, \tag{89}$$

where P_{dip} is the total scattered power. A more practical approach is forward tweezer detection, where a lens recollimates the forward-scattered light and the transmitted trapping light. Their interference is measured by a quadrant photodetector. The power on each quadrant is

$$P_1^Q = P_{inc}\frac{\pi}{4}NA_{cl}^2 + k\sqrt{\frac{3P_{inc}P_{dip}}{2\pi}}\mathbf{B}^{fw}\mathbf{r}_0, \tag{90}$$

where P_{inc} is the power of the incoming trapping light, NA_{cl} is the numerical aperture of the collimation lens, and $\mathbf{B}^{fw}$ is given by

$$\mathbf{B}^{fw} = \int_0^{\theta_{cl}} d\theta \sin\theta \sqrt{\cos\theta} \begin{pmatrix} \sin\theta(1+2\cos\theta)/3 \\ \sin\theta(2+\cos\theta)/3 \\ \pi(\cos\theta - A)(1+\cos\theta)/4 \end{pmatrix}. \tag{91}$$

The power on the other quadrants P_n^Q follows the same relation as given by Equation (90), but with sign changes for the coordinates $x_0 \to -x_0$ for $n \in \{2,3\}$ and $y_0 \to -y_0$ for $n \in \{3,4\}$. By combining the quadrant signals, the particle position is extracted as

$$(P_1^Q + P_4^Q) - (P_2^Q + P_3^Q) = P_x^{cal} k x_0 \tag{92}$$

$$(P_1^Q + P_2^Q) - (P_3^Q + P_4^Q) = P_y^{cal} k y_0 \tag{93}$$

$$\sum_{n=1}^{4} P_n^Q - P_{inc}^{\pi} NA_{cl}^2 = P_z^{cal} k z_0. \tag{94}$$

The calibration factor for each axis is given by

$$P_j^{cal} = \sqrt{\frac{24 P_{inc} P_{dip}}{\pi}} B_j^{fw} \tag{95}$$

with $j = (x, y, z)$.

BACKWARD DETECTION: A second common method, tweezer backward detection, collects light scattered backward through the trapping lens. This light can be separated from the incoming beam using polarization optics, as described in the experimental section. In this configuration, an external local oscillator provides the phase reference instead of the transmitted trapping light. The analysis is identical to forward detection, differing only in the lens parameters $\theta_{cl} \to \theta_{tl}$, $NA_{cl} \to NA_{tl}$, and $\mathbf{B}^{fw} \to \mathbf{B}^{bw}$, with

$$\mathbf{B}^{bw} = \int_0^{\theta_{tl}} d\theta \sin\theta \sqrt{\cos\theta} \begin{pmatrix} \sin\theta(1+2\cos\theta)/3 \\ \sin\theta(2+\cos\theta)/3 \\ \pi(\cos\theta + A)(1+\cos\theta)/4 \end{pmatrix}. \tag{96}$$

In the backward configuration, the detection for the x and y motion is identical to the forward configuration, but it differs for the z motion. To compare the performance to a Heisenberg-limited detection, we define a detection efficiency $\eta_j^{bw} = S_{imp}^{j} / S_{imp}^{j,bw}$. Here, S_{imp}^{j} is the measurement imprecision for the Heisenberg-limited measurement and $S_{imp}^{j,bw}$ is the measurement imprecision of the tweezer backward measurement. An efficiency of $\eta = 1$ indicates a Heisenberg-limit detection. For the particle's center of mass motion, the efficiencies are found to be

$$\eta_x^{bw} = \frac{30(B_x^{bw})^2}{\pi^2 NA_{tl}^2} \tag{97}$$

$$\eta_y^{bw} = \frac{15(B_y^{bw})^2}{\pi^2 NA_{tl}^2} \tag{98}$$

$$\eta_z^{bw} = \frac{15(B_z^{bw})^2}{(1+\frac{5}{2}A^2)\pi^2 NA_{tl}^2}. \tag{99}$$

For a setup with $NA_{tl} = 0.77$, the efficiencies are calculated to be $(\eta_x^{bw}, \eta_y^{bw}, \eta_z^{bw}) = (0.35, 0.39, 0.57)$. Note that for high enough numerical apertures, the detection efficiency along the z direction can be high enough to resolve the ground state of motion, which was used to actively cool it to its ground state [81, 122].

3.4 COHERENT SCATTERING

The coherent scattering interaction originates from tweezer photons scattering off a nanoparticle into a cavity mode. This creates a linear coupling between the particle's motion and the cavity electric field, without the need of a highly populated cavity mode. The interaction geometry, involving light scattering at a 90 ° angle, allows for a genuinely three-dimensional coupling. This technique was pioneered in the domain of atomic cooling [130]. In this section, I will first derive the Hamiltonian of the coupled particle-cavity system to show its three-dimensional nature. I then solve simplified Langevin equations for one motional degree of freedom and conclude by presenting a detection model for the cavity output that shows the asymmetry of the motional sidebands.

3.4.1 *Interaction Model*

In this section, I present a quantum description of the combined cavity-particle system, starting with the total Hamiltonian

$$\hat{H} = \hat{H}_f^p + \hat{H}_f^{em} + H_{int}. \tag{100}$$

The three parts include the description of the free particle motion $\hat{H}_f^p$, the Hamiltonian for the free electromagnetic field $\hat{H}_f^{em}$, and a term describing the interaction of the particle and the field $\hat{H}_{int}$. They are given by

$$\hat{H}_f^p = \frac{\hat{\mathbf{p}}^2}{2m} \tag{101}$$

$$\hat{H}_f^{em} = \frac{\varepsilon_0}{2}\int dV\left(\hat{\mathbf{E}}^2(\mathbf{r}) + c^2\hat{\mathbf{B}}^2(\mathbf{r})\right) \tag{102}$$

$$\hat{H}_{int} = -\frac{1}{2}\alpha\hat{\mathbf{E}}^2(\mathbf{x}, t). \tag{103}$$

The first term describes the free three-dimensional motion of the center of mass of a particle with mass m. The second term describes the free total electromagnetic field at a point $\mathbf{r}$ in space. The interaction is modeled by an induced dipole interacting with the total electric field at its position $\mathbf{x}$, which is only valid in the small particle limit. The total electric field $\hat{\mathbf{E}}(\mathbf{x})$ contains many modes in principle [55], but we focus on just two to keep the derivation manageable while still explaining the optomechanical coupling mechanism. These two modes are the field of the tweezer and the cavity

$$\hat{\mathbf{E}}(\mathbf{x}, t) = \hat{\mathbf{E}}_{tw}(\mathbf{x}, t) + \hat{\mathbf{E}}_{cav}(\mathbf{x}, t). \tag{104}$$

Both are modeled as TEM_{00} Gaussian beams. To match the experimental configuration, the cavity mode is aligned with the x-axis while the tweezer field propagates along the z-axis. Optimal coupling is achieved, when the two mode waists overlap. To allow for spatial alignment, we introduce two coordinate systems. The cavity's coordinate frame is denoted (x_c, y_c, z_c) and the tweezer's as (x,y,z), with origins located at their respective waists. Since the tweezer provides the trapping potential, the particle's motion is aligned with its coordinate frame. Three types of alignments are considered here: small displacements in x_c-direction, rotations around the z-axis, and small rotations around the y-axis. The rotations can be expressed via the matrix $\mathbf{x}_{cav} = R(\theta_1, \theta_2)\mathbf{x}_{tw}$

$$\begin{pmatrix} x_c \\ y_c \\ z_c \end{pmatrix} = \begin{pmatrix} \cos\theta_1 & \sin\theta_1 & 0 \\ -\sin\theta_1 & \cos\theta_1 & 0 \\ 0 & 0 & 1 \end{pmatrix} \begin{pmatrix} \cos\theta_2 & 0 & \sin\theta_2 \\ 0 & 1 & 0 \\ -\sin\theta_2 & 0 & \cos\theta_2 \end{pmatrix} \begin{pmatrix} x \\ y \\ z \end{pmatrix}. \tag{105}$$

Experimentally, the rotation around the z-axis is implemented via rotating the polarization of the tweezer beam, while the rotation around the y-axis is due to imperfect alignment of the tweezer objective. A sketch of the alignment of the modes can be seen in Figure 5. The electric fields of the two modes are given by

$$\hat{\mathbf{E}}_{cav}(\mathbf{x}, t) = \sqrt{\frac{\hbar\omega_{cav}}{2\varepsilon_0 V_{cav}}}\mathbf{e}_c \left(f(\mathbf{x}) e^{-i\omega_{cav}t}\hat{a} + f^*(\mathbf{x}) e^{i\omega_{cav}t}\hat{a}^\dagger \right) \tag{106}$$

$$\mathbf{E}_{tw}(\mathbf{x}, t) = \frac{1}{2}\left(\mathbf{E}_{tw}(\mathbf{x}) e^{-i\omega_{tw}t} + \mathbf{E}^*_{tw}(\mathbf{x}) e^{i\omega_{tw}t} \right). \tag{107}$$

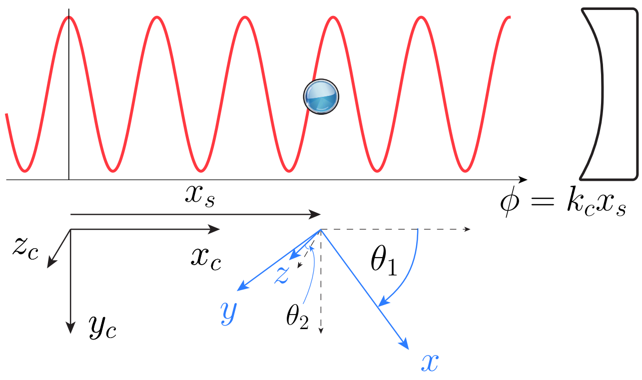

Figure 5: Relation between the cavity and tweezer coordinate systems. The tweezer frame (blue) is shifted by x_s and rotated by θ_1 about the z_c axis and by θ_2 about the y_c axis relative to the cavity frame (black). The cavity standing wave (red) is shown as a reference.

The tweezer field is assumed to be a strong classical field. The spatial mode functions are given by

$$f(\mathbf{x}_{cav}) = \frac{w_{0c}}{w_c(x_c)} \exp\left(-\frac{y_c^2 + z_c^2}{w_c^2(x_c)} - i\phi_{gc}(x_c)\right) \tag{108}$$

$$\times \cos\left(k_c x_c + \frac{k_c(y_c^2 + z_c^2)}{2R_c(x_c)}\right) \tag{109}$$

$$\mathbf{E}_{tw}(\mathbf{x}) = \frac{E_{0t} w_{0t}}{w_t(z)} \mathbf{e}_t \exp\left(-\frac{x^2}{w_{xt}^2(z)} - \frac{y^2}{w_{yt}^2(z)}\right) \tag{110}$$

$$\times \exp\left(\frac{ik_t(x^2 + y^2)}{2R_t(z)} + i\phi_{gt}(z) - ik_t z\right). \tag{111}$$

The cavity parameters are resonance frequency ω_{cav}, mode volume V_{cav}, waist w_{0c}, wavenumber k_c, and polarization $\mathbf{e}_c$. The tweezer parameters are frequency ω_{tw}, field strength E_{0t}, waist w_{0t}, wavenumber k_t, and polarization $\mathbf{e}_t$. The beam radii and radii of curvature are given by

$$w_c(x) = w_{0c}\sqrt{1 + \left(\frac{x}{x_0}\right)^2}, \tag{112}$$

$$R_c(x) = x\left(1 + \left(\frac{x_0}{x}\right)^2\right), \tag{113}$$

$$w_t(z) = w_{0t}\sqrt{1 + \left(\frac{z}{z_0}\right)^2}, \tag{114}$$

$$R_t(z) = z\left(1 + \left(\frac{z_0}{z}\right)^2\right). \tag{115}$$

The waist of the tweezer is modified in x and y direction by $w_{xt,yt}(z) = A_{x,y} w_t(z)$ to incorporate the non-degenerate trapping frequencies in the radial direction. The Rayleigh range of the cavity (tweezer) is given by x_0 (z_0)

$$x_0 = \frac{\pi w_{0c}^2}{\lambda_c} \tag{116}$$
$$z_0 = \frac{\pi w_{0t}^2}{\lambda_t} \tag{117}$$

where λ_c and λ_t are the wavelength of cavity and tweezer light. The Gouy phase shift is given by

$$\phi_{gc}(x_c) = \arctan\left(\frac{x}{x_0}\right) \tag{118}$$
$$\phi_{gt}(z) = \arctan\left(\frac{z}{z_0}\right) \tag{119}$$

A displacement along the cavity axis is modeled by the transformation $x_c \to x_c - x_s$, for a small shift $x_s \sim \lambda_c/4 \ll x_0$. We then insert the expression for the electric fields from Equation (106) and (107) into the Hamiltonian (100). The interaction originates from the interference of the tweezer and cavity fields in the interaction Hamiltonian

$$\left|\hat{\mathbf{E}}(\mathbf{x},t)\right|^2 = \left|\hat{\mathbf{E}}_{tw} + \hat{\mathbf{E}}_{cav}\right|^2 = \left|\hat{\mathbf{E}}_{tw}\right|^2 + \left|\hat{\mathbf{E}}_{cav}\right|^2 + \hat{\mathbf{E}}_{tw}^*\hat{\mathbf{E}}_{cav} + \hat{\mathbf{E}}_{tw}\hat{\mathbf{E}}_{cav}^*. \tag{120}$$

A more detailed calculation can be found in Appendix C. After approximation, the total Hamiltonian is

$$\begin{aligned}
\hat{H} \;=\; & \sum_{j=x,y,z} \hbar\Omega_j \left(b_j^\dagger b_j + \frac{1}{2}\right) \\
& + \hbar\omega_{cav}\left(a^\dagger a + \frac{1}{2}\right) - \frac{\alpha\hbar\omega_{cav}}{4\varepsilon_0 V_{cav}} \cos^2\phi \left(a^\dagger a + \frac{1}{2}\right) \\
& - \frac{\alpha\hbar\omega_{cav}}{4\varepsilon_0 V_{cav}} k_c \sin(2\phi) x_c \left(a^\dagger a + \frac{1}{2}\right) \qquad (121) \\
& - \frac{1}{2}\alpha\sqrt{\frac{\hbar\omega_{cav}}{2\varepsilon_0 V_{cav}}} E_{0t}\mathbf{e}_t \cdot \mathbf{e}_c \Big[\cos\phi\left(a^\dagger e^{i\Delta t} + a e^{-i\Delta t}\right) \\
& + i\cos\phi \frac{x_c}{x_0}\left(a^\dagger e^{i\Delta t} - a e^{-i\Delta t}\right) \\
& + i\cos\phi z \left(\frac{1}{z_0} - k_t\right)\left(a^\dagger e^{i\Delta t} - a e^{-i\Delta t}\right) \\
& + k_c x_c \sin\phi \left(a^\dagger e^{i\Delta t} + a e^{-i\Delta t}\right)\Big], \qquad (122)
\end{aligned}$$

where a modification due to the displacement manifests through the phase $\phi = k_c x_s$. The first line combines the free-particle terms with those from the particle-tweezer interaction. The next step is to move to a frame rotating with frequency Δ using the transformation $\hat{H} \to U^\dagger \hat{H} U - A$, where $U = e^{-i\Delta a^\dagger a t}$ and $A = \hbar\Delta a^\dagger a$. Note that this transformation only affects the cavity field. The transformed Hamiltonian is

$$\hat{H} = \sum_{j=x,y,z} \hbar\Omega_j \left(b_j^\dagger b_j + \frac{1}{2}\right) \tag{123}$$

$$+\hbar\left(\omega_t - \frac{\alpha\omega_{cav}}{4\varepsilon_0 V_{cav}}\cos^2\phi\right)\left(a^\dagger a + \frac{1}{2}\right) \tag{124}$$

$$-\frac{\alpha\hbar\omega_{cav}}{4\varepsilon_0 V_{cav}} k_c \sin(2\phi) x_c \left(a^\dagger a + \frac{1}{2}\right) \tag{125}$$

$$-\frac{1}{2}\alpha\sqrt{\frac{\hbar\omega_{cav}}{2\varepsilon_0 V_{cav}}} E_{0t}\mathbf{e}_c \cdot \mathbf{e}_t \cos\phi \left[\left(a^\dagger + a\right)\right. \tag{126}$$

$$\left.+i\frac{x_c}{x_0}\left(a^\dagger - a\right) + iz\left(\frac{1}{z_0} - k_t\right)\left(a^\dagger - a\right)\right] \tag{127}$$

$$-\frac{1}{2}\alpha\sqrt{\frac{\hbar\omega_{cav}}{2\varepsilon_0 V_{cav}}} E_{0t}\mathbf{e}_c \cdot \mathbf{e}_t k_c \sin\phi x_c \left(a^\dagger + a\right). \tag{128}$$

We can now interpret the obtained terms. The term in Line (123) describes free motion of the particle in the tweezer potential. Line (124) is the free cavity field with a correction to its energy due to the presence of the particle. Line (125) gives rise to dispersive optomechanical coupling, representing the particle's interaction with the field built up inside the cavity. While this term typically requires linearization, it will not be treated here. Its strength is proportional to $\sin(2\phi)$, making it maximal at the intensity slope of the cavity field. In contrast, Lines (126) and (127) are proportional to $\cos\phi$ and are thus maximal at the cavity intensity maximum. The term in Line (126) can be interpreted as an interaction between the tweezer and cavity fields, which is ignored from here on as it does not involve particle motion. The first term in Line (127) couples particle motion along the cavity axis to the cavity via the cavity Gouy phase. This interaction is very small due to the cavity's large Rayleigh length x_0. The second term in Line (127) is an interaction of the z motion with the cavity amplitude quadrature due to a phase acquired from particle displacement and the Gouy phase shift of the tweezer. The final term in Line (128) represents a genuinely linear optomechanical coupling between the particle's motion along the cavity axis and the cavity phase quadrature. This interaction requires no additional linearization. Its dependence on $\sin\phi$ indicates it is maximized at the cavity intensity minima. For simplicity, we write an effective Hamiltonian that includes only the dominant terms relevant to the particle motion

$$\begin{aligned} \hat{H} &= \sum_{j=x,y,z} \hbar\Omega_j \left(b_j^\dagger b_j + \frac{1}{2}\right) + \hbar\tilde{\omega}\left(a^\dagger a + \frac{1}{2}\right) \\ &\quad -i\hbar g_{z1}\frac{\hat{z}}{z_{zpf}}\left(a^\dagger - a\right) - \hbar g_{z2}\frac{\hat{z}}{z_{zpf}}\left(a^\dagger + a\right) \\ &\quad -\hbar g_y \frac{\hat{y}}{y_{zpf}}\left(a^\dagger + a\right) - \hbar g_x \frac{\hat{x}}{x_{zpf}}\left(a^\dagger + a\right). \end{aligned} \tag{129}$$

Using the coordinate transformation from (105), the particle position was expressed in the tweezer frame. To emphasize its quantum nature, hats were put on the position operators. The modified cavity frequency and coupling rates were introduced as

$$\tilde{\omega} = \omega_{tw} - \frac{\alpha\omega_{cav}}{4\varepsilon_0 V_{cav}}\cos^2\phi \tag{130}$$

$$g_{z1} = \frac{1}{2}\alpha\sqrt{\frac{\omega_{cav}}{2\hbar\varepsilon_0 V_{cav}}}E_{0t}\cos\phi\cos\theta_1\left(\frac{1}{z_0} - k_t\right)z_{zpf} \tag{131}$$

$$g_{z2} = \frac{1}{2}\alpha\sqrt{\frac{\omega_{cav}}{2\hbar\varepsilon_0 V_{cav}}}E_{0t}k_c\sin\phi\cos^2\theta_1\sin\theta_2 z_{zpf} \tag{132}$$

$$g_y = \frac{1}{2}\alpha\sqrt{\frac{\omega_{cav}}{2\hbar\varepsilon_0 V_{cav}}}E_{0t}k_c\sin\phi\cos\theta_1\sin\theta_1 y_{zpf} \tag{133}$$

$$g_x = \frac{1}{2}\alpha\sqrt{\frac{\omega_{cav}}{2\hbar\varepsilon_0 V_{cav}}}E_{0t}k_c\sin\phi\cos^2\theta_1\cos\theta_2 x_{zpf} \tag{134}$$

where we replaced $\mathbf{e}_c \cdot \mathbf{e}_t \sim \cos\theta_1$. Genuine three-dimensional optomechanical coupling is achieved by choosing a position ϕ and polarization angle θ_1 such that $\sin\phi \neq 0$ and $\cos\phi \neq 0$, and $\sin\theta_1 \neq 0$ and $\cos\theta_1 \neq 0$. Due to the small tilt of the z-axis with angle θ_2, a residual coupling to the z motion is maintained even when the coupling rate $g_{z1} = 0$, via the non-zero term $g_{z2} \neq 0$.

3.4.2 *Simplified Dynamics and Detection*

To illustrate the signal detected in the experiment, we will solve Langevin equations including dissipation and the dominant coupling between the cavity field a and the particle motion along the cavity b_x, which is denoted just as b henceforth. The Langevin equations are

$$\dot{a}(t) = -i\omega_c a(t) + i g_x\left(b^\dagger(t) + b(t)\right) - \frac{\kappa}{2}a(t) - \sqrt{\kappa}a_{in}(t) \tag{135}$$

$$\dot{b}(t) = -i\Omega b(t) + i g_x\left(a^\dagger(t) + a(t)\right) + \frac{\gamma}{2}\left(b^\dagger(t) - b(t)\right) + i\sqrt{\gamma}P_{in}(t) \tag{136}$$

Here, ω_c and Ω are the effective cavity and particle frequencies, while κ and γ are their damping rates. The input noise terms for the cavity

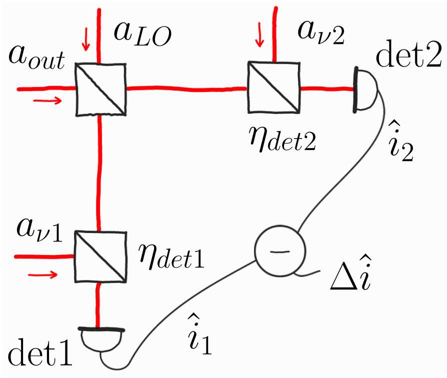

Figure 6: Model of balanced heterodyne detection of the cavity output. The output field $\hat{a}_{out}$ is mixed on a 50:50 beam splitter with a strong local oscillator $\hat{a}_{LO}$. Detection inefficiency is modeled by beam splitters before each detector, with vacuum at the auxiliary inputs. The photocurrents are then subtracted to obtain the difference signal $\Delta\hat{\imath}$.

and particle are a_{in} and P_{in}. The two equations and their complex conjugates can be written conveniently in Matrix from

$$\dot{\mathbf{a}}(t) = \mathcal{A}\mathbf{a}(t) + \mathbf{N}(t) \tag{137}$$

with

$$\mathbf{a}(t) = \begin{pmatrix} a(t) \\ a^\dagger(t) \\ b(t) \\ a^\dagger(t) \end{pmatrix}, \quad \mathbf{N}(t) = \begin{pmatrix} -\sqrt{\kappa}a_{in}(t) \\ -\sqrt{\kappa}a^\dagger_{in}(t) \\ i\sqrt{\gamma}P_{in}(t) \\ -i\sqrt{\gamma}P^\dagger_{in}(t) \end{pmatrix} \tag{138}$$

and

$$\mathcal{A} = \begin{pmatrix} -i\omega_c - \frac{\kappa}{2} & 0 & ig_x & ig_x \\ 0 & i\omega_c - \frac{\kappa}{2} & -ig_x & -ig_x \\ ig_x & ig_x & -i\Omega - \frac{\gamma}{2} & \frac{\gamma}{2} \\ -ig_x & -ig_x & \frac{\gamma}{2} & i\Omega - \frac{\gamma}{2} \end{pmatrix}. \tag{139}$$

This notation lets us write the solution in the Fourier space in a concise way

$$\mathbf{a}(\omega) = \left(-i\omega\mathbb{1} - \mathcal{A}\right)^{-1}\mathbf{N}(\omega) \tag{140}$$

$$= \overline{\chi}(\omega)\mathbf{N}(\omega), \tag{141}$$

where $\mathbb{1}$ is the unit matrix and $\overline{\chi}(\omega) = \left(-i\omega\mathbb{1} - \mathcal{A}\right)^{-1}$. To proceed, we require a model for detecting the cavity output field. To measure the sideband asymmetry discussed in Chapter 3.1, we employ balanced heterodyne detection. This technique allows for the measurement of both the positive and negative frequency components of the particle's motion, known as the anti-Stokes and Stokes sidebands. The measurement scheme is shown in Figure 6. A strong local oscillator $a_{LO}(t)$ is mixed with the cavity output $a_{out}(t)$ on a 50/50 beam splitter. Both beam splitter outputs are detected by photodiodes. The detection efficiency is modeled as a beam splitter with transmittance η placed in front of an ideal detector, which mixes in two uncorrelated vacuum fields, $a_{v1}(t)$ and $a_{v2}(t)$. The total fields in front of the detectors are

$$a_{det1}(t) = \eta\frac{1}{\sqrt{2}}(a_{out}(t)+a_{LO}(t))+\sqrt{1-\eta^2}a_{v1}(t) \quad (142)$$

$$a_{det2}(t) = \eta\frac{1}{\sqrt{2}}(a_{out}(t)-a_{LO}(t))-\sqrt{1-\eta^2}a_{v2}(t). \quad (143)$$

The input-output relation links the cavity field from Equation (141) to the output field via $a_{out}(t) = a_{in}(t) - \sqrt{\kappa}a(t)$. The detected photocurrents are $\hat{i}_{1,2} = a^\dagger_{det1,2}(t)a_{det1,2}(t)$ [53, 132], and the difference current is $\Delta\hat{i}(t) = \hat{i}_1(t) - \hat{i}_2(t)$. Assuming a highly populated coherent state $a_{LO}(t) = |\alpha_{LO}|e^{-i\omega_{LO}t} + a_{LO}$ as local oscillator and moving to a rotating frame, such that $a(t) \to a(t)e^{-i\omega_{sig}t}$, the difference current simplifies to

$$\Delta\hat{i}(t) \simeq |\alpha_{LO}|\Big(\eta^2 a_{in}(t)e^{-i\omega_{het}t} - \eta^2\sqrt{\kappa}a(t)e^{-i\omega_{het}t} + \eta\sqrt{1-\eta^2}a_v(t)e^{-i\omega_{het}t} + \text{H.c.}\Big). \quad (144)$$

The heterodyne frequency is given by $\omega_{het} = \omega_{sig} - \omega_{LO}$. The frequency of the local oscillator ω_{LO} is chosen in a way that ω_{het} is above all technical noise but within the detection bandwidth of the photodiodes. At this point, the difference current $\Delta\hat{i}$ is still a quantum operator. To obtain the classical spectrum that is actually measured, we symmetrize the quantum spectrum [53, 132], yielding

$$S_{\Delta i\Delta i}(\omega) = \frac{1}{2}\left(S_{\Delta\hat{i}\Delta\hat{i}}(\omega) + S_{\Delta\hat{i}\Delta\hat{i}}(-\omega)\right). \quad (145)$$

After doing some math (see Appendix B), the spectrum is given by

$$\begin{aligned} S_{\Delta i\Delta i}(\omega) = \frac{|\alpha_{LO}|^2}{2}\Big(&\overline{\overline{X}}{}^2_{2\alpha}(\omega+\omega_{het})C_{\alpha\beta}\overline{\overline{X}}{}^{1\,T}_{\beta 1}(-\omega-\omega_{het}) \\ &+\overline{\overline{X}}{}^1_{1\alpha}(\omega-\omega_{het})C_{\alpha\beta}\overline{\overline{X}}{}^{2\,T}_{\beta 2}(-\omega+\omega_{het}) \\ &\overline{\overline{X}}{}^2_{2\alpha}(-\omega+\omega_{het})C_{\alpha\beta}\overline{\overline{X}}{}^{1\,T}_{\beta 1}(\omega-\omega_{het}) \\ +\overline{\overline{X}}{}^1_{1\alpha}(-\omega-\omega_{het})&C_{\alpha\beta}\overline{\overline{X}}{}^{2\,T}_{\beta 2}(\omega+\omega_{het}) + 2\eta^2(1-\eta^2)\Big), \end{aligned} \quad (146)$$

where $\overline{\overline{X}}{}^1_{ij}(\omega)$ and $\overline{\overline{X}}{}^2_{ij}(\omega)$ are susceptibility matrices defined in Equation (226) and $C_{\alpha\beta}$ is the correlator matrix defined in Equation (231). The spectrum, plotted in Figure 7, shows motional peaks mixed with the cavity mode peak. To find the amplitudes of the mechanical peaks experimentally, we rescale the spectrum by the cavity mode profile, which can be measured independently. Figure 8 shows the mechan-

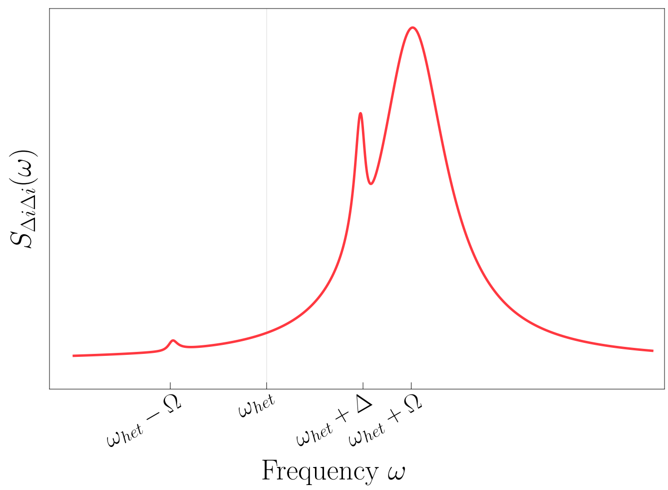

Figure 7: Detection of the cavity output light. Plotted is the classical spectrum of the detected current of a balanced heterodyne detection of the cavity output field $S_{\Delta i \Delta i}(\omega)$. The peaks corresponding to the mechanical motion of the particle are at $\omega_{het} - \Omega$ and $\omega_{het} + \Omega$. The peak corresponding to the cavity mode is at $\omega_{het} + \Delta$.

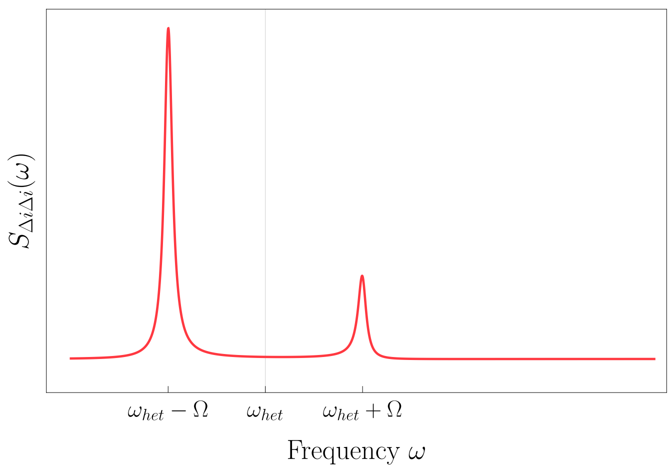

Figure 8: Detection of mechanical motion via balanced heterodyne detection with a flat cavity response. The two peaks correspond to the mechanical peaks at positive $+\Omega$ and negative $-\Omega$. The peaks are inverted since the photons involved in an energy lowering process have higher energy.

ical peaks with a flat cavity response. The peaks are inverted in frequency compared to Equation (42) because the measurement is performed on scattered photons, not on the phonons directly. Each time a lower-energy phonon is created, a higher-energy photon is created, leading to this spectral inversion.

4 GROUND STATE COOLING — THE EXPERIMENT

The previous section laid the groundwork for the experimental implementation of the main goal of this part of my thesis: cooling the center of mass motion of a levitated particle into its quantum ground state. In this section, I will give details on the platform and discuss the experimental results. The discussion is organized into three parts. First, Section 4.1 describes the tweezer trap, covering initial alignment, tweezer detection, and particle loading. Next, Section 4.2 details the optomechanical cavity, including its locking, and detection of the cavity output light, followed by a brief discussion of laser stability and vacuum requirements. Finally, Section 4.3 presents the measurement of the particle's motional ground state. A schematic overview of the experimental platform can be seen in Figure 9.

4.1 TWEEZER

In the following sections, I will describe how the optical trap of the nanoparticle is formed, how the particle is loaded into the trap and how we detect and verify that we trapped a particle. I will discuss how intensity noise of the trapping laser impacts the optical trapping and how we optimize the polarization of the trapping light. A sketch of the optical layout specific to the optical tweezer can be seen in Figure 10.

4.1.1 *Tweezer Alignment and Detection*

The optical trap is formed by tightly focusing a laser beam with a microscope objective. Even though the setup is designed to prevent the loss of alignment to the objective, it was necessary to align the tweezer from scratch. In this section, I will give an overview of the optical setup, explain how the tweezer is aligned, and how tweezer forward detection is implemented.
Light from an Nd:YAG laser (Innolight Mephisto, 2W) with a wavelength of $\lambda = 1064\mathrm{nm}$ and a frequency of $\omega_1 = 2\pi c/\lambda$ is split into three beams using half wave plates (HWP) and polarizing beam splitters (PBS). The first beam is used to lock the optomechanical cavity, which will be described in Section 4.2.1. The second beam is used as a local oscillator in the heterodyne detection, which will be described in Section 4.2.2. The third beam is coupled into an optical fiber and is used to cancel common classical noise in the tweezer z detection, which will be described at the end of this section. The transmitted

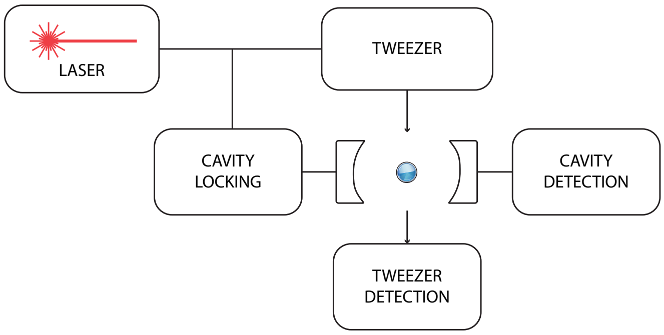

Figure 9: Schematic overview of the experiment. The description of experimental details is split into three parts. The tweezer trapping and detection of the tweezer light is discussed in Section 4.1. Locking of the optomechanical cavity is presented in Section 4.2.1. Detection of the cavity output light is discussed in Section 4.2.2. Detailed schematics of each sub-setup can be found in their respective sections.

beam is coupled into a fiber and amplified by a fiber amplifier (FA, Keopsys, maximal output power 5W). Since optical fibers tend to alter the polarization of the transmitted light, a half wave plate, a quarter wave plate, and a half wave plate are used to compensate for that change. The output fiber of the amplifier is butt coupled to a second fiber. The out coupler of the second fiber is never moved. If for any reason the amplifier needs to be maintained, moved, or completely replaced, the output fiber still remains aligned to the microscope objective. Nonetheless, alignment from scratch was necessary during my work on this project. The amplified laser is again out-coupled into a free-space mode. A telescope consisting of two lenses magnifies the beam to approximately 5 mm. The beam passes again through a series of three waveplates for polarization control before it enters the vacuum chamber where it is focused by a high-NA microscope objective (MO, NA=0.8, opening aperture $\sim$ 3 mm, working distance $=$ 3.4 mm) to form the optical trap. Note the large working distance of the objective, which is necessary to move the particle into the cavity mode without clipping [56].
Initial alignment of the objective is done by reducing the waist of the input beam as much as possible and aligning it to exit the objective without deflection. The objective is relatively insensitive to small alignment errors, allowing an initial optical trap to be formed. By expanding the beam to ~5 mm to slightly overfill the objective aperture and increasing the input power to ~1 W, a particle can be trapped. Details on the loading process can be found in Section 4.1.4. If no particle is trapped, the initial alignment is repeated. Once a particle is trapped, the alignment is optimized by maximizing the particle's axial (z) oscillation frequency. The axial trapping frequency depends on both the power in the focus and the Rayleigh range. For final alignment we use the power-independent ratio of axial to radial fre-

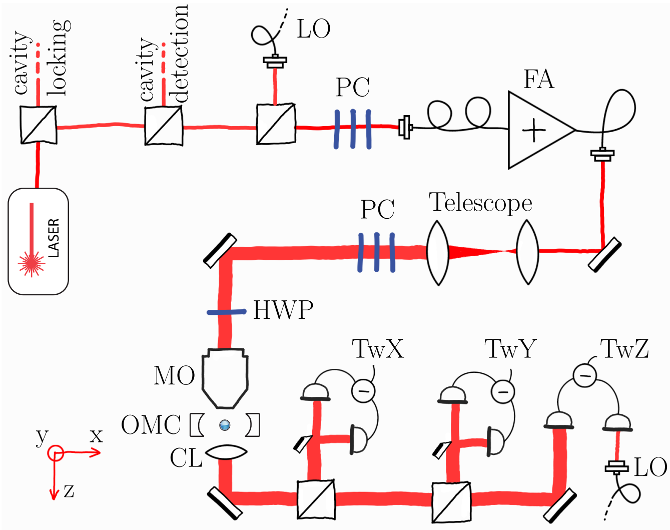

Figure 10: Schematic of the setup relevant for the optical tweezer and tweezer detection. The light of the Mephisto is amplified by a fiber amplifier (FA) and expanded to overfill the aperture of a microscope objective (MO). In the focus a nanoparticle is trapped. The transmitted light is recollimated and detected by a 3D tweezer detection scheme.

quencies Ω_x/Ω_z. This ratio is maximized when the Rayleigh range is minimized, which indicates an optimal alignment. We tune the system to achieve a ratio of $\Omega_x/\Omega_z \sim 4$, which gives us oscillation frequencies of $(\Omega_x, \Omega_y, \Omega_z)/2\pi \sim (305, 275, 80)$ kHz. We can estimate the tweezer waists to be $W_x = 0.67$ µm and $W_y = 0.77$ µm.
To position the trapped particle with respect to the cavity mode, the microscope objective is mounted on a 3D nano positioner (Mechonics MX35, step size ~ 8 nm). The range of transverse motion is small relative to the diameter of the input beam, which ensures that the trap alignment and trapping potential are not disturbed as the particle is repositioned. After the focus, the fast expanding beam, is recollimated by a lens (f = 15.29 mm, NA = 0.16) placed in the vacuum chamber. The collimation lens has a high working distance to limit backscattering of the trapping light into the cavity mode. It is mounted on its own 3D nanopositioner (Mechonics MX25) for alignment with respect to the optical trap. The collimated tweezer light is detected by a tweezer forward detection scheme. Instead of a quadrant photodetector, for the x/y motion, we split the light using a D-shaped mirror and detect each half-beam by a balanced photodetector (Thorlabs, PDB425C-AC). For the z motion, the full beam is detected by one diode of a balanced photodetector. To cancel classical common noise, a reference beam (tweezer LO) is detected on the other diode. A plot of typical spectra from the tweezer forward detection can be seen in Figure 11.

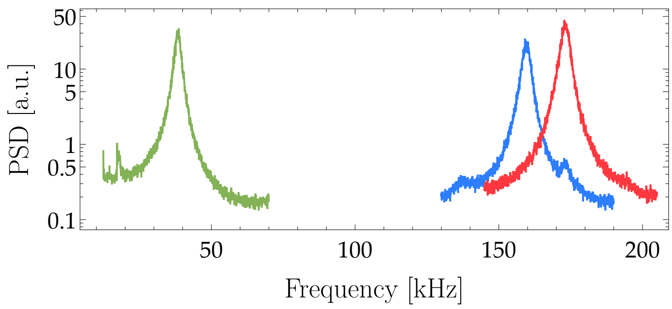

Figure 11: Power spectral densities of the forward tweezer detection. Z-direction plotted in green, y-direction plotted in blue and x-direction plotted in red. A small amount of cross-coupling due to alignment errors can be seen in the blue spectrum.

4.1.2 *Polarization of the Trapping Light*

The theory in Section 3.4 assumes that the tweezer light is linearly polarized at the trapping position and can be easily rotated to any other linear polarization. The observant reader of Section 3.3 may have noticed that tightly focusing a Gaussian beam changes its polarization. A linearly polarized beam at the input of the objective will not be linearly polarized in the focus. For ground state cooling, however, we require vertical polarization at the trap to optimize the mode overlap of the scattered light with the cavity mode and to align the particle's motion with the cavity axis. We cannot, however, directly measure the polarization at the trapping plane for technical reasons. Since the particle is trapped some distance away from the focus, we find the polarization of the recollimated beam to be a good approximation of the polarization at the trapping position. We can measure the polarization outside of the vacuum chamber easily with a polarimeter. As seen in Figure 10, we use a HWP-QWP-HWP combination to initially set the polarization to vertical. Then, right in front of the vacuum chamber, we use a HWP to rotate the polarization from vertical (maximal scattering into the cavity) to horizontal (minimal scattering into the cavity) during measurement runs. This simple technique does not allow for rotation through only linear polarizations. The plane of rotation is slightly angled. A polarization measurement can be seen in Figure 12. We optimize for vertical polarization, leaving a slightly elliptical polarization elsewhere. The scattering is still strongly suppressed in the horizontal setting and we remain with a three-dimensional coupling in between vertical and horizontal polarizations.

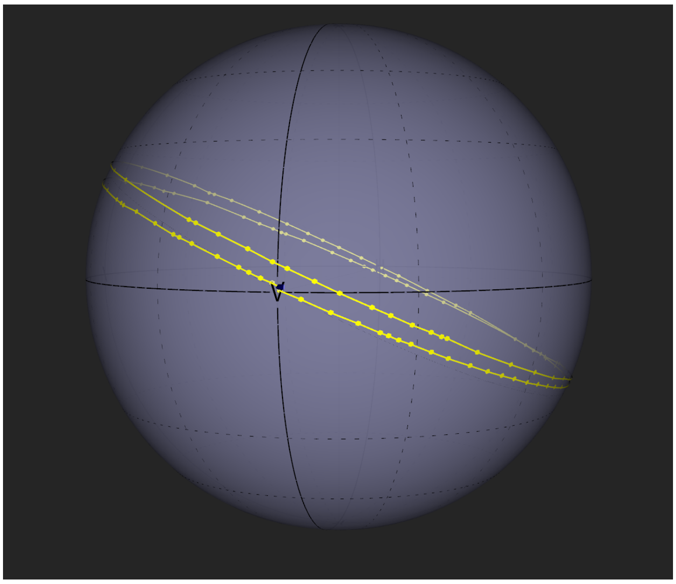

Figure 12: Measurement of the polarization of the recollimated tweezer beam. Measurements are represented by yellow points on the Bloch sphere while rotating the HWP in the input of the tweezer. The plane of rotation of the polarization is angled with respect to the plane of linear polarizations. Shown are two full rotations of the polarization which do not perfectly loop into each other due to an imperfect wave plate.

4.1.3 *Laser Intensity Noise*

As discussed in Section 3.3, additional heating of the particle motion may be introduced via parametric driving by laser intensity noise. It is introduced via a negative damping rate [115]

$$\gamma_{\mathrm{int}} = -\pi^2 \Omega^2 S_{\mathrm{RIN}}(2\Omega), \tag{147}$$

where $S_{\mathrm{RIN}}(2\Omega)$ is the relative intensity noise at twice the mechanical frequency Ω. While Mephisto lasers typically have low intensity noise of ~ -135 dB/Hz, the fiber amplifier may increase the noise levels significantly. Therefore, we measure the intensity noise of the Mephisto alone and the Mephisto amplified by the fiber amplifier. As can be seen in Figure 13, the noise levels are significantly increased for frequencies smaller than 100 kHz. To minimize the added heating, we intentionally increase the trapping power until the second harmonics of the particle motion are above the frequency band with increased intensity noise. The calculated damping rates for the particle frequencies used here $(\Omega_x, \Omega_y, \Omega_z)/2\pi \sim (305, 275, 80)$ kHz are $(\gamma^x_{\mathrm{int}}, \gamma^y_{\mathrm{int}}, \gamma^z_{\mathrm{int}})/2\pi \sim -(6, 5, 0.5)$ mHz. For the x and y motion, the additional damping is negligible compared with the cooling rates of at least 1 kHz. The z motion, however, is not strongly cooled and the additional heating can become significant, but does not lead to particle loss.

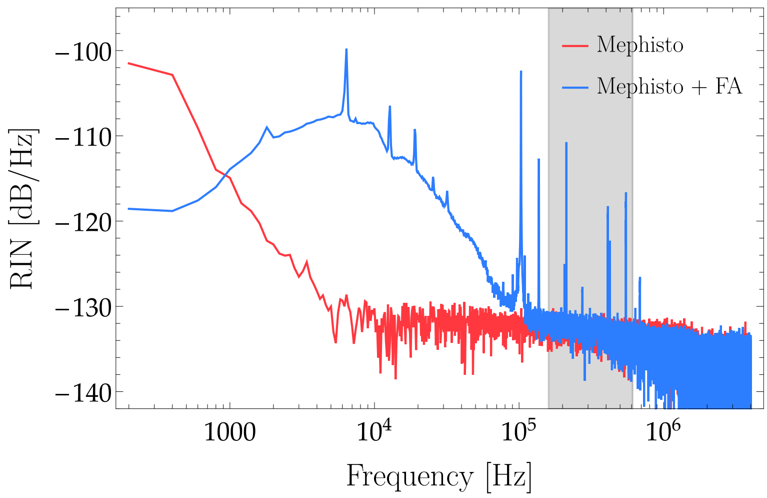

Figure 13: Measured intensity noise of the Mephisto laser alone (red) and the Mephisto amplified by the fiber amplifier (blue). The amplification adds a significant amount of noise at frequencies below 100 kHz. We increase the particle frequencies such that twice the mechanical frequency is above the added noise (gray region) to avoid parametric heating.

4.1.4 *Particle Loading*

The particles used in this experiment are silica spheres bought from microParticles GmbH and are shipped in a aqueous solution. Here, particles with a diameter of $d = 143 \pm 4$ nm and a density of $\rho = 1850$ kg/m^3 (as specified by the producer) are used. An SEM picture can be seen in Figure 14. A key aspect of levitated nanoparticles – that they lack a rigid connection to a support structure – is both a significant advantage and a practical challenge. While it provides excellent isolation, it also means a particle can easily escape the optical trap, resulting in its permanent loss and necessitating the loading of a new one. Many technological advancements regarding loading techniques have been made since this experiment was designed. Loading via LIAD [16, 43, 71], piezo-based [8, 65] or hollow-core-fiber-based [74] loading are some examples. Here, we use the easy-to-implement but crude method of loading via nebulizer, mostly for historical reasons.

To load nanoparticles, we repurpose a medical nebulizer (OMRON MicroAir U22) to vaporize a solution of nanoparticles in isopropanol, using a ratio of 5 µl of particle solution to 5 ml of isopropanol. The resulting mist consists of isopropanol droplets approximately 2 µm in size. The solution ratio is chosen so that each droplet contains less than one particle on average. The nebulizer is housed in a vacuum dome at atmospheric pressure, which is connected to the main science chamber via a tube and a gate valve. To introduce the particles, we first pump the science chamber to a base pressure of approximately 10^{-2} mbar and then briefly open the gate valve. The pressure differential transports the aerosol into the chamber where the optical

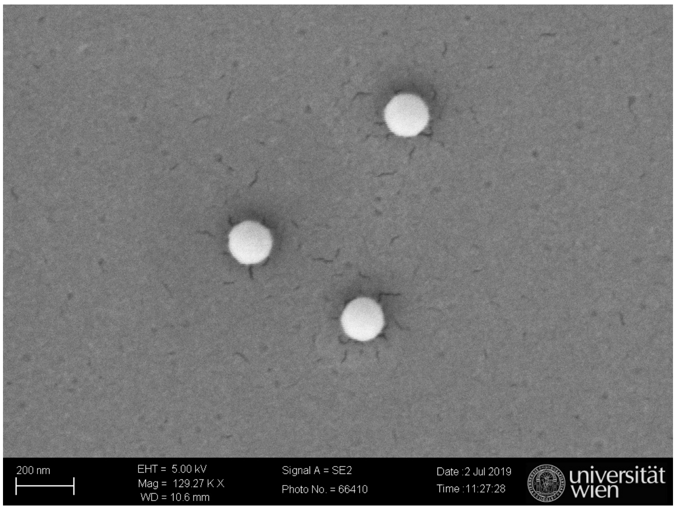

Figure 14: Scanning electron microscope image of silica nano particles with a diameter of 143 ± 4 nm.

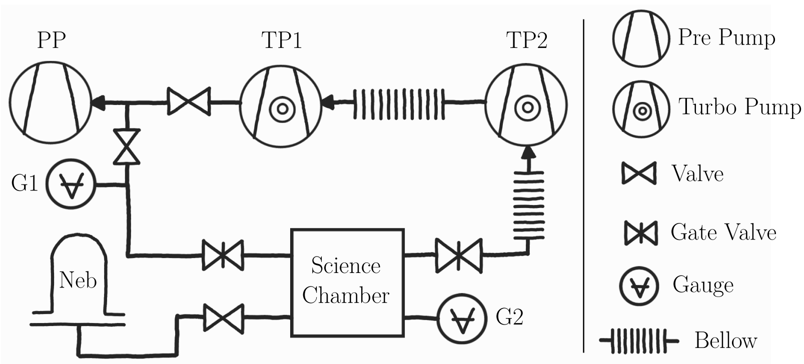

Figure 15: Schematic of the vacuum system. Vacuum pumping is done either via a scroll pump (PP) directly or via two chained turbo pumps (TP1 and TP2). Two gauges measure the pressure at medium vacuum (G1) or high and ultra high vacuum (G2). The particle loading chamber (Neb) is connected via a separate line.

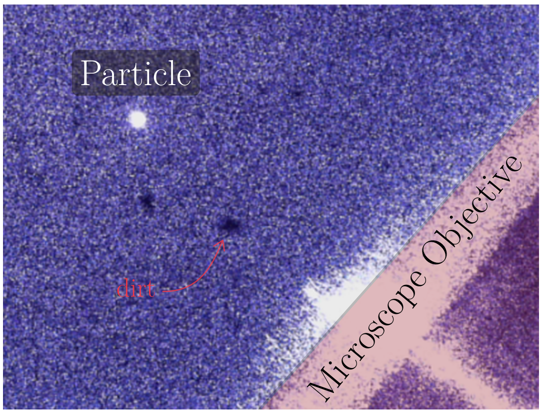

Figure 16: Camera image of a trapped particle in the optical tweezer. Scattering off the objective can be seen in the bottom right corner. The black spots are dirt on the camera. The optomechanical cavity is removed in this image.

tweezer is located. This cycle is repeated until the chamber pressure reaches approximately 200 mbar, a level chosen to heavily overdamp the particle motion. A schematic of the vacuum system is shown in Figure 15.

This loading process is inherently dirty, coating the vacuum chamber and all equipment inside with isopropanol, water, and particles, which results in two major problems. First, outgassing limits the final vacuum pressure and pumping speed. Although bake-outs would typically mitigate this, the chamber gets re-contaminated with each loading cycle, necessitating another bake-out. To prevent misalignment or damage, only long, low-temperature bake-outs are possible, making the entire loading and baking cycle unfeasible. Instead, we accommodate longer pump durations during measurements, which is discussed further in Section 4.2.8. Second, the finesse of the optomechanical cavity would degrade severely if even a single particle were deposited on a mirror within the cavity mode. To prevent this, the setup was designed in a modular way [56], allowing the cavity to be removed during trapping and reinserted only after all airborne particles are evacuated (see Chapter 4.2). Deposits on other optical elements pose a lesser problem. We expect a slight reduction in transmission but have not observed any impact on the setup's overall performance.

When the science chamber is filled with droplets, eventually one will fall into the optical trap by chance. Gas damping ensures that the particle does not pass the trapping region. On a camera monitoring the trap, we see the light scattered by the trapped particle. An example picture can be seen in Figure 16. At this point, we do not know if a single particle, a cluster, a droplet, or a particle with a liquid shell was trapped. To ensure that it is a single particle, we evacuate the science chamber below ~ 0.1 mbar using the pre-pump, removing all remaining airborne droplets in the process. Below this pressure, any trapped

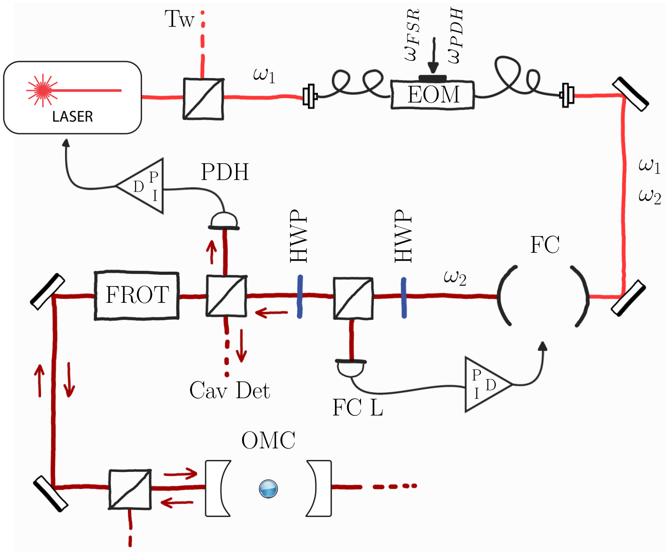

Figure 17: Schematic of the setup used to lock the optomechanical cavity. An EOM generates the laser sidebands required for locking. A filtering cavity removes unwanted frequency components. The optomechanical cavity is locked to laser frequency ω_2 via a PDH scheme.

droplets and liquid shells around a particle evaporate quickly. Finally, we look into the tweezer detection and inspect the motional spectrum of the trapped object. A spherical particle has a spectrum with three Lorentzian peaks corresponding to the x y and z motion. Signatures of rotation would appear as a broad spectral feature that is changing frequency depending on the amount of circular polarization of the trapping light. If no signatures of rotation are present, we assume a spherical particle of the expected size is trapped. For initial characterization of the spectrum, we measured the mass of an individually trapped particle as detailed in [33] and use SEM pictures to confirm the diameter of the particle batch.

4.2 CAVITY

This section provides a detailed overview of the part of the setup relevant to the optomechanical cavity, which is presented in Figure 17. The discussion will cover the cavity locking procedures and the interplay of the various laser frequencies. I will explain the various detection techniques used for the cavity output fields, including homodyne detection for the locking mode, power measurement of the coherent scattering mode and heterodyne detection of the coherent scattering mode. Finally, I will present the modular design of the cavity assembly and discuss various characterization measurements of the cavity itself.

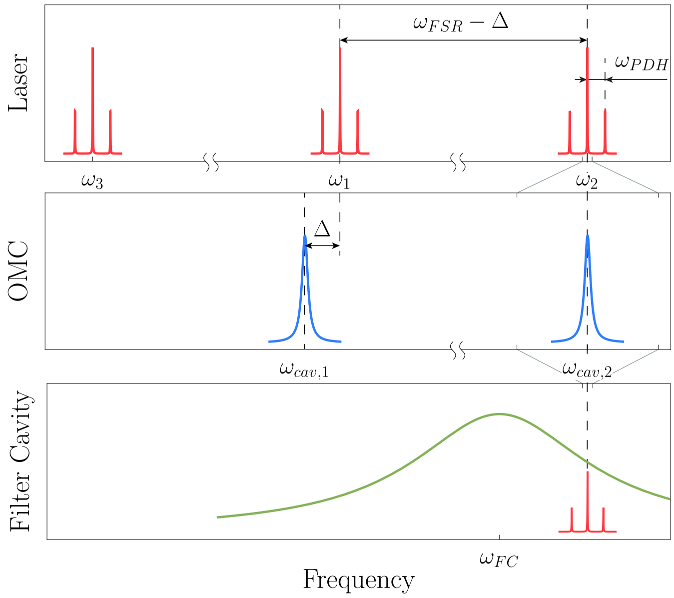

Figure 18: Diagram of all frequencies used in the locking process. The EOM creates frequency components in the laser light (red). The response functions of the optomechanical cavity (OMC) and the filtering cavity are shown in blue and green. The axis of the middle plot is zoomed in. The tone at frequency ω_1 drives the tweezer and is detuned by Δ to the cavity resonance at frequency $\omega_{cav,1}$. The tone at ω_2 is locked to the cavity resonance at $\omega_{cav,2}$ and to the side of the filtering cavity resonance at ω_{FC}.

4.2.1 *Locking*

The optomechanical cavity was built as a monolithic aluminum piece to eliminate noise from piezo actuators. This design makes it vulnerable to acoustic vibrations and thermal drifts. Consequently, its resonance frequency fluctuates and drifts significantly relative to the driving laser's mode structure. We employ a two-stage locking scheme to stabilize the laser frequency to the resonance frequency of the cavity. A Pound–Drever–Hall (PDH) [40] lock corrects for small but fast fluctuation with a ~1 kHz bandwidth, while a separate, slower lock compensates for large, temperature-induced drifts of the cavity holder. In the following, I will trace the beam path dedicated to this locking system and explain how the necessary laser frequencies are derived.

The main laser light at frequency ω_1 is coupled into a fiber-based electro-optic modulator (EOM) driven by two RF tones. The first tone is set near the cavity's free spectral range $\omega_{FSR} + \Delta$, while the second is set to $\omega_{PDH}/2\pi = 6$ MHz. This produces a spectrum of frequency components spaced by approximately one FSR, where each component has sidebands at $\pm\omega_{PDH}$, as shown in Figure 18. The light is subsequently coupled into a filtering cavity (FC) of simple construction. It consists of two mirrors spaced by a ring piezo to adjust its length. The filtering cavity is designed to transmit the three tones

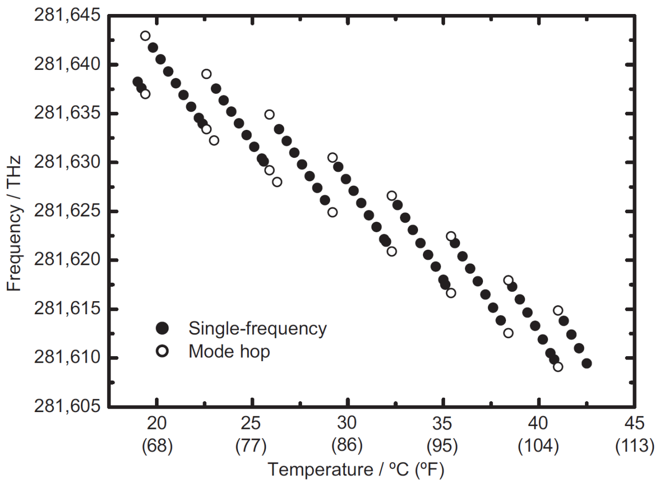

Figure 19: Mode structure of the Mephisto laser[1]. continuous cavity locking is possible in between two mode hops. n

around $\omega_2 = \omega_1 + \omega_{FR} + \Delta$, while rejecting all other frequencies. Its fundamental resonance has a linewidth of $\kappa_{FC}/2\pi = 80$ MHz, which is small compared to $\omega_{FSR}/2\pi \sim 14.0129$ GHz but large compared to ω_{PDH}. We lock the filtering cavity's resonance to the upper triplet of tones using a side-of-fringe scheme that maintains constant transmitted power. This is achieved by sampling a small portion of the FC output by a photodiode (FCL) via a half-wave plate and polarizing beam splitter to generate an error signal that drives a Toptica PID 110 to adjust the filtering cavity length. The filtered light is then coupled into the optomechanical cavity (OMC). The light reflected by the OMC is split off and detected to create the error signals for the fast PDH and slow thermal locks. The fast PDH lock acts on a piezo element inside the Mephisto laser via a Toptica PID 110. We limit its bandwidth to ~1 kHz to avoid a reaction to signals from particle motion. The tuning range of the PDH lock is limited by the piezo actuator to ~ 50 MHz[1]. However, the drifts due to thermal expansion of the cavity are much larger. To overcome this, we implement a secondary, slow thermal lock that adjusts the laser crystal temperature. This thermal lock uses a feedback signal from a Zurich Instruments HF2LI module, which processes an error signal derived from the PDH lock. While the Mephisto laser system has a total frequency tuning range of ~ 30 GHz, the laser's mode structure (Figure 19) prevents continuous tuning, which limits experimental run times, as discussed in Section 4.2.8. The combined locking scheme has two key functions. First, it stabilizes the laser frequency ω_2 to the cavity resonance frequency $\omega_{cav,2}$. To avoid significant dispersive coupling between the particle's motion and the locking mode, we limit the power of the locking mode to $> 10\mu W$. Second, by design, it also locks the tweezer

1 See Operator's Manual Mephisto Lasers

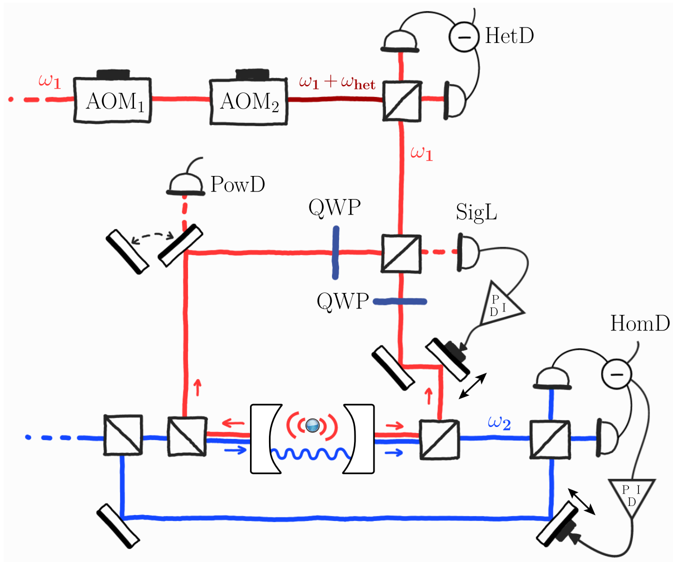

Figure 20: Sketch of cavity detection of the two longitudinal cavity modes. The locking mode (blue) is read out by balanced homodyne detection (HomD). The coherently scattered mode (red) is measured either with a DC photodiode (PowD) or by balanced heterodyne detection (HetD).

laser frequency ω_1 close to its adjacent cavity resonance $\omega_{cav,1}$. We can control the detuning $\Delta = \omega_1 - \omega_{cav,1}$ indirectly by changing the EOM drive frequency. This action does not immediately shift ω_1 but instead moves ω_2 away from its lock point. The PDH lock then instantly corrects this by pulling ω_2 back to $\omega_{cav,2}$, which in turn shifts ω_1 and alters the detuning Δ.

4.2.2 *Cavity Detection*

We are using two longitudinal modes of the optomechanical cavity in this experiment. The first is a locking mode, which is driven on resonance through an input mirror. The second is the coherent scattering mode, which is not externally driven and remains empty until a particle is coupled to the cavity. It is then populated from within by the particle's coherently scattered light, which is typically red-detuned from the cavity resonance. The generation and arrangement of those modes is explained in Section 4.2.1. The two modes are in orthogonal polarization states and their outputs are measured separately. While a balanced homodyne detection is performed on the locking mode, the output of the coherent scattering mode is measured either by a DC photodiode to monitor its power or by a balanced heterodyne detection. A schematic of the complete detection setup is shown in Figure 20.

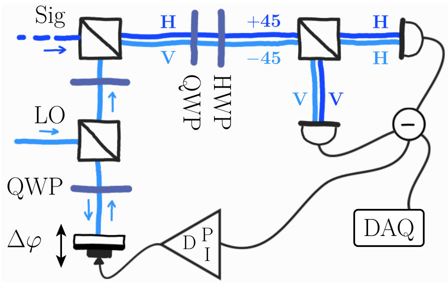

Figure 21: Schematic of homodyne detection for the locking mode. The cavity output (Sig, dark blue) is interfered with a local oscillator (LO, light blue), with beam polarizations indicated by their respective colors.

LOCKING MODE HOMODYNE Although particle motion is imprinted on the phase quadrature of the locking mode via dispersive coupling, this interaction is neglected in the theory detailed in Section 3.4 because of its low coupling rate. At high occupation, we can still detect the particle motion via the locking mode. A detailed description of the theory is omitted here as it is only an alignment tool. More information can be found elsewhere [33]. A detailed sketch of the homodyne detection scheme can be seen in Figure 21.

We split off the horizontally polarized locking mode with a PBS and overlap it with a local oscillator on a second PBS. Spatial mode matching is achieved by steering the local oscillator, with the wave fronts matched sufficiently well by the setup's design. At this stage, the combined beams are spatially overlapped but have orthogonal polarizations. We then use a half-wave plate and a quarter-wave plate to rotate these two components into +45° and -45° polarization states. A final PBS then splits the beam 50/50, producing two outputs that are now matched in both space and polarization. These two outputs are sent to a balanced photodetector (Thorlabs PDB425C-AC) for measurement. For stable detection of the phase quadrature, we lock the local oscillator's phase to the signal beam's phase. Phase adjustment is done with a piezo-actuated mirror in the local oscillator's beam path. We generate an error signal by subtracting the two monitor outputs of the detector using a custom-built SUM-DIFF box. This error signal is fed to a Toptica PID110, which locks it to zero, resulting in a phase quadrature detection. The final signal is either monitored as a live spectrum or recorded as a time trace using an oscilloscope (Pico Technology, PicoScope 5442B). Because this detection method measures particle motion along the cavity axis regardless of the tweezer's position, orientation, or polarization, it is an ideal tool for alignment. We first set the tweezer trap's polarization (as detailed in Section 4.1.2). Then, using the locking mode homodyne signal, we confirm that this procedure successfully aligns the tweezer trap axis parallel to the cavity axis, as demonstrated by the measurement in Figure 22. We rotate the trap polarization with the HWP in front of the vacuum chamber

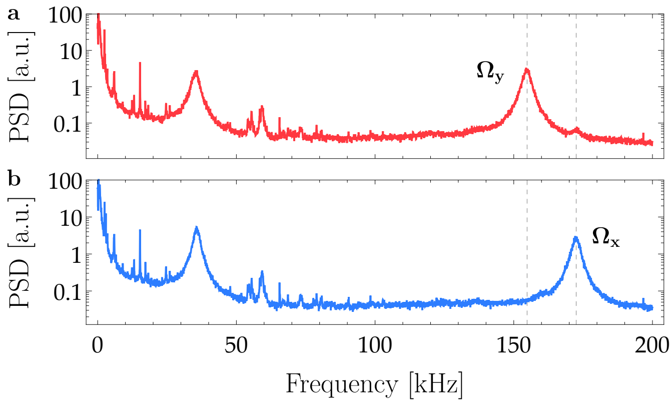

Figure 22: Homodyne measurement of particle motion using the locking mode with the tweezer horizontally polarized (**a**) and vertically polarized (**b**). The x-motion is slightly coupled to the cavity mode in the horizontal configuration.

from horizontal to vertical while monitoring the locking mode homodyne signal. In an ideal scenario, this rotation would only change the peak heights in the homodyne spectrum, while the motional frequencies would remain constant. We observe two deviations from this ideal case. First, we see a small change in the Ω_x and Ω_y frequencies, indicating the tweezer potential is being slightly distorted. This can be explained by the fact that the polarization in the trapping plane does not remain purely linear as it is rotated. Second, we observe coupling of the z motion to the locking mode, which indicates that the cavity axis is not perfectly perpendicular to the tweezer propagation [33]. Although both effects are small, the latter is beneficial as it provides a small amount of cooling to the z motion, which stabilizes the particle.

DETECTION OF THE COHERENT SCATTERING MODE Due to the symmetrical configuration of the optomechanical cavity (see 4.2.3), the coherent scattering (CS) mode leaks through both end mirrors at equal rates. We split this light from both cavity outputs using a PBS to perform one of two measurements.

We measure the DC power of one output with a photodiode (Thorlabs SM05PD4A) amplified by a current amplifier (Femto DHPCA). The measured power is proportional to the intra-cavity power. The built-up power depends on the particle's position within the standing wave as $\cos^2(x_0 k)$ (see Equation 126), reaching a maximum at an intensity antinode ($x_0 = 0$) and a minimum at an intensity node ($x_0 = \pi/4$), where $\phi = x_0 k$ is used to show the position dependency explicitly. We use this method for initial particle positioning and for continuous monitoring during operation. A scan of the particle position along the cavity standing wave can be seen in Figure 23.

For balanced heterodyne detection of the CS mode, we maximize the

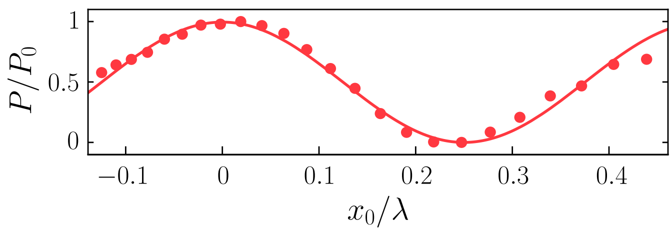

Figure 23: Power leaking from the coherent scattering mode as the particle is moved along the cavity standing wave.

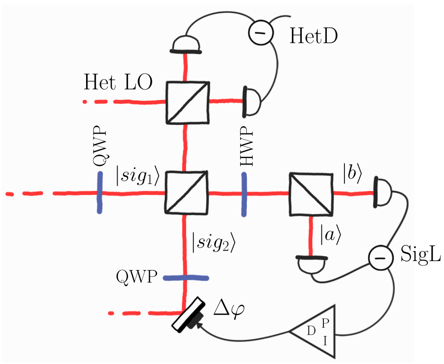

Figure 24: Heterodyne detection and coherent polarization beam combination. The two output beams of the coherent-scattering mode are combined on a PBS. Small amounts of L/R-polarized light are added to the sig1/sig2 beams. One PBS output is measured with a balanced detector. A movable mirror is actuated to lock the relative phase of the two signal beams.

signal-to-noise ratio by coherently combining the output light from both cavity mirrors. This is achieved by engaging a flip mirror to combine the two output beams on a PBS. A coherent beam combination [126] is essential, as it allows the combined signal to be beat with a local oscillator. A schematic of the coherent polarization beam combination scheme is shown in Figure 24. For efficient beam combination, we use a minimal amount of light for a phase-locking procedure. First, we add a small circularly polarized component to each signal beam with quarter-wave plates, creating the states

$$|\mathrm{sig1}\rangle = |V\rangle + \varepsilon|L\rangle \tag{148}$$
$$|\mathrm{sig2}\rangle = (|H\rangle + \varepsilon|R\rangle)e^{i\Delta\varphi}, \tag{149}$$

where a randomly drifting phase difference $\Delta\varphi$ is added in $|\mathrm{sig2}\rangle$ and ε is a small coefficient. We then perform a balanced DC measurement of one PBS output using a HWP and a PBS to generate an error signal that is proportional to the relative phase drift $\Delta\varphi$. The beams right in front of the detectors are

$$|a\rangle = |H\rangle + i|V\rangle e^{i\Delta\varphi} \tag{150}$$
$$|b\rangle = |V\rangle - i|V\rangle e^{i\Delta\varphi}, \tag{151}$$

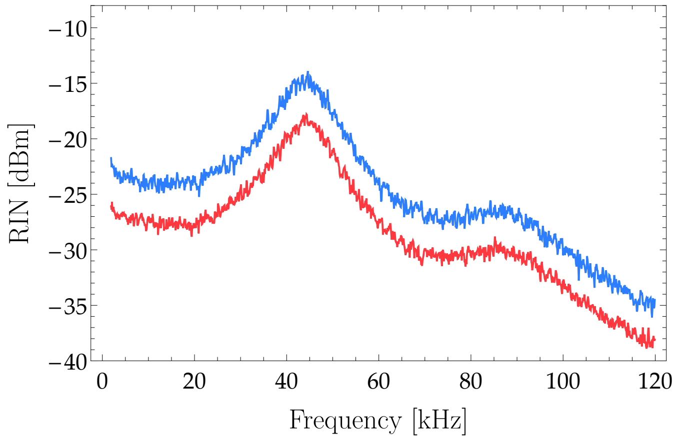

Figure 25: Heterodyne spectrum of the coherent-scattering mode with both cavity output beams combined (blue) and a single output beam (red). Data taken at the intensity maximum with a 500 kHz detuning.

which leaves the difference of the measured intensities as

$$\langle b|b\rangle - \langle a|a\rangle = 4\sin(\Delta\varphi). \tag{152}$$

This error signal is fed back to a movable mirror, which actuates the phase of signal 2 to lock the phase difference $\Delta\varphi = 0$. When locked, the two beams combine coherently into the state

$$|\mathrm{combined}\rangle = |V\rangle + |H\rangle e^{i\Delta\varphi} = |+\rangle, \tag{153}$$

where the small circularly polarized contribution was omitted. Experimentally, we reduce the locking power to ~ 500 nW, leaving 2.1 μW and 2.5 μW for the signal beams. Locking these signals is challenging because they are inherently unstable. Their power drifts with the particle's position in the cavity, and they have large fluctuations, since they are modulated by the particle motion. To maintain a stable lock, we must use strong filtering and carefully balance the locking detector to keep the setpoint at zero. Any imbalance or setpoint offset will cause the locking phase $\Delta\varphi$ to drift, reducing the benefit of the beam combining stage. A comparison of a heterodyne spectrum taken with and without beam combination can be seen in Figure 25.
We perform balanced heterodyne detection using a local oscillator (LO) detuned by 10.2 MHz, chosen to be within the 75 MHz detector bandwidth but above technical noise of the detection apparatus. We create this detuning by passing the LO through two consecutive AOMs, shifting its frequency by +205.1 MHz and -194.9 MHz. The LO and signal are combined in a variable fiber beam splitter (F-CPL-1060-N-FA, Newport). The control over the splitting ratio is superior to other methods we tested. Proper balancing is crucial for rejecting common-mode noise, such as LO intensity noise. We operate at low LO powers $P_{LO} \sim 400$ μW to ensure the detection is shot-noise limited around the heterodyne frequency. To demonstrate this, we measure

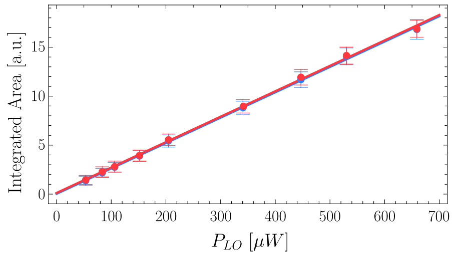

Figure 26: Integrated area of heterodyne spectra versus local-oscillator power with the signal beam blocked. Integrated bands: blue trace $(-350, -250)$ kHz and red trace $(250, 350)$ kHz. The linear scaling is a signature of a shot-noise limited detection.

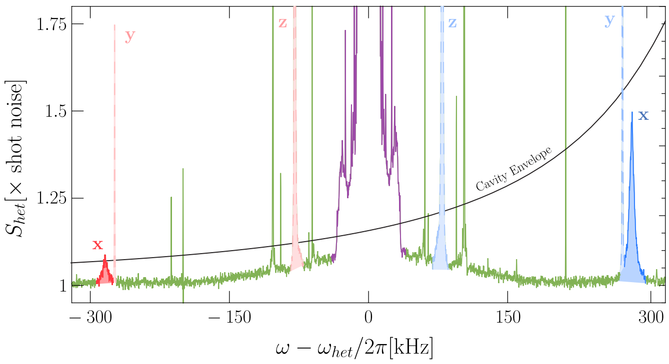

Figure 27: Heterodyne spectrum of the particle position with strongly cooled x motion. All three center-of-mass modes are visible and labeled. The x-mode linewidth is significantly broader due to strong cooling. Stokes (red) and anti-Stokes (blue) sidebands are indicated. The black curve shows the cavity transfer function scaled to the x-mode Stokes sideband power. The central purple feature corresponds to the tweezer carrier frequency. Remaining features are attributed to tweezer intensity noise or electronic noise.

the noise spectrum at various LO powers with the signal blocked. The integrated noise in the $(-350, -250)$ kHz and $(250, 350)$ kHz bands shows a linear scaling with LO power, as seen in Figure 26, which is the expected scaling of shot noise. Figure 27 shows an example heterodyne spectrum with strongly cooled x-motion. All three motional degrees of freedom are detected, as described in Section 7, with their corresponding peaks labeled in the plot. The x-peak is significantly smaller in amplitude and broader due to heavy cooling. The cavity envelope, shown as a black line, indicates the expected height difference between the Stokes and anti-Stokes sidebands, which are highlighted in red and blue. The dominant central peak corresponds to the carrier frequency of the tweezer and is present due to imperfect suppression of the elastic scattering process. Other peaks are attributed to technical noise, such as laser amplitude noise or electronic noise.

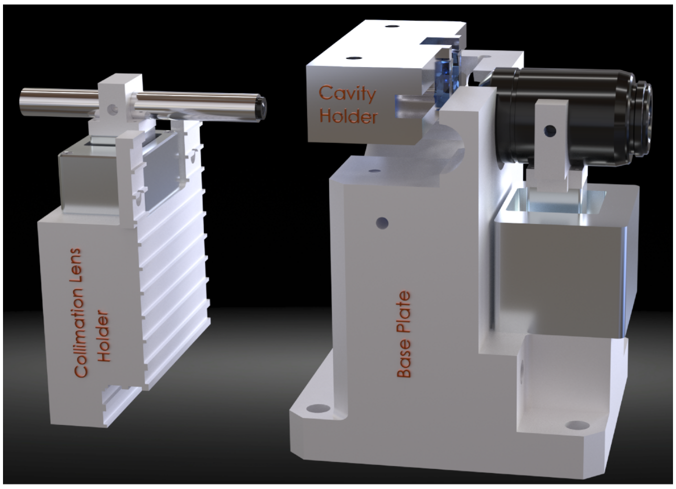

Figure 28: Renderings of the modular cavity assembly. The cavity holder is fully removable. The cavity mirrors are cut into strips to allow the tweezer trap to access the cavity mode. The microscope objective and recollimation lens are mounted on 3D nanopositioners.

4.2.3 *Optomechanical Cavity Design*

Despite being initially designed for a dispersively coupled experiment, the optomechanical cavity fulfills all the requirements for ground state cooling of particle motion via coherent scattering, even if some of its design choices are suboptimal for our current application. The cavity consists of two identical mirrors with a radius of curvature of $R_1 = R_2 = 10$ mm and a transmittance of $T_1 = T_2 = 20 \cdot 10^{-6}$. The mirrors are cut into stripes of 4 mm width from their initial 12.7 mm round substrate, such that the tweezer trap, formed by the microscope objective with a working distance of 3.4 mm, can reach the cavity mode. The mirrors are glued to a monolithic holder made of aluminum to form the optomechanical cavity with a length of $L \sim 10.7$ mm. The experimental assembly consists of three separate pieces: a joint base plate, the cavity holder, and the collimation lens holder. The joint base plate is screwed to the bottom of the vacuum chamber. The microscope objective is mounted on a 3D nano positioner, which itself is mounted on the base plate. The collimation lens is glued into a tube which can be pushed close to the tweezer focus. The tube is mounted on a 3D nano positioner, which is screwed to the collimation lens holder. The experiment's modular design allows the cavity holder to be removed for nanoparticle loading. To reinsert the cavity, the collimation lens holder is first unscrewed. The cavity holder is then carefully positioned by hand around the trapped particle on the base plate. Finally, the collimation lens holder is reinstalled by inserting its lens tube through a hole in the cavity holder and screwing it back onto the base plate, which clamps the cavity holder in place without a rigid connection. The cavity remains aligned with

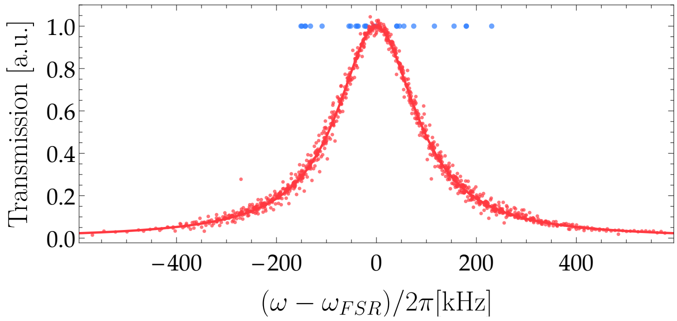

Figure 29: Multiple cavity resonance scans acquired over several months (red points). The free spectral range of each scan (blue) shows the drift of the cavity length. Each scan was shifted by its measured FSR to overlap. A joint fit of all data points is plotted (red line).

the external optics. With practice, this procedure can be performed with almost 100% success and without particle loss. Pictures of the cavity-tweezer assembly are shown in Figure 28.

4.2.4 *Free Spectral Range and Linewidth*

To measure the free spectral range ω_{FSR} and the cavity linewidth κ, we drive the coherent scattering mode with a laser at the tweezer frequency ω_1 through an input mirror, while the locking mode at frequency ω_2 is locked to the cavity resonance frequency. We measure the power of the transmitted light in the coherent scattering mode while scanning ω_1. Over the course of operating the system, we performed many such scans. As expected, we see the free spectral range drifting slightly from scan to scan. To get an accurate estimate of the linewidth, we collect all scans and overlay them by subtracting the free spectral range. We fit all data points together to get the linewidth $\kappa = 193 \pm 1$ kHz. The mean free spectral range computes to $\omega_{FSR}/2\pi = 14.0192$ GHz. The collected scans can be seen in Figure 29.

4.2.5 *Birefringence*

The fundamental requirement for coherent scattering is the overlap between the particle's scattered light mode and the cavity mode. The spatial overlap of the modes can always be achieved by external alignment of the tweezer mode. The polarization of the modes, however, is given by the geometry of the experiment. The tweezer must be vertically polarized to align the spatial modes, while the polarization of the cavity modes is fixed by its geometry. Stress on the cavity mirrors can induce birefringence, which makes cavity modes with orthogonal polarization non-degenerate. The orientation and polarization of those modes depend on the geometry and the applied stress. To be

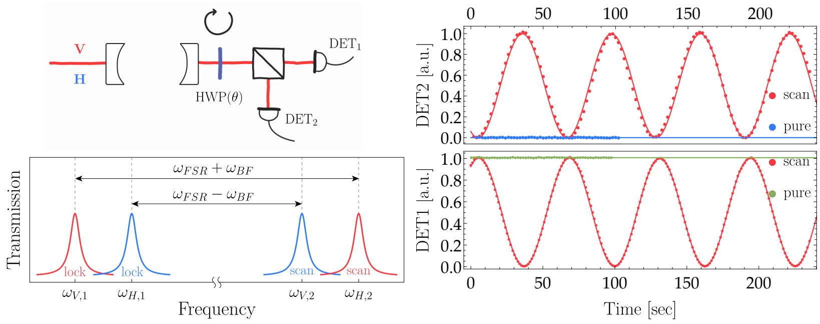

Figure 30: Measurement of cavity birefringence. The orientations of the two orthogonal cavity polarization eigenmodes are determined by locking the cavity to one mode and scanning the frequency of the other. The output polarization is analyzed with a rotating half-wave plate (HWP) and a polarizing beam splitter. The red trace shows the transmitted power versus HWP angle, confirming linear polarization. The blue/green trace, taken without the HWP, indicates alignment with the optical table. The frequency shift due to birefringence is measured by locking to one polarization mode and scanning to the next longitudinal mode with orthogonal polarization. The measurement is repeated with reversed polarization to obtain twice the splitting $2\omega_{BF}$.

able to collect all scattering off the nanoparticle with only one polarization cavity mode, the modes need to be aligned with the optical table — that is, horizontally and vertically polarized in the lab reference frame. Additionally, the two polarization modes have shifted resonance frequencies. The shift needs to be taken into account when setting the detuning of the tweezer drive to the cavity resonance. One of the polarization modes could be blue detuned when setting the optimal detuning for the other mode. Additional unwanted heating will arise if the tweezer light is blue detuned to one of the polarization modes, even if only weakly coupled.

To measure the polarization orientation, we first lock the cavity to a single polarization mode, confirmed by the PDH error signal showing only one set of peaks. We then place a rotating half-wave plate before a PBS at the output and record the transmitted and reflected power as the wave plate is rotated. The full visibility of this measurement confirms that the mode is linearly polarized. Removing the rotating wave plate and measuring all power at one PBS output then confirms that the mode is aligned with the optical table's reference frame. The measurement setup and results are shown in Figure 30. In hindsight, this orientation is expected, as the cutting and gluing of the cavity mirrors creates a strong directional bias. To measure the birefringence-induced frequency shift, we perform two measurements. First, we lock the cavity in the horizontal polarization mode at frequency ω_2 and drive the cavity with a secondary vertically polarized beam at frequency ω_1. We scan ω_1 until we find the next longitudinal cavity mode. Then, we repeat the measurement with reversed polarizations: locking to the vertical mode and scanning with a horizontal drive. The measured frequency difference in each case is $\omega_2 - \omega_1 = \omega_{FSR} \pm \omega_{BF}$. By combining these results, we determine the frequency shift due to birefringence to be $\omega_{BF}/2\pi \sim 200$ kHz.

4.2.6 *Positioning Stability*

The final mean occupation we can measure is directly impacted by our ability to stabilize the particle's position. The optimal position for cooling the motion along the cavity axis is an intensity node, as shown in Equation (134). We identify two main contributing factors to non-optimal positioning: long-term drifts of the cavity-tweezer alignment and vibrations originating from the pumping system.

First, the larger contribution is the drift in alignment of the tweezer with respect to the cavity node. The positioning can be actively corrected by moving the tweezer with the 3D nano positioner it is mounted on. The nano positioner has a step size of ~ 8 nm, which leads to a maximum distance from the cavity node of 4 nm. During measurement setup, we optimize the particle's position by minimizing the scattered power measured by the PowD detector (Section 4.2.2). However, once we begin recording heterodyne time traces, the flip mount redirects this light to the heterodyne detector. We optimize the position before every measurement. In post-processing, we extract the distance to a cavity node from the heterodyne spectrum to verify good positioning during the measurement. Imperfect suppression of elastically scattered photons creates a peak in the spectrum at the heterodyne frequency ω_{het}, which was omitted in the theory shown in Figure 7. The height of this peak is proportional to the product of the local oscillator and coherent scattering powers $P_{LO}P_{CS}$, which depends on the particle position as $\cos^2(x_0 k)$. We calibrate the measurement by moving the particle to a maximum and setting the measured peak height to one. By assuming the local oscillator power and the detection efficiency are constant, we can reconstruct the position during a cavity cooling measurement. A plot of the extracted position can be seen in Figure 31**b**. Note that the plotted signal is averaged to show only long-term drifts.

The second-largest source of positioning errors originate from vibrations of the pumping system, transferred via the bellow connecting the turbo pump and the vacuum chamber. The vacuum pumps excite vibrational modes in the bellow, which couple to the cavity-tweezer assembly. Distinct peaks appear in the spectra of the PDH error signal and the particle motion, with the most prominent at a frequency of 54 Hz. To mitigate the vibrations, we stiffen and damp specific modes of the bellow by adding modeling clay and foam at strategic positions. We identified these positions by applying pressure to the bellow by

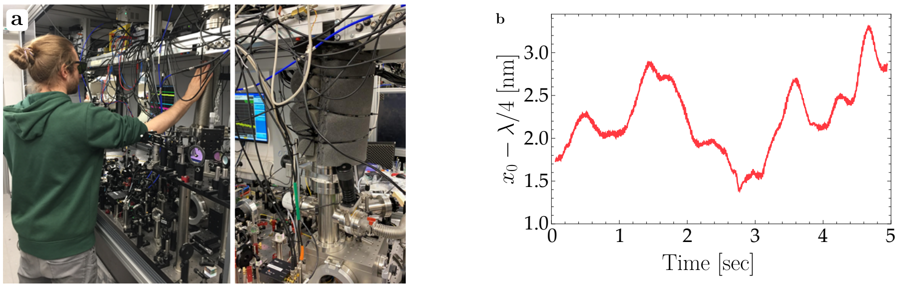

Figure 31: Positioning stability. **a** Manual damping of bellows vibrations to identify optimal locations for modeling clay and foam and bellows with damping applied. **b** Position extracted from the height of the heterodyne peak at ω_{het}. The signal is averaged to show long-term drifts only. The particle remains within 4 nm of the cavity node during the measurement.

hand and monitoring the PDH error signal for a reduction in mode amplitude. Figure 31**a** shows a picture of the damping of the bellow.

4.2.7 *Laser Phase Noise Heating*

The cavity can convert phase or frequency noise of the driving laser into intensity noise of the intracavity power. The intensity noise of the cavity field, like that of the trapping laser discussed in Section 4.1.3, can lead to additional heating of the particle's motion. The additional heating is proportional to the number of photons in the cavity mode, which depends on the position of the particle as $\cos^2(x_0 k)$. For our experimental parameters of $\Delta \sim \Omega_x = 2\pi$ 305 kHz with a particle positioned ~ 3 nm away from a cavity node, the added phonons to the particle occupation due to frequency noise is given by [35, 68, 102, 113]

$$n_{ph} = \frac{n_{photon}}{\kappa} S_{\dot{\phi}\dot{\phi}}(\Omega_x) < 0.025, \tag{154}$$

where $n_{photons}$ is the number of photons in the cavity mode. With a level of frequency noise from the Mephisto laser of $S_{\dot{\phi}\dot{\phi}}(\Omega_x) = 0.1$ Hz^2/Hz [60], the heating due to frequency noise is negligible.

4.2.8 *Pumping Speed and Mode-Hop Free Operation Time*

Loading particles via nebulizer has one main disadvantage: it prevents maintaining a clean vacuum environment. With every particle loading cycle, the vacuum chamber walls are saturated with water and isopropanol again, reducing pumping speed through outgassing. Since particles are typically lost at pressures of $\sim 10^{-3}$ mbar without additional stabilization, most of the vacuum pumping has to be done while some cooling of the center-of-mass motion is performed. In this experiment, we only employ cavity cooling, which is feasible since coherent scattering provides genuine three-dimensional coupling in-

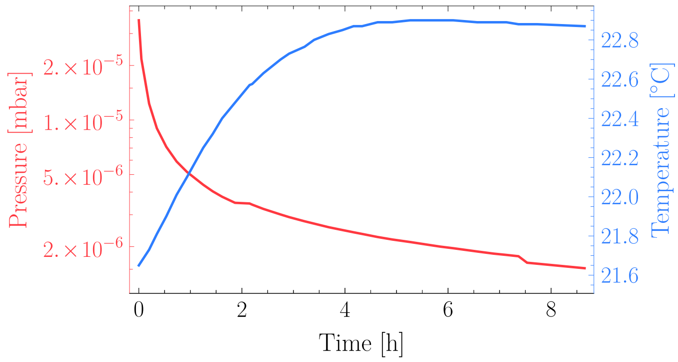

Figure 32: Science chamber pressure (red) and Mephisto laser crystal temperature (blue) over time. The laser must remain within its mode-hop-free range during a pumpdown. To mitigate drift, measurements were taken at night when ambient temperature changes counteracted vacuum-pumping induced drift.

dependent of the particle's position within the cavity. This, however, necessitates an engaged cavity lock for the whole evacuation process. As explained in Section 4.2.1, the cavity resonance frequency drifts freely with changes in length due to changes in the temperature of the cavity holder. Drifts due to the pressure dependent index of refraction of the medium are negligible in comparison. The laser frequency can only be tuned continuously between two mode hops. If the laser performs a mode hop, the cavity lock is lost, leading to a loss of particle cooling and subsequent particle loss. We experimentally confirm the mode hop free range by locking the cavity at a given laser temperature. We heat the cavity holder with thermal radiation through a vacuum window to facilitate a fast drift until the cavity lock is lost at a mode hop. We repeat this process to map out the mode hop structure of our specific laser model and find a mode hop free range of $\sim 3.2°$. According to the Operator's Manual Mephisto Lasers, this corresponds to a range of ~ 9.6 GHz in laser frequency. Reaching the typical measurement pressure of $\sim 10^{-6}$ mbar requires an evacuation time of up to 10 hours, during which the cavity length and laser crystal temperature drift continuously. We identify two main reasons for this drift. First, the reduced heat conductance of the surrounding medium at lower pressures, combined with the continuous heating from the tweezer laser, causes the holder's temperature to rise. Second, the holder responds to the inadequately regulated lab temperature, which itself oscillates with the day-night cycle. To keep the laser crystal temperature within its mode-hop-free range during evacuation, we first preheat the cavity holder with thermal radiation to a point just above a mode hop. We then lock the cavity, move the particle into the cavity mode, and begin the pumpdown process. The chamber is evacuated in two stages. First, a scroll pump (nXDS6i, Edwards) brings the pressure down to its base pressure of $\sim 10^{-2}$ mbar.

Then, we shut the valve to the scroll pump and open the gate valve to a turbo pump (nEXT300D, Edwards). To optimize the performance of our main turbo pump, we pre-pump it with a secondary turbo pump. To further mitigate temperature drifts, we utilize the natural turning point of the laboratory temperature during night times. We start the pump down around 20:00, such that measurement times fall into the early morning hours of 4:00 - 6:00 before the morning sun heats the building again. Constant monitoring of the locking setpoint is needed during the pumpdown due to the large drifts. We regularly adjust the offset of the locking signal to keep the PID regulator signal within its output range. An example of pressure and laser crystal temperature during a pump down can be seen in Figure 32.

4.2.9 *Tweezer - Cavity Detuning*

Optimal cooling of the nanoparticle motion is achieved at an optimal detuning $\Delta = \omega_{cav} - \omega_{tw}$ between the cavity resonance frequency ω_{cav} and the trapping beam frequency ω_{tw}. This is realized when the ratio between the cooling rate (photons scattered into the Stokes sideband) and the heating rate (photons scattered into the anti-Stokes sideband) is maximized. In the sideband-resolved limit ($\Omega_m \gg \kappa$), this optimum occurs at a detuning of $\Delta = \Omega_m$, where Ω_m is the frequency of the cooled mechanical mode. Setting the detuning accurately is crucial, but is complicated by cavity length drifts, which alter the detuning via changing the free spectral range. We devise a scheme to accurately determine the detuning during a measurement run. We drive the coherent scattering mode with a beam split off the trapping beam through one of the end mirrors. To create sidebands with an outward sweeping frequency, we modulate the drive with an EOM that is driven by a network analyzer (Rhode&Schwarz, ZNB8). We measure the cavity transmission with a photodiode and demodulate the signal with the network analyzer to determine the power at the sideband frequency. This allows us to accurately measure the current detuning and counteract any drifts. To not disturb the cooling performance by driving the coherent scattering mode, we shutter this beam whenever we do cooling measurements. A detuning scan and the measurement scheme are shown in Figure 33. In this example, we set the detuning to 500 kHz and measured an actual value of 454 kHz.

For the estimation of the final occupation, we need to determine the detuning for the recorded data. From Figure 7, we have learned that the spectrum shows asymmetry with respect to ω_{het} due to the cavity transmission function. For the residual phase noise and the purely

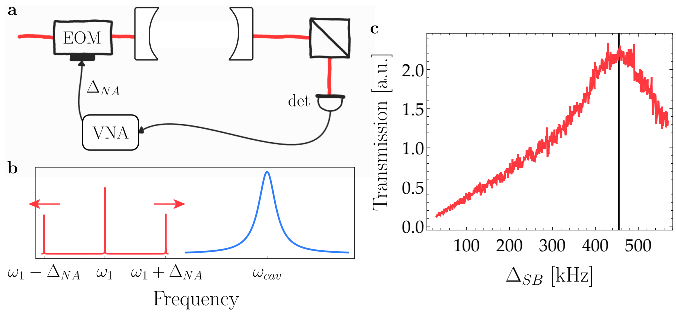

Figure 33: Detuning scan during a measurement run. **a** Scheme of the measurement. We drive the coherent scattering mode with a beam at the tweezer frequency. Two sidebands with sweeping frequency are generated by an EOM. We scan one sideband over the cavity resonance. The transmitted power is detected by a photo diode and demodulated by a network analyser (VNA). **c** The demodulated transmitted power shows a maximum at the cavity resonance. This measurement was done with an expected detuning of $\Delta_{set}/2\pi = 500$ kHz. The measurement shows the actual detuning drifted to $\Delta_{est}/2\pi \sim 454$ kHz.

classical z motion, this is the only asymmetry which depends on the detuning to the cavity mode as [34]

$$\frac{S_{het}(\omega_{het} + \omega)}{S_{het}(\omega_{het} - \omega)} = \frac{\left(\frac{\kappa}{2}\right)^2 + (\omega + \Delta)^2}{\left(\frac{\kappa}{2}\right)^2 + (\omega - \Delta)^2}. \tag{155}$$

We can estimate the detuning from a spectrum with an average error of ± 10 kHz, which is included in the estimation of the final motional occupation.

4.3 GROUND STATE COOLING

In this section, I will present the results of the experiment, discuss them, and provide an outlook for future applications. The relevant parameters are compiled in Table 1, and their calibration is described in the referenced sections.

Once the goal pressure of 10^{-6} mbar is reached, we begin the cooling measurement. First, we rotate the trap polarization to maximize scattering into the cavity mode. Then, we move the particle to a cavity node by minimizing the DC power in the coherent scattering mode. We perform a detuning scan to find the optimal cooling performance. At each detuning we take a long time trace to resolve the spectral peak of the heavily cooled x-motion above the background variance. Using a 16 ns sample interval and a total time trace length of up to 62.5 GSA, we achieve spectra with approximately 10^6 averages. To evaluate the data, we jointly fit the Stokes and anti-Stokes sidebands of the x-and y-motion to extract their amplitudes. The resulting spectra and fits for detunings of $\Delta/2\pi = 580 \pm 10$ kHz and $\Delta/2\pi = 275 \pm 1$

Name	Symbol	Value	Reference
diameter	d	143 nm	4.1.4
density	ρ	1850 kg / m^3	4.1.4
motional frequency	$(\Omega_x, \Omega_y, \Omega_z)$	$2\pi \cdot (305, 275, 80)$ kHz	4.1.1
cavity linewidth	κ	$2\pi \cdot 193$ kHz	4.2.4
cavity finesse	$\mathcal{F}$	73000	4.2.4
free spectral range	ω_{FSR}	$2\pi \cdot 14.0192$ GHz	4.2.4
cavity length	L	1.07 cm	4.2.3

Table 1: Summary of experimental parameters. Details can be found in the referenced sections.

kHz are shown in Figure 34. We determine the final occupation n_x via sideband thermometry

$$\frac{S_{het}(\omega_{het} + \Omega_x) - 1}{S_{het}(\omega_{het} - \Omega_x) - 1} = \frac{n_x}{n_x + 1} \frac{\left(\frac{\kappa}{2}\right)^2 + (\Delta + \Omega_x)^2}{\left(\frac{\kappa}{2}\right)^2 + (\Delta - \Omega_x)^2}, \tag{156}$$

where we use the amplitudes of the broad peak attributed to the x-motion. The plot of final mean occupation versus detuning (Figure 34b) shows a minimum at $\Delta/2\pi = 315$ kHz. At this detuning, we measure a mean occupation of $\bar{n}_x = 0.43 \pm 0.03$ phonons, corresponding to a 70 ± 2 % probability of finding the motion in the ground state. The steady state final occupation is reached when the total heating rate Γ_x is balanced by the cooling rate $\bar{n}_{fin} \times \gamma$, where γ is the linewidth of the motional sidebands. The observed sideband imbalance in the spectrum is present due to additional heating, which must be compensated by a stronger cooling sideband. In a system without this additional heating, the sidebands amplitudes would be equal. By independently measuring the linewidth of the sidebands and the final occupation, we estimate a total heating rate of $\Gamma_x/2\pi = 20.6 \pm 2.3$ kHz. This rate is dominated by heating from gas collisions, which we estimate from previous calibrations [56] to be $\Gamma_{gas}/2\pi = 16.1 \pm 1.2$ kHz. Additional contributions include photon recoil and laser phase noise, which we estimate to be $\Gamma_{recoil}/2\pi \sim 6$ kHz and $\Gamma_{pn}/2\pi < 200$ Hz. The green band in Figure 34b shows the predicted cooling performance from optomechanics theory [51], based on our independently measured system parameters. Measurement errors, together with pressure drifts during the measurements, are taken into account in the theoretical plot. We can also apply this theory to estimate the cooling performance at the recoil limit, when heating from gas collisions is negligible. The dark green line indicates the predicted phonon occupation at pressures below 10^{-8} mbar.

To estimate the phonon occupation of the y-motion, we fit the sidebands attributed to its motion and extract the damping rate of $\gamma_y/2\pi = 0.5$ kHz. Combining this with the estimated heating rate of $\Gamma_y/2\pi \sim 20$

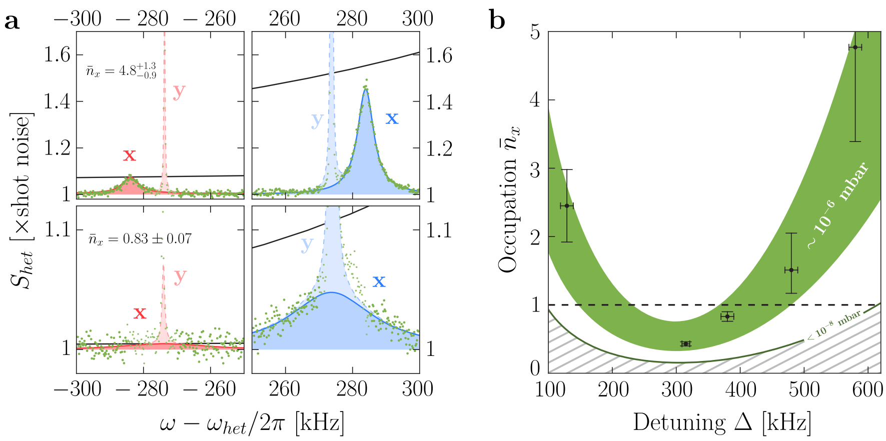

Figure 34: Sideband thermometry of particle motion. **a** Heterodyne spectra around the Stokes (left, red) and anti-Stokes (right, blue) sidebands. Fits to the contributions of the x-mode are shown as solid lines. The contribution of the residually coupled y mode is plotted in lighter colors, with dashed-line fits. The cavity response function, scaled to the Stokes sideband power, is shown as a solid black line. Spectra at detunings $\Delta/2\pi = 580 \pm 10$ kHz (top) and $\Delta/2\pi = 275 \pm 1$ kHz (bottom) are shown. In the bottom plot, the anti-Stokes sideband amplitude is visibly reduced relative to the cavity transmission function due to stronger cooling. The final occupation n_x is calculated from the ratio of the sideband amplitudes after removing the cavity envelope and is indicated in the plots. **b** Final occupation n_x versus tweezer–cavity detuning Δ. Data points are derived from the sideband asymmetry of the heterodyne spectra. Error bars incorporate uncertainties in the laser detuning, the cavity decay rate, and the errors of the fit. The lowest occupation, $n_x = 0.43 \pm 0.03$, is reached near the optimal detuning of $\Delta/2\pi = 315$ kHz. The green band represents a theoretical model based on independently measured system parameters, including pressure drifts during the measurement. The dark green curve indicates the theory prediction for the final occupation at the recoil limit for pressures below 10^{-8} mbar.

kHz yields a final occupation of $\bar{n}_y < 100$ phonons across all detunings.
Because the particle is positioned near a cavity node, the z-motion is only cooled minimally. Due to its high occupation, we observe higher harmonics in the spectrum. After removing the cavity response function, the ratio of the area of the first two harmonics is given by

$$\frac{g_{quad}}{g_{lin}} \frac{\langle z^4 \rangle}{\langle z^2 \rangle} = \frac{k_B T_z}{m \Omega_z^2} \left(\frac{k - 1/z_R}{2} \right)^2, \tag{157}$$

where $m = 2.83$ fg is the mass of the particle, k_B is the Boltzmann constant, $k = 2\pi/\lambda$ is the wavenumber with $\lambda = 1064$ nm, $z_R = W_x W_y \pi/\lambda$ is the Rayleigh range with the tweezer waists of $W_x = 0.67$ µm and $W_y = 0.77$ µm. At a detuning of $\Delta/2\pi = 315$ kHz, the average temperature is $T_z \sim 80$ K, corresponding to an occupation of $n_z = k_B T_z/(\hbar \Omega_z) = 2 \cdot 10^7$ phonons. While the occupation fluctuates substantially between runs, it is consistently cooled enough to remain stably trapped.

4.3.1 *Discussion and Outlook*

The results presented here are the first demonstration of cooling a levitated nano particle to its motional quantum ground state in a room temperature environment. The evaluation and theory presented here are a simple treatment considering the three center of mass motions of the particle as one dimensional and independent. Caution must be taken due to the high coupling rates and similar oscillation frequencies of the x- and y-motion. Cross coupling and mode hybridization [125] can lead to a spectral component of the x-motion at the frequency of the y-motion. In this case the one dimensional treatment underestimates the final occupation. As a worst case scenario we estimate the final occupation by integrating the area of the spectrum in a band of $\pm(250 - 300)$ kHz over both the broad peak attributed to x-motion and the narrow peak attributed to y-motion and obtain a final occupation of $n_{wc} = 0.91 \pm 0.04$ phonons. This treatment overestimates the occupation but still demonstrates ground state cooling.
The experimental apparatus used here has technical limitations in many areas. Improving the final vacuum pressures and reducing pump times would benefit the experiment greatly. To accomplish that a clean loading technique like hollow core fiber loading must be implemented or the cavity mirrors need to be protected from contamination such that the vacuum chamber does not need to be vented for particle loading.
Enhancing vibration isolation and positioning stability can be achieved by implementing better damping. Drifts of the tweezer relative to the cavity standing wave can be mitigated through a monolithic holder design. Drift of the cavity standing wave due to length variations can

be reduced by fabricating the holder from a low-expansion material such as Zerodur or Invar. Additionally, stabilizing the cavity length to an ultrastable laser would extend lock lifetimes.

To optimize detection, high quantum efficiency detectors should be used. The optomechanical cavity should be implemented in a single-sided geometry to enable efficient collection of all light scattered by the particle. Locking the cavity with a TEM01 mode would further reduce the particle's interaction with the locking mode. However, modifying other cavity parameters is nontrivial and must be considered in light of the experiment's objectives. Moderate increases in finesse would improve cooling, whereas excessively high finesse would raise the final occupation again. Reducing the mode volume and waist will enhance the coupling strength. Theoretical treatment that includes strong, ultra-strong, or deep-strong coupling is required to assess the resulting effects depending on the final system parameters.

Operating the experiment in a cryogenic environment would mitigate heating from blackbody radiation and provide cryogenic vacuum conditions.

The presented results pave the way for room-temperature quantum experiments with levitated nanoparticles, enabling the implementation of more complex quantum states. Extension to multimode operation, either by coupling multiple degrees of freedom of a single particle or by coupling multiple particles to the cavity mode, is feasible. Entanglement of particle motion may be achievable for tests of fundamental physics. Levitation experiments also offer advantages for sensing applications that demand high mass and high positional resolution.

Part II

NON-HERMITIAN DYNAMICS OF OPTICALLY COUPLED NANOPARTICLES

5 INTRODUCTION: OPTICALLY COUPLED NANOPARTICLES

The scattering produced by an optically induced dipole in a nanoparticle can be leveraged in multiple ways. In the previous part of this thesis, we used it for cooling the particle motion via coherent scattering into a cavity. Here, we implement a mutual coupling between two particles by interfacing their dipole scattering. Light scattered from one particle modifies the local electromagnetic field at the position of the second, coupling their motion via the light-induced dipole–dipole interaction.

The use of light-mediated forces has a long history across diverse platforms [37]. Early work focused on colloidal microparticles. In such systems, particles suspended in liquid are typically illuminated by a broad, common laser beam. The scattered light generates an effective, collective potential landscape that depends on both particle number and configuration, giving rise to self organization and pattern formation phenomena [15, 118, 120]. These effects are due to optical binding forces, often treated as a conservative interaction. However, since light carries momentum, appropriately engineered optical fields can produce non-conservative forces. This has enabled, for example, optical sorting and separation of microparticles [13] and the emergence of self-sustained oscillations in optically bound chains [14]. However, suspension in liquid introduces strong viscous damping that removes particle inertia from the dynamics, and the lack of individual control and readout of particle positions, together with limited tunability of the optical field parameters, greatly limits the observable effects.

Recent advances have extended the study of optical binding and light-induced dipole-dipole interactions to nanoparticles in vacuum, where the reduced environmental damping reveals the underlying coupled dynamics [6, 17, 77, 107, 119]. The use of individually trapped nanoparticles in separate optical tweezers enables fine control of both the light fields and particle positions, making the non-Hermitian, nonlinear nature of the interaction accessible.

In this part of the thesis, we demonstrate the non-reciprocal and nonlinear nature of the light-induced dipole-dipole interaction using two nanoparticles trapped in parallel optical tweezers. We show that arrays of trapped nanoparticles are a platform of multiple, individually addressable oscillators with programmable couplings. By appropriately choosing system parameters, we realize a fully anti-reciprocal coupling. We observe $\mathcal{PT}$-symmetry breaking, a Hopf bifurcation, and a transition to mechanical lasing of the collective particle motion. These results show that this system may be used to test complex many-body physics [59, 137] and non-equilibrium physics [72, 75]. Furthermore, the ability to cool and precisely control individual oscillators [76] opens pathways toward quantum optical binding [110], with prospects for exploring topological effects [30, 97, 98], entanglement [12, 25, 112], and collective quantum phenomena [80].

This chapter is organized as follows. Section 6 extends the theory presented in Section 3 to a pair of interacting nanoparticles in parallel optical tweezers. Section 7.1 introduces the experimental platform and gives details on alignment and calibration. Section 7.2 presents the results, which are discussed in Section 7.3.

6 THEORY FOR LIGHT-INDUCED INTERACTION

The theory for trapping a single nanoparticle is provided in the previous part. Here, we extend the treatment to two nanoparticles trapped in parallel optical tweezers. The key ingredient for understanding the presented experiment is the light-induced dipole-dipole interaction, for which we provide a model. The setup consists of two parallel optical tweezers, with a nanoparticle trapped in each focus. The coherently scattered light between the particles interferes with the local trapping light to induce a force on each nanoparticle that depends on both particle positions. This force gives rise to a three-dimensional, nonlinear, non-reciprocal coupling of the center of mass motion. We will simplify the model to linear dynamics of the center-of-mass motion along the tweezer propagation axis, governed by a non-Hermitian dynamical matrix. This theory gives a basic understanding of the dynamics we observe experimentally. Nonetheless, we observe nonlinear effects beyond the scope of the theory presented here. For a more rigorous, nonlinear treatment, see [37, 110, 111].

6.1 SYSTEM MODEL — TWO INTERACTING PARTICLES

In this section, we derive the linear, non-Hermitian dynamics of two identical nanoparticles trapped in parallel optical tweezers. Although light-induced forces between particles have been studied [26, 37], the case of particles trapped in two distinct, parallel optical tweezers has not been analyzed. Here, we extend the treatment to this configuration and show that it provides non-reciprocal coupling. A sketch of the system is shown in Figure 35.

To calculate the total forces acting on each particle, we first require the total electric field at the position of each particle. The model consists of two parallel optical tweezers described by Gaussian beams. Each

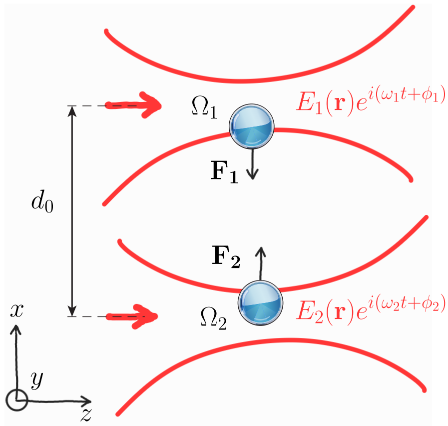

Figure 35: Light-induced dipole-dipole interaction. Two particles are trapped in parallel optical tweezers at a mean distance of d_0. The forces $\mathbf{F}_1$ and $\mathbf{F}_2$ are in general non-reciprocal and non-Hermitian.

particle coherently scatters light to the trapping position of the other particle, such that the total field is given by the interference between the trapping light and the scattered light. The particles are trapped at positions $\mathbf{r}_1$ and $\mathbf{r}_2$, respectively. The force on the particle at $\mathbf{r}_1$, averaged over one full oscillation of the electromagnetic field, is given by [26, 37]

$$\langle \mathbf{F}(\mathbf{r}_1)\rangle = \frac{1}{2}\mathrm{Re}\left[\mathbf{p}^*(\mathbf{r}_1)\left(\nabla\mathbf{E}(\mathbf{r})\right)\big|_{\mathbf{r}=\mathbf{r}_1}\right], \tag{158}$$

where $\mathrm{Re}[R]$ is the real part of R, $\mathbf{p}^*(\mathbf{r})$ is the complex conjugate of the dipole moment $\mathbf{p}$ of the particle at position $\mathbf{r}$, and $\mathbf{E}$ is the total electric field. The total electric field at the positions of the particles is given by

$$\mathbf{E}(\mathbf{r}_1) = \mathbf{E}^{I}(\mathbf{r}_1) + G(\mathbf{r}_1-\mathbf{r}_2)\alpha\mathbf{E}(\mathbf{r}_2), \tag{159}$$
$$\mathbf{E}(\mathbf{r}_2) = \mathbf{E}^{I}(\mathbf{r}_2) + G(\mathbf{r}_2-\mathbf{r}_1)\alpha\mathbf{E}(\mathbf{r}_1), \tag{160}$$

where $\mathbf{E}^{I}(\mathbf{r})$ is the incident electric field at position $\mathbf{r}$, α is the polarizability of the particles, and $G(\mathbf{r})$ is the Green's tensor of the transverse Helmholtz equation. It is given by

$$G(\mathbf{r}) = \frac{e^{ikr}}{4\pi}\left[(1-ikr)\frac{3\mathbf{r}\otimes\mathbf{r}-r^2\mathbb{1}}{r^5} + k^2\frac{r^2\mathbb{1}-\mathbf{r}\otimes\mathbf{r}}{r^3}\right], \tag{161}$$

where $r=|\mathbf{r}|$ and $\otimes$ denotes the outer product. The second term in Equation (159) describes the electric field scattered from the particle at position $\mathbf{r}_2$ to the particle at position $\mathbf{r}_1$. Substituting Equations (159) and (160), together with Equation (161), into Equation (158) yields

$$\langle \mathbf{F}(\mathbf{r}_1)\rangle = \frac{1}{2}\mathrm{Re}\left[\alpha\mathbf{E}^{I}(\mathbf{r}_1)\cdot\nabla\mathbf{E}^{I}(\mathbf{r}_1)\right.$$
$$\left. +\alpha^2\nabla\left(\mathbf{E}^{I}(\mathbf{r}_1)\cdot G(\mathbf{r}_1-\mathbf{r}_2)\mathbf{E}^{I}(\mathbf{r}_2)\right)\right], \tag{162}$$

where we use $\mathbf{p}(\mathbf{r}_1)=\alpha\mathbf{E}(\mathbf{r}_1)$ and keep only terms to $\mathcal{O}(\alpha^2)$. The first term depends only on the incident field at $\mathbf{r}_1$ and describes the trapping forces of the tweezer. Since these were treated in Section 3.3, we omit them below. The second term describes the so-called optical binding force, which originates from the interference between the local trapping field and the scattered field. We consider only dynamics along the tweezer axis, which is well isolated from the others and can be treated independently. We model the incident electric field $\mathbf{E}^{\mathrm{I}}(\mathbf{r})$ as two parallel, focused Gaussian beams that propagate in the z direction and share the same linear polarization. For particles deeply trapped in the beam foci, the fields can be approximated locally as $\mathbf{E}^{\mathrm{I}}(\mathbf{r}_{1,2}) \approx \mathbf{E}_{1,2}\exp(ikz_{1,2} - iz_{1,2}/z_R + i\phi_{1,2})$, where $\phi_{1,2}$ are the local optical phases at the tweezer foci. The inter-particle distance is assumed to be large ($d = |\mathbf{r}_1 - \mathbf{r}_2| \gg 1/k$) such that the first term of the Green's tensor can be omitted. The optical binding force $\mathbf{F}_{1,2}$ on particle 1 and particle 2 is approximated as

$$\mathbf{F}_{1,2} \approx \frac{|\mathbf{E}_1||\mathbf{E}_2|\alpha^2 k^2}{8\pi\varepsilon_0 d}\cos^2\theta\sin(kd \pm \Delta\phi)\left(\pm k\mathbf{n} + \left(k - \frac{1}{z_R}\right)\mathbf{e}_z\right), \tag{163}$$

where ε_0 is the vacuum permittivity, $\pi/2 - \theta$ is the angle between the polarization direction of the trapping beams and the axis connecting the particles, $\Delta\phi = \Delta\phi_0 - (k - 1/z_R)(z_1 - z_2)$ is the optical phase difference at the particle positions, with $\Delta\phi_0 = \phi_2 - \phi_1$ and $\mathbf{n} = (\mathbf{r}_1 - \mathbf{r}_2)/d$. The force is generally non-reciprocal ($\mathbf{F}_1 \neq -\mathbf{F}_2$) and non-Hermitian. Energy and momentum in the two-particle system are not conserved and are constantly supplied and taken away by the optical fields.

As a next step, we simplify the dynamics to the linear regime, which is illustrated in Figure 36. We express the equations using the complex amplitudes $a_j = (z_j + ip_j/m\Omega_j)\exp(i\Omega_0 t)/2z_{zpf,j}$ for particle j with position z_j, momentum p_j, mass m, and zero-point fluctuation $z_{zpf,j} = \sqrt{\hbar/2m\Omega_j}$. Expanding the force around the trapping positions yields linearized equations of motion for the z motion in a frame rotating at the mean mechanical frequency $\Omega_0 = (\Omega_1 + \Omega_2)/2$, averaged over one mechanical cycle $2\pi/\Omega_0$

$$\frac{d}{dt}\begin{pmatrix} a_1 \\ a_2 \end{pmatrix} = -iH_{NH}\begin{pmatrix} a_1 \\ a_2 \end{pmatrix} + \sqrt{\gamma n_T}\begin{pmatrix} \xi_1 \\ \xi_2 \end{pmatrix}. \tag{164}$$

Gas damping and diffusion are added by the complex white noise ξ_j with the damping rate γ, the thermal occupation n_T, and correlations $\langle \xi^*_{j'j}(t')\xi_j(t)\rangle = \delta_{jj'}\delta(t'-t)$ and $\langle \xi_{j'}(t')\xi_j(t)\rangle = 0$. The non-Hermitian dynamical matrix is given by

$$H_{NH} = \begin{pmatrix} -\frac{\Delta\Omega}{2} + g_r + g_a - i\frac{\gamma}{2} & -(g_r + g_a) \\ -(g_r - g_a) & \frac{\Delta\Omega}{2} + g_r - g_a - i\frac{\gamma}{2} \end{pmatrix}, \tag{165}$$

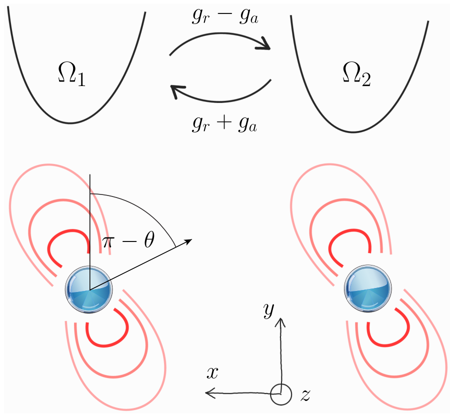

Figure 36: Two particles with oscillation frequencies Ω_1 and Ω_2 are coupled asymmetrically: $g_r - g_a$ in one direction and $g_r + g_a$ in the other. The coupling strength depends on the polarization angle θ.

with $\Delta\Omega = \Omega_2 - \Omega_1$. The coupling is introduced via g_r (reciprocal, conservative) and g_a (anti-reciprocal, non-conservative), defined by

$$g_r = \frac{G}{kd_0}\cos(kd_0)\cos(\Delta\phi_0), \tag{166}$$

$$g_a = \frac{G}{kd_0}\sin(kd_0)\sin(\Delta\phi_0), \tag{167}$$

which depend on the mean particle distance d_0 and the constant

$$G = \frac{\alpha^2 k^5 |E_1||E_2|}{16\pi\varepsilon_0\Omega_0}\cos^2\theta. \tag{168}$$

The coupling rates decrease as $1/d_0$. Their overall strength depends on the trapping beam field strengths $E_{1,2}$ and can be tuned by adjusting the polarization angle θ of the trapping fields. Experimentally, both the distance d_0 and the optical phase $\Delta\phi_0$ can be chosen independently. The coupled system forms normal modes with frequencies $\Omega_\pm = \Omega_0 + \mathrm{Re}[\lambda_\pm]$ and damping rates $\gamma_\pm = -2\mathrm{Im}[\lambda_\pm]$ given by the eigenvalues of the dynamical matrix H_{NH}

$$\lambda_\pm = \frac{1}{2}\left(2g_r - i\gamma \pm \Lambda\right), \tag{169}$$

with $\Lambda = \sqrt{4g_r^2 - 4g_a\Delta\Omega + \Delta\Omega^2}$. For $g_a < g_r$ the system exhibits normal mode splitting. For $g_a = g_r$, the coupling rates cancel out in one-direction while they add up in the other direction, yielding one directional coupling. For $g_a > g_r$, the parameter Λ becomes imaginary when $\Delta\Omega$ lies between Ω_l and Ω_r, where $\Omega_{l,r} = 2g_a \pm 2\sqrt{g_a^2 - g_r^2}$. Consequently the system shows normal mode attraction. The two eigenfrequencies coalesce into a single value while the damping rates split. The frequencies and damping rates for the three different cases are plotted in Figure 37. The eigenvectors of the dynamical matrix are

$$\mathbf{v}_\pm = \begin{pmatrix} 2g_a - \Delta\Omega \pm \Lambda \\ 2(g_a - g_r) \end{pmatrix}. \tag{170}$$

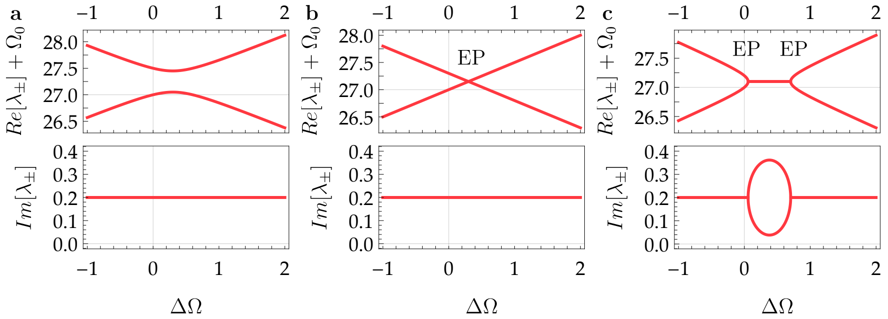

Figure 37: Frequencies and damping rates of the normal modes of H_{NH}. **a** ($g_a < g_r$) The system exhibits normal mode splitting. **b** ($g_a = g_r$) One directional coupling leads to one exceptional point (EP) where the normal modes frequencies cross. **c** ($g_a > g_r$) There is normal mode attraction for the frequencies and splitting of the damping rates in between the exceptional points (EP).

In general, reconstructing the eigenvectors from the motion of the individual oscillator requires characterizing the coupling rates. For the special case of $g_r = 0$ ($g_a = 0$), at a detuning of $\Delta\Omega = 2g_a$ ($\Delta\Omega = 0$), the eigenvectors become independent of the coupling rates and we can reconstruct the normal modes as $a_\pm = a_1 \pm i a_2$ ($a_\pm = a_1 \pm a_2$). The corresponding eigenmodes in position space are $z_\pm = z_1 \mp i z_2$ ($z_\pm = z_1 \mp z_2$). The sign flip arises from the definition of the complex amplitudes a_j. At the edges of the region of normal mode attraction $\Delta\Omega = \Omega_{l,r}$, the eigenvalues $\lambda_\pm$ and eigenvectors $\mathbf{v}_\pm$ coalesce, which gives rise to two exceptional points.
The matrix H_{NH} is symmetric with respect to generalized parity and time reversal, except for the region between the exceptional points where $\mathcal{PT}$-symmetry is broken because the eigenmodes have different damping rates [48]. In this regime, the mode a_+ is amplified while the mode a_- is suppressed. We determine whether the system is in the $\mathcal{PT}$-symmetric phase or the $\mathcal{PT}$-symmetry broken phase by analyzing the autocorrelation function [105], given by

$$\begin{aligned} g_{jj}^{(1)}(\Delta t) &= \langle a_j^*(t) a_j(t+\Delta t)\rangle \\ &= n_T \left[\left(1 + \frac{4g_a(g_a \pm g_r)}{\gamma^2 + \Lambda^2}\right) \cos\left(\frac{\Lambda}{2}\Delta t\right) \right. \\ &+ \frac{4\gamma g_a(g_a \pm g_r)}{\Lambda(\gamma^2+\Lambda^2)} \sin\left(\frac{\Lambda}{2}|\Delta t|\right) \\ &\pm \left. i\frac{\Delta\Omega - 2g_a}{\Lambda} \sin\left(\frac{\Lambda}{2}\Delta t\right)\right] e^{-i g_r \Delta t} e^{-\frac{\gamma}{2}|\Delta t|}. \qquad (171) \end{aligned}$$

In the $\mathcal{PT}$-symmetry broken phase, the parameter Λ becomes imaginary. Writing $\Lambda = iR$ with $R > 0$, the oscillatory terms transform as $\cos(\Lambda t) \to \cosh(Rt)$ and $\sin(\Lambda t) \to i \sinh(Rt)$. When combined with the natural damping γ, these contributions yield purely exponential behavior with two distinct decay rates, so the total autocorrelation

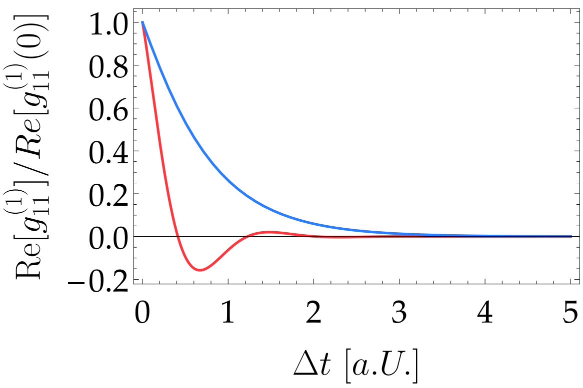

Figure 38: Normalized autocorrelation function $g_{11}^{(0)}(\Delta t)$ illustrating the effect of the coupling rate g_a. A small g_a (red) leads to oscillatory behavior, indicative of the $\mathcal{PT}$-symmetric phase. A larger g_a (blue) leads to bi-exponential decay, indicative of the $\mathcal{PT}$-symmetry broken phase.

function decays bi-exponentially. A plot of the normalized autocorrelation function $g_{11}^{(0)}(\Delta t)/g_{11}^{(0)}(0)$ is shown in Figure 38. Two theoretical curves are plotted for different coupling rates g_a, where one shows oscillatory behavior and the other shows bi-exponential decay.
To characterize the joint motion of the two particles, we write their complex amplitudes as $a_{1,2} = |a_{1,2}|e^{-i\psi_{1,2}}$, introducing the motional amplitudes $|a_{1,2}|$ and the mechanical phases $\psi_{1,2}$. The interaction, and to a lesser extent thermal fluctuations, induce a preferred mechanical phase delay $\psi = \psi_2 - \psi_1$. In the linear regime, this phase delay can be calculated via the cross correlation function, which incorporates the phase delay stemming form the interaction and form the thermal fluctuations as

$$\psi = \mathrm{Arg}\left(g_{12}^{(1)}(0)\right), \tag{172}$$

where the cross-correlation function is given by

$$\begin{aligned} g_{12}^{(1)}(\Delta t) &= \langle a_2^*(t) a_1(t+\Delta t)\rangle \\ &= n_T \left[\frac{2g_a(i\gamma + 2g_a - \Delta\Omega)}{\gamma^2 + \Lambda^2}\left\{\cos\left(\frac{\Lambda}{2}\Delta t\right)\right.\right. \\ &+ \left.\frac{\gamma}{\Lambda}\sin\left(\frac{\Lambda}{2}|\Delta t|\right)\right\} \\ &+ \left. i\frac{2g_r}{\Lambda}\sin\left(\frac{\Lambda}{2}\Delta t\right)\right] e^{-ig_r\Delta t} e^{-\frac{\gamma}{2}|\Delta t|}. \end{aligned} \tag{173}$$

The linear model breaks down once the total damping of the amplified mode γ_+ switches sign at the threshold coupling rate of

$$g_{a,th} = \frac{4g_r^2 + \gamma^2 + \Delta\Omega^2}{4\Omega}, \tag{174}$$

at which point the model would predict an exponentially growing oscillation amplitude. In reality, the amplitude increases only until higher-order nonlinear terms become significant and stabilize the motion again. For the light-induced dipole-dipole interaction, the stabilizing nonlinearity is provided by the interaction itself.

A fully analytical nonlinear description of the joint particle motion can be obtained by introducing the joint motional amplitude $A = 2k\sqrt{\hbar/(m\Omega_0)}\sqrt{|a_2|^2+|a_1|^2}$ and the mechanical phase delay ψ. The resulting model consists of two coupled differential equations [105, 110, 111]

$$\dot{A} = -\frac{\gamma}{2}A + g_a A\sin(\psi) f\left(A\sin\frac{\psi}{2}\right), \tag{175}$$

$$\dot{\psi} = \Delta\Omega - 4g_a\sin^2\left(\frac{\psi}{2}\right) f\left(A\sin\frac{\psi}{2}\right), \tag{176}$$

A detailed derivation is beyond the scope of this thesis. The results together with the experimental comparison, including the nonlinear model, are presented in Section 7.

7 NON-HERMITIAN DYNAMICS – THE EXPERIMENT

In this section, I present the experimental implementation of two trapped nanoparticles coupled via light-induced dipole-dipole interaction. We focus on anti-reciprocal coupling even though the acousto-optic deflector-based platform presented here is capable of generating more complex interactions. We observe collective motion with signatures of $\mathcal{PT}$-symmetry breaking and we show how the non-conservative nature of the interaction drives the collective motion into a nonlinear regime. We see a transition into limit-cycle motion after a threshold interaction strength is exceeded, which can be understood as a second-order (non-Hermitian) phase transition.
This part of the thesis is structured in the following way: I will start by giving an overview of the experimental apparatus, explaining the trap-creation scheme in Section 7.1.1 and how the motion of the individual particles is measured in Section 7.1.2. I will provide details on the calibration of the various system parameters, including the mean trapping distance in Section 7.1.5, the number of charges attached to the particles in Section 7.1.7, and the difference in particle size in Section 7.1.8. Finally, I will present the results showing non-Hermitian dynamics and non-reciprocity of the joint nanoparticle motion, followed by a discussion.

7.1 EXPERIMENTAL APPARATUS

We use an Nd:YAG laser (Innolight Mephisto, wavelength $\lambda = 1064$ nm) as the light source. Its output is amplified by a fiber amplifier (Azurlight Systems, maximum output of 10 W) to approximately 7 W. About 5% of the power is picked off using a half-wave plate (HWP) and a polarizing beam splitter (PBS) to serve as the local oscillator for the detection scheme, which is discussed in Section 7.1.2. The rest of the light is used to generate the trap array by two crossed acousto-optic deflectors (AODs). The traps created in this way are highly tunable, allowing us to adjust the mean interparticle distance d_0, the phase difference of the trapping beams in the trapping plane $\Delta\phi_0$, and the particle oscillation frequencies $\Omega_{1,2}$.

7.1.1 *Trap Array Creation*

We use two perpendicularly oriented AODs (AA Opto- electronic, DTSXY-400-1064) to generate an array of output beams, which are imaged to the trapping plane to form parallel optical tweezers, where

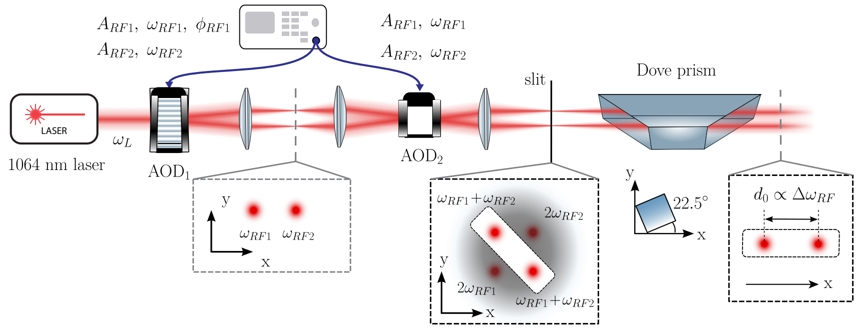

Figure 39: Creation of the trapping beams using two crossed AODs. Each AOD is driven with two drive tones, generating a 2×2 array of beams at the output of the second AOD. The optical frequency shifts relative to the input laser frequency ω_L is indicated in the boxes at the marked positions. The two beams with unequal optical frequencies are blocked by a spatial filter (slit), and the remaining pair is rotated with a Dove prism to align with the optical table. Optical power, beam separation, and relative phase are controlled via the drive amplitudes A_{RF1} and A_{RF2}, the frequencies ω_{RF1} and ω_{RF2}, and the phase ϕ_{RF1} of the AOD inputs.

we trap two silica nanoparticles with a nominal radius of $r = 105 \pm 2$ nm. Figure 39 shows a sketch of how the trapping beams are generated. The AODs diffract an input beam with an angle θ_{AOD} that depends on the AOD's drive frequency ω_{RF}, given approximately by

$$\theta_{AOD} \approx \frac{\lambda\omega_{RF}}{2\pi c_s}, \tag{177}$$

where λ is the wavelength of the deflected laser and c_s is the speed of the sound waves in the AOD crystal. The deflectors are mounted on separate 5-axis translation stages (Thorlabs, PY005/M) to enable precise alignment of each AOD. The first AOD is oriented horizontally and driven by a laser beam with a diameter of approximately 2 mm and optical frequency ω_L. Two lenses ($f = 25$ mm) conjugate the plane where the beams are deflected in the first AOD to that of the second. The second AOD is rotated by 90° relative to the first to deflect the beams vertically. To create four output beams after the second AOD, we drive both AODs with two tones with frequencies ω_{RF1} and ω_{RF2}. Hence, there are two beams with a relative angle of $\Delta\theta_{AOD}$ at the output of the first AOD. In the second AOD, each of those beams is diffracted again into two first-order beams with the same relative angle. Therefore, we create a minimal 2x2 array of laser beams at the output of the second AOD.

In addition to the impact on the output angle, the diffraction in the AOD crystals causes a frequency and phase shift in the output beam equal to the frequency and phase of the drive tone. When both AODs are driven by tones with the same frequencies, two output beams share the final optical frequency of $\omega_L + \omega_{RF1} + \omega_{RF2}$, while the other two have frequencies $\omega_L + 2\omega_{RF1}$ and $\omega_L + 2\omega_{RF2}$. The light-induced dipole-dipole interaction relies on the interference of the trapping beams. Accordingly we select the two beams with equal optical frequency and block the other two. To achieve this, the four output beams of the second AOD are focused by a lens with focal length $f_1 = 250$ mm. In the focal plane, each beam is focused to a distinct spot arranged in a square pattern, where the distance between the foci is proportional to the relative deflection angle $\Delta\theta_{AOD}$. At this plane, we place a spatial filter, an adjustable mechanical slit (Thorlabs, VA100CP/M), to block the two beams with different optical frequencies. The two remaining beams share the same optical frequencies. Their connecting axis is tilted by 45 ° relative to the optical table. A dove prism is used to rotate the beams so that they are aligned with the optical table. To control the relative optical phase between the two remaining beams, we shift the phase ϕ_{RF1} of only one RF tone. The accumulated phase over the full beam path is identical for both beams. Therefore, the total remaining phase difference $\Delta\phi_0$ follows directly from the phase shift of the AOD drive, ϕ_{RF1}. Finally, because the AOD diffraction efficiency scales with the drive-tone amplitudes A_{RF1} and A_{RF2}, we can independently control the optical power of the two remaining beams.

The AOD drive signals are generated by an arbitrary waveform generator (Spectrum Instrumentation M4i.6631-x8). The waveforms are computed in Python, allowing us to set the drive-tone frequencies ω_{RF1} and ω_{RF2}, phase ϕ_{RF1}, and amplitudes A_{RF1} and A_{RF2}. While the AWG's 400 MHz bandwidth would allow control of trap parameters on timescales much faster than the particle dynamics, the time required to compute the waveforms restricts changes to approximately 0.1 seconds.

Once the trapping beams are generated, a quarter wave plate (QWP) and a HWP optimize the polarization before the beams pass through a Faraday rotator. Finally, the beams are recollimated by a lens with a focal length of $f_2 = 1000$ mm. A HWP rotates the direction of linear polarization of the trapping beams right before the vacuum chamber. The two lenses after the AODs form a telescope in a 4f configuration to expand the beam to a diameter of ~ 8 mm and image the two remaining focal spots to the trapping plane. We use an aspheric lens (LightPath, 355330) with a numerical aperture of $NA = 0.77$, a working distance of $d_w = 1.59$ mm, and a clear aperture of $d_{ap} = 5$ mm to create the traps, which can be seen in Figure 40.

This procedure creates two parallel optical tweezers. The optical power in each trap is set by the AOD drive amplitudes A_{RF1} and A_{RF2}, which in turn determines the particle oscillation frequencies Ω_1 and Ω_2. The optical phase difference in the trapping plane, $\Delta\phi_0$, is controlled by the RF phase ϕ_{RF1}. The mean separation between the traps, d_0, is set by the AOD drive-tone frequency difference $\Delta\omega_{RF} = \omega_{RF1} - \omega_{RF2} \propto \Delta\theta_{RF}$. Once the trapping beams are generated, the initial

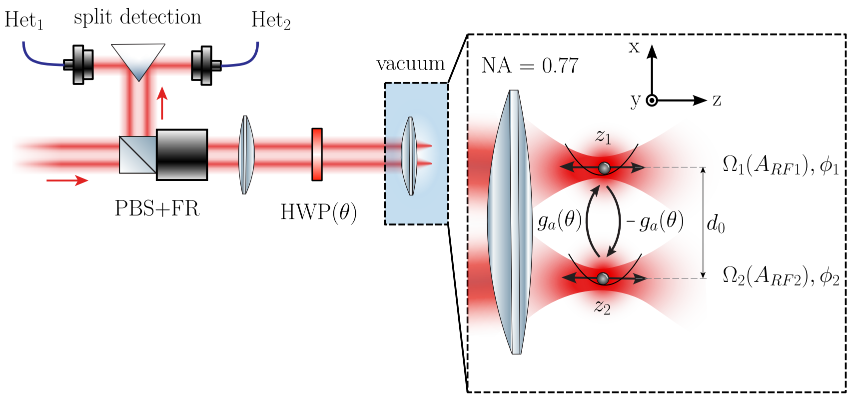

Figure 40: Parallel optical tweezers. Trapping beams created by the AODs pass through a polarizing beam splitter (PBS) and a Faraday rotator (FR), then are recollimated by a lens. A half-wave plate (HWP) sets the angle θ of the linear polarization before a high-NA aspheric lens (NA = 0.77) focuses the beams to form two optical traps. Backscattered light is redirected by the PBS to a split detection. The particle oscillation frequencies Ω_1 and Ω_2, mean interparticle distance d_0, and in-plane optical phase difference $\Delta\phi = \phi_2 - \phi_1$ are controlled via the AOD drive parameters A_{RF1}, A_{RF2}, $\Delta\omega_{RF}$, and ϕ_{RF1}. The coupling rate g_a is tuned by the polarization angle θ.

tweezer alignment is performed as described in Section 4.1.1. Particle loading is done using a nebulizer, as detailed in Section 4.1.4. Additional care is required when aligning parallel optical tweezers to ensure stable trapping and reproducible alignment. Procedures for trap optimization and calibration are presented in Section 7.1.4.

7.1.2 *Individual Particle Detection*

In this experiment, we are only interested in the motion along the trapping beam propagation direction. We use a tweezer backward detection as described in Section 3.3.4, which is most sensitive to the z motion. There is a residual coupling of the x and y motion due to imperfect alignment, which we use for diagnostics of the system. The backscattered light of both particles is collected by the trapping lens. The backscattering passes the second telescope lens before it is split from the main laser line by a Faraday rotator. The trapping lens and the telescope lens reimage the particles in the trapping plane with a magnification of ~ 320. A camera image of four trapped particles (taken with the mechanical slit removed) can be seen in Figure 41. In that imaging plane, we use a knife-edge right-angle prism mirror to separate the light of the two individual particles. Each particle signal is recollimated and coupled into a single-mode fiber. The single-mode fiber is used for mode cleaning, rejecting background light reflected off optical elements, and suppressing crosstalk between the two detection channels. To optimize the coupling of the dipolar emission of the particles into the single-mode fiber, we calculated a magnification

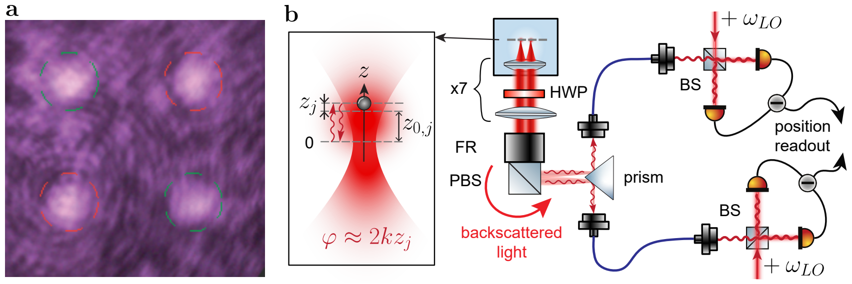

Figure 41: a Camera picture of the reimaged backscattering of four trapped particles. **b** Balanced heterodyne detection of the z motion of individual particles.

of the whole imaging, from particle to fiber core, of ~ 7. Each signal is then overlapped with a local oscillator on a 50/50 fiber beam splitter (Thorlabs, TN1064R5A2A). The light for the local oscillators is split off the main laser line and frequency-shifted by an AOM (Gooch & Housego 3110-197) to set the heterodyne frequency to $\omega_{het}/2\pi = 1.1$ MHz. The local oscillator polarization is matched to the signal polarization at the output of the fiber beam splitters. The beams are finally detected by balanced photodetectors (Thorlabs, PDB425C-AC) to implement a balanced heterodyne detection for each particle. The data acquisition (Pico Technology, PicoScope 5444D) is done with a sampling interval of 96 ns and further position reconstruction is done in post-processing. We calibrate the cross-coupling of the detection by trapping one particle while both traps are on and measuring the position with both channels. We then move the same particle to the other trap and perform another measurement. The cross-coupling in detection is suppressed by ~ 40 dB.

7.1.3 *Position Reconstruction*

The balanced heterodyne detection measures an intensity dependent on the phase difference between signal and local oscillator light

$$I_{het}(t) = |E_{LO}E_{sig}| \cos(\omega_{het}t + \varphi_{het}(t)), \tag{178}$$

where E_{LO} and E_{sig} are the electric field strengths of the local oscillator and the signal, and $\varphi_{het}(t)$ is the phase difference between the signal and the local oscillator beam in a frame rotating with the heterodyne frequency ω_{het}. The heterodyne phase itself depends on the particle position

$$\varphi_{het}(t) \propto \varphi(z(t)) + \varphi(y(t)) + \varphi(x(t)) + \varphi_n(t), \tag{179}$$

where we can separate the contribution of each center of mass motion. All additional changes in the relative phase are given by φ_n, which includes drifts of the relative optical path length and vibrations of the optical elements. We retrieve the optical phase via the Hilbert transform of the heterodyne time trace $\mathcal{H}(I_{het}(t))$. Calculating the argument of the Hilbert transform yields the wrapped phase of the heterodyne time trace $\arg(\mathcal{H}(I_{het}(t)) = \omega_{het}t + \varphi_{het}(t) \mod 2\pi$. The advantage of using heterodyne detection is that the total optical phase $\omega_{het}t + \varphi_{het}(t)$ is a strictly increasing function even though $\varphi_{het}(t)$ is oscillating. This allows straightforward phase unwrapping, and we can finally subtract the linear increase of the heterodyne frequency to obtain the heterodyne phase

$$\varphi_{het}(t) = \mathrm{unwr}\{\arg\left(\mathcal{H}\left[I_{het}(t)\right]\right)\} - \omega_{het}t. \tag{180}$$

All operations are implemented in Python using the NumPy and SciPy packages. The mean mechanical frequencies in this work are $(\Omega_z, \Omega_y, \Omega_x)/2\pi \approx (25, 94, 105)$ kHz. We apply a filter with a bandwidth of $(5, 50)$ kHz to isolate the z contribution to the phase $\varphi(z(t))$. The z position is finally reconstructed using [121]

$$\varphi(z(t)) = 2kz - \arctan\left((z + z_0)/z_R\right), \tag{181}$$

where the second term is a modification due to the Gouy phase of the trapping beam, with the offset of the mean trapping position from the focal plane z_0 and the Rayleigh length $z_R = w_x w_y \pi/\lambda$. We estimate the tweezer waist in the x (y) direction to be $w_x = 0.678$ µm ($w_y = 0.775$ µm) from the trapping frequencies, giving $z_R = 1.55$ µm and the mean displacement $z_0 = 0.8$ µm from the particle radius. The Gouy phase only contributes a modification of $\sim 3\%$ to the total displacement. Hence, it can be safely neglected when reconstructing the particle motion.

7.1.4 *Trap Optimization*

Trapping in parallel optical tweezers with tunable parameters comes with additional challenges. Strong focusing of the trapping beams is subject to imaging errors that distort the optical potential. For small displacements of the particle and a static input beam, even a badly imaged trapping beam can be locally approximated as a harmonic potential and provides a good platform for experiments. However, for parallel optical tweezers with equal optical frequencies, the light of the two traps can interfere. Small contributions from trapping beam 1 can significantly change the optical trap at position 2. With dynamic trap parameters, adjustments in position or phase of each trapping beam can influence the trapping position and oscillation frequency significantly. Hence, we need to take great care to align the beams with minimal crosstalk between them. First, we make sure that the alignment is symmetrical with respect to the trapping lens. For calibration, we trap a single particle, move it from the leftmost position to the rightmost position, and measure its oscillation frequency. The

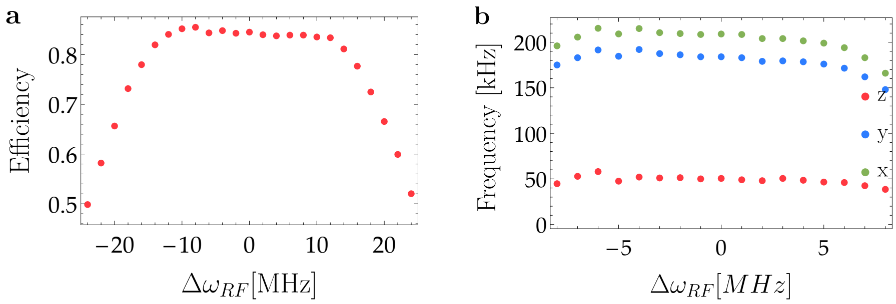

Figure 42: a AOD diffraction efficiency versus AOD drive frequency difference $\Delta\omega_{RF}$. Efficiency is measured after the second AOD, while driving both AOD's with two tones symmetrically spaced up and down around 73 MHz. **b** Particle frequency versus particle position.

trap is created by a single RF drive on each AOD, which is swept symmetrically around the central frequency of 73 MHz. The center of mass oscillation frequencies are affected by diffraction efficiencies of the AODs, which depend on the drive frequency and the clipping losses of the trapping beam at the aperture of the trapping lens. We measure the AOD efficiency independently by comparing the optical input power of the first AOD to the output power of the second. A plot of trap frequencies and diffraction efficiency during a position sweep can be seen in Figure 42. As a second calibration step, we trap a single particle at the desired position and turn the second (empty) trap on. We sweep the optical phase of the second trapping beam, which changes the interference pattern at the trapping position. We monitor the trapping frequencies which change by $\sim 5\%$.

7.1.5 *Distance Calibration*

The mean particle separation is set experimentally by the difference in the AOD drive frequencies $d_0 = C_0 \Delta\omega_{RF}$. The conversion factor C_0 is influenced by many unknown factors, such as the magnification of the telescope and the effective NA of the trapping lens. We can calibrate it by performing an interferometric measurement, using the light radiated by the particles, whose wavelength provides a known etalon. We set the polarization of the trapping light such that the particles scatter maximally toward each other and place a camera in the far field on their connecting axis. The emission of both particles interferes in the plane of detection, where we measure the intensity $I(d_0)$. We sweep the AOD frequency difference between 4 and 12 MHz and record the interference pattern shown in Figure 43. The whole scan has a varying envelope, which is fully repeatable over many measurement runs. We attribute it to changes in the AOD diffraction efficiency. Finally, we fit the interference pattern with a $\cos^2$ function and obtain a conversion factor of $C_0 = (2.3845 \pm 0.0005)\ \mu m/MHz$. All measure-

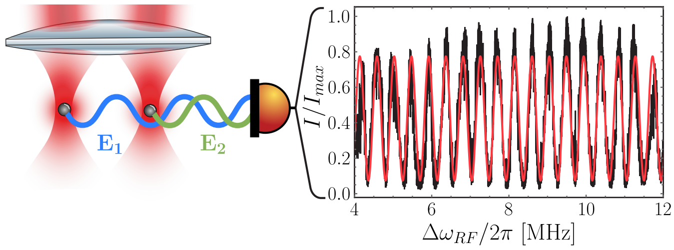

Figure 43: Interferometric measurement to calibrate the mean particle distance. The particle emission interferes in the far field. We sweep the AOD drive frequency difference $\Delta\omega_{RF}$ and record the intensity (black). A fit to the interference pattern (red) yields the conversion factor C_0.

ments in the results section were performed at $\Delta\omega_{RF} = 7.72$ MHz, which leads to a mean particle distance of $d_0 = (18.408 \pm 0.005)$ µm.

7.1.6 *Optical Interaction Calibration*

We can tune the coupling rates of the light-induced dipole-dipole interaction via three experimentally accessible parameters. The relative strength of the anti-reciprocal coupling rate g_a and the reciprocal coupling rate g_r can be tuned by the mean particle distance d_0 and the optical phase difference $\Delta\phi_0$, as seen in Equations (166) and (167), while their overall strength is given by the polarization angle of the trapping light θ, as seen in Equation (168). To find parameters experimentally where g_a is maximized while g_r is negligible, we scan both d_0 and $\Delta\phi_0$ with a polarization angle of $\theta = 0°$ to maximize the overall interaction strength. For a general combination of $g_a \neq 0$ and $g_r \neq 0$, the total interaction strength $g_r \pm g_a$ is not symmetric between particle 1 and particle 2. The peak amplitude of particle 2's motion in the power spectral density of particle 1 is $\propto (g_r + g_a)^2$, whereas, in the other direction, it is $\propto (g_r - g_a)^2$. We monitor the spectrum to find a set of parameters for which the interaction-induced peaks have equal amplitudes, which is possible for either $g_r = 0$ or $g_a = 0$. Finally, we confirm that there is no normal mode splitting for equal particle frequencies but normal mode attraction and conclude that $g_a \neq 0$. The parameters deduced this way are $\Delta\phi_0 = (0.5 \pm 0.08)\pi$, with an error based on the step size of the scan, and $d_0 = (18.408 \pm 0.005)$ µm calculated from the AOD drive frequencies. The reciprocal coupling rate $g_r \propto \cos(kd_0)\cos(\Delta\phi_0) = 0.00 \pm 0.08$ is effectively zero for the chosen conditions.
To calibrate the anti-reciprocal coupling rate, we scan the detuning between the intrinsic mechanical frequencies $\Delta\Omega = \Omega_2 - \Omega_1$. This is done by reducing the power in one AOD drive tone while simultaneously increasing the power in the other. We scan the mechanical frequencies symmetrically around a mean frequency of $\Omega_0 = (\Omega_1 + \Omega_2)/2 \approx 2\pi \cdot 27.5$ kHz. We take a spectrum for each detuning

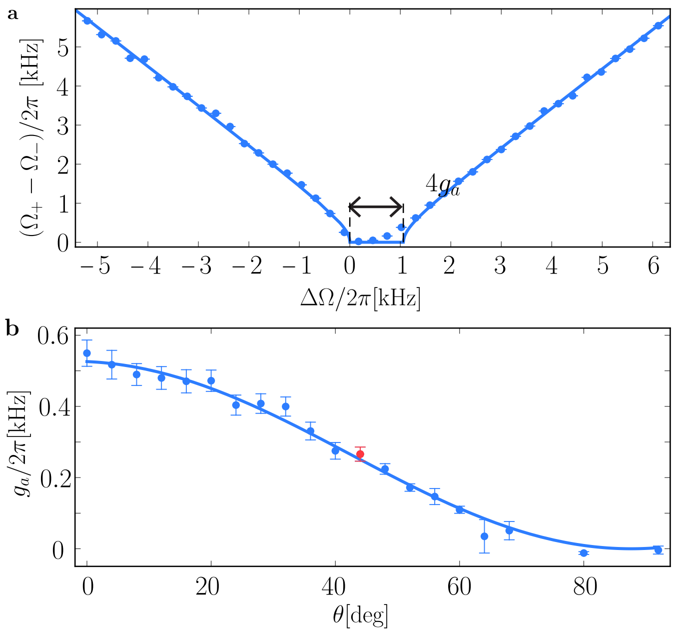

Figure 44: a Normal mode frequency difference versus intrinsic mechanical detuning. Points are obtained from fits to the mechanical spectra, with error bars denoting the standard error of each fit. The line is a fit of the linear model used to extract the coupling rate g_a. **b** Coupling rate versus trapping beam polarization angle. Points are obtained from fits to the normal mode difference, with error bars indicating the standard error of the fit. The red point corresponds to the fit shown in panel a.

and fit the peaks in the spectra of the individual particle motion. After obtaining the normal mode frequencies from the fit, we plot their difference, $\Omega_+ - \Omega_- = \mathrm{Re}(\sqrt{\Delta\Omega^2 - 4g_a\Delta\Omega})$. The normal mode frequencies are degenerate in a region of $\Delta\Omega = (0, 4g_a)$ as per Equation (169). We fit the normal mode frequencies for each polarization angle θ to extract the coupling rate. The coupling rates follow a $\cos^2\theta$ curve as expected and are plotted in Figure 44 together with an example fit of the normal mode frequencies at a polarization angle of $\theta = 42°$. For higher coupling rates, we observe a nonzero difference of the normal mode frequencies in the $\mathcal{PT}$-symmetry broken region. We attribute the discrepancy to small differences in particle mass and thermal fluctuations, which are not included in the linearized theory. Furthermore, we expect small changes in the trap geometries when rotating the polarization, which affects the intrinsic particle detuning $\Delta\Omega$ slightly. We use the fit to the normal mode frequency difference to characterize the zero crossing, and obtain a correction for each polarization angle.

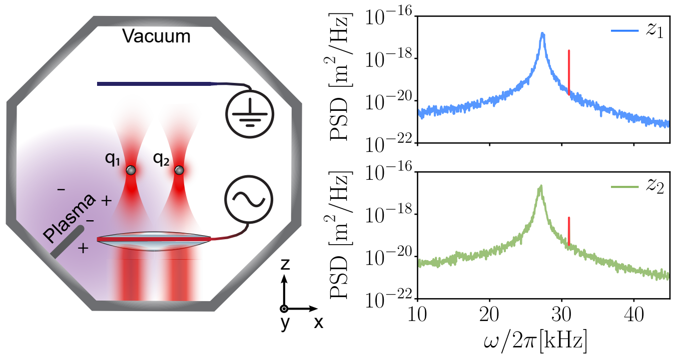

Figure 45: A plasma, ignited at a high-voltage pin inside the vacuum chamber, is used to probabilistically discharge the nanoparticles. We drive the particle motion via electrodes attached to the holder of the trapping lens and recollimation lens. The motional spectrum of particles with estimated charges of $q_1 = (2.5 \pm 0.7)e$ (blue) and a particle with $q_2 = (1.5 \pm 0.5)e$ (yellow) with the remaining response to the electric drive (red) are shown on the right side.

7.1.7 *Charge Calibration*

To measure the effects of the light-induced dipole-dipole interaction, we need to exclude other mechanisms that couple the particle motion. Loading via nebulizer can leave more than 100 elementary charges attached to the nanoparticle surface. Prior studies have shown that electrostatic forces can dominate for nanoparticles in parallel optical tweezers [107]. To discharge both particles until the Coulomb interaction becomes negligible, we ignite a plasma on a high-voltage pin. Free-floating ions or electrons created at the pin attach to the particles probabilistically, leaving their total charge fluctuating. To estimate the number of charges on the particles, we drive their motion electrically. We attach a wire to the metallic holder of the trapping lens and apply an AC voltage with a function generator. The holder of the collimation lens is grounded and acts as the second electrode, forming a capacitor around the particles. We choose a sinusoidal electric drive with a frequency of $\Omega_{ed}/2\pi = 31$ kHz, which is close to the particle oscillation frequency but off-resonance. When the particles are charged, the electric drive manifests as a sharp peak in the spectrum of the motion with an amplitude that is proportional to the number of charges on the particle. We monitor the spectrum in real time while the plasma is on, and turn it off once we see no or minimal response to the electric drive on both particles. Once the plasma is turned off, we observe no change in the number of charges. After discharging the particles, we calibrate the number of charges in a similar manner to the procedure described in [107]. Assuming a point charge in a plate capacitor, the number of charges $N_{1,2}$ is given by

$$N_{1,2} = \frac{\sqrt{2}mD_e}{eV_{AC}} \left|\Omega_{1,2}^2 - \Omega_{ed}^2\right| \sqrt{\langle z_{d1,2}^2 \rangle}, \tag{182}$$

where m is the particle mass, $D_e = (5 \pm 1)$ mm is the distance between the electrodes, $V_{AC} = 10$ V is the drive amplitude, $\Omega_{1,2}$ is the oscillation frequency of particles 1 and 2, and $\langle z^2_{d1,2} \rangle$ is the time-averaged displacement of particles 1 and 2 due to the electric drive.

The motional spectrum of particle 1 (blue) and particle 2 (green) can be seen in Figure 45. The peak due to the electric drive is highlighted in red. We estimate the number of charges to be $N_1 = 2.5 \pm 0.7$ and $N_2 = 1.5 \pm 0.5$ after the discharging process. The remaining Coulomb coupling rate is given by

$$g_c = \frac{N_1 N_2 e^2}{8\pi\varepsilon_0 m \Omega' d_0^3} = (-0.077 \pm 0.030) \text{ Hz}, \tag{183}$$

where e is the elementary charge, ε_0 is the vacuum permittivity, and $\Omega' = \sqrt{\Omega^2 - N_1 N_2 e^2/(4\pi\varepsilon_0 m d_0^3)}$. This coupling rate is small compared to the intrinsic damping rate of the mechanical motion, and the anti-reciprocal coupling rate dominates for polarization angles in the range of $(0°, 80°)$. We can therefore safely neglect the Coulomb interaction for the description of the non-Hermitian dynamics observed here.

7.1.8 *Particle Size*

The models used in this part of the thesis assume two identical spherical particles. We use particles purchased from microParticles GmbH with a radius of $r = 105 \pm 2$ nm and a density of $\rho = 1850$ kg/m^3 as specified by the manufacturer. Even within the specifications, the particle mass can vary significantly. To calibrate the relative size of the particles, we can compare their damping rates. The damping rate of particle i is given by Equation (82)

$$\gamma_i = \frac{16}{\pi} \frac{p}{v_{gas} r_i \rho}. \tag{184}$$

When assuming equal mass density ρ, we can determine the relative radii simply by computing the ratio of the damping rates

$$\frac{\gamma_1}{\gamma_2} = \frac{r_2}{r_1}. \tag{185}$$

To obtain an accurate estimate of the relative radii, we measure the uncoupled motion of each particle at various pressures. We compute the power spectral densities and fit them with the line shape of a driven damped harmonic oscillator to estimate the damping rates. Signatures of rotation are completely absent from all spectra, which allows us to assume perfectly spherical particles. We compute the ratio of the damping rates for each pressure and receive the average size ratio of $r_2/r_1 = 1.01 \pm 0.01$. Figure 46 shows examples of spectra, along with the fits and the resulting damping rate ratios.

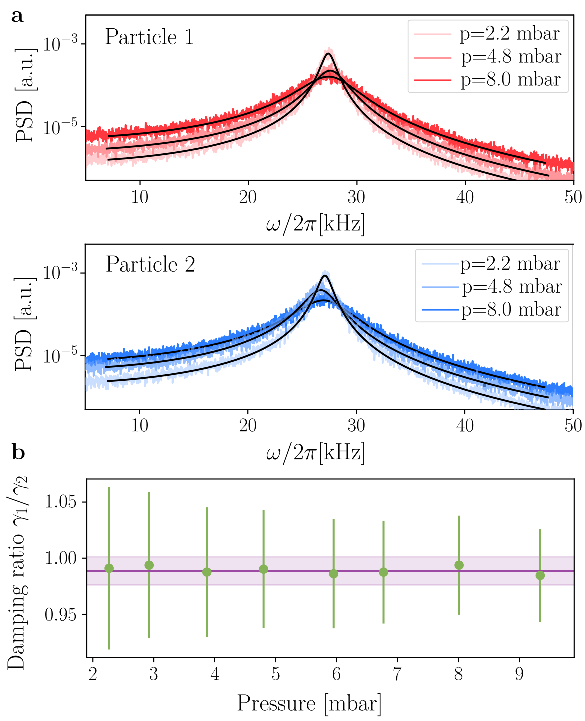

Figure 46: Estimation of relative particle size. **a** We fit the spectra for each particle at various pressures to extract the damping rates $\gamma_{1,2}$. **b** The resulting ratios are plotted in green. The error bars represent the standard error of the fits. The purple region indicates the weighted average $r_2/r_1 = 1.01 \pm 0.01$.

Name	Symbol	Value	Reference
Particle diameter	d	210 nm	7.1.8
Particle density	ρ	1850 kg / m^3	7.1.8
Mean motional frequency	Ω_0	$2\pi \cdot 27.5$ kHz	7.1.6
Mechanical damping rate	γ	$2\pi \cdot 0.46$ kHz	7.2
Mean particle distance	d_0	18.408 µm	7.1.5
Reciprocal coupling rate	g_r	0 kHz	7.1.6
Coulomb interaction rate	g_C	-0.077 Hz	7.1.7
Anti-reciprocal interaction rate	g_a	$2\pi \cdot (0 - 0.55)$ kHz	7.1.6

Table 2: List of parameters used for the results presented here. More information can be found in the referenced sections.

7.2 NON-HERMITIAN DYNAMICS OF OPTICALLY COUPLED NANOPARTICLES

We experimentally investigate the anti-reciprocal light-induced dipole-dipole interaction between two levitated nanoparticles. We choose parameters in our fully tunable system such that the reciprocal $g_r = 0$ and Coulomb $g_C = 0$ coupling rates are negligible. A summary of the used parameters can be seen in Table 2, and their calibration is discussed in previous sections. We choose an operating pressure giving a mechanical damping rate of $\gamma/2\pi = (0.46 \pm 0.02)$ kHz, which we obtain from fits to the mechanical spectra with no interaction $g_a = 0$. We keep the pressure constant over all measurements presented in this section. To explore the joint dynamics systematically, we perform a 2D parameter scan over the intrinsic mechanical detuning $\Delta\Omega$ and the coupling rate g_a. For each measurement, we record a heterodyne time trace of the motion of each particle.

7.2.1 *Linear Dynamics*

The joint particle motion is well described by the linear theory presented in Section 6.1 for all detunings at low coupling rates, i.e., when the gas damping is larger than the coupling-induced amplification. Detuning scans for coupling rates of $g_a/2\pi = 0.012 \pm 0.004$ kHz and $g_a/2\pi = 0.15 \pm 0.02$ kHz are presented in Figure 47. For each detuning, we compute the power spectral density of the individual particle motion. In the far detuned or weakly coupled case, the spectra have one dominant peak, which we fit to extract the normal mode frequencies $\Omega_\pm$ and damping rates $\gamma_\pm$. The scan for the vanishing coupling rate (panel **a**) shows the normal mode frequencies cross at an intrinsic detuning of $\Delta\Omega/2\pi = 0$ kHz, while the damping rates are degenerate and constant over the full scan. At the higher coupling rate (panel

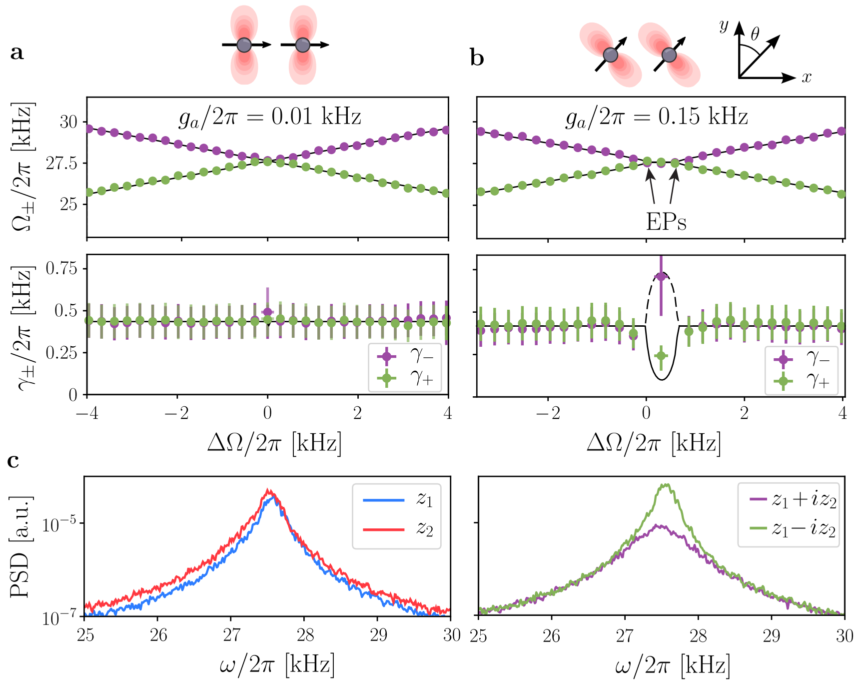

Figure 47: Particle motion in the linear regime. Points show measured normal mode frequencies and damping rates extracted from fits to motional spectra. Error bars represent the standard error of the fit. **a** The normal mode frequencies cross and the damping rates are degenerate for no interaction. **b** The damping rates split and the normal mode frequencies are degenerate in between the exceptional points (EPs) for higher interaction strength. **c** The spectra of the individual particles are almost identical. The reconstructed normal modes reveal one amplified mode and one damped mode.

b), two exceptional points emerge, with a region of degenerate normal mode frequencies in between. At the center of the degeneracy, the spectra of the individual particle motion $z_{1,2}$ are nearly identical, since each particle has an equal contributions from both normal modes for these parameters. However, we can reconstruct the normal modes as $z_\pm = z_1 \mp iz_2$. A fit of the normal mode spectra reveals an amplified mode z_+ with a decreased damping rate and a damped mode z_- with an increased damping rate. The normal mode frequencies and damping rates obtained from linear theory are plotted as a black line in panels **a** and **b** and fit the measurements well.

To get more insight into the correlations and statistics of the particle motion, we take a closer look at their time traces. In Figure 48, we compare three time traces in different regimes. The top row of the figure corresponds to uncoupled oscillators with $g_a/\gamma = -0.01 \pm 0.03$ and $\Delta\Omega/\gamma = 1.18 \pm 0.05$. The time traces and the histograms of the positions show thermal distributions, which are represented by Gaussian distributions. To assess their correlation, we reconstruct the oscillation phase of the particles $\bar{\psi}_{1,2}$ via the Hilbert transform

$$\bar{\psi}_j(z_j(t)) = \mathrm{unwr}\left\{\arg\left(\mathcal{H}[z_j(t)]\right)\right\}. \tag{186}$$

The instantaneous phase delay is given by $\bar{\psi} = \bar{\psi}_2 - \bar{\psi}_1$. The normalized histogram of all phase delays modulo 2π is mostly flat. Some residual correlations are introduced through thermal fluctuations, manifesting as slightly higher values at the center of the shown region. Lastly, we plot the joint $z_1 - z_2$ phase space to analyze the joint motion, which shows an uncorrelated 2D Gaussian distribution, as expected for two uncorrelated thermally driven harmonic oscillators.

The second row of Figure 48 shows a time trace with a slightly increased coupling rate of $g_a/\gamma = 0.32 \pm 0.05$ and a detuning of $\Delta\Omega/\gamma = 1.19 \pm 0.05$. The motion of the particles in this regime is still well described by linear theory. The histograms of the positions are still Gaussian, even though the amplitude of motion is slightly increased. The histogram of the phase delay, however, shows a distinct peak around the most probable phase $\bar{\psi}_{max}$, which is introduced by the anti-reciprocal coupling. One particle follows the other with a phase delay depending on the detuning, which is a consequence of broken $\mathcal{PT}$-symmetry. The joint phase space distribution now shows a 2D Gaussian distribution squashed under an angle depending on $\bar{\psi}$.

When increasing the coupling rate even more, the interaction-induced amplification eventually overcomes the intrinsic mechanical damping. The linear theory would predict infinitely amplified motion. In reality, the next higher-order nonlinearity becomes relevant, stabilizing the system again. The last row in Figure 48 shows dynamics for a coupling rate of $g_a/\gamma = 1.04 \pm 0.08$ and a detuning of $\Delta\Omega/\gamma = 1.37 \pm 0.06$. We see signatures of nonlinear motion in the time trace, which shows a greatly increased amplitude, and the motional statistics are repre-

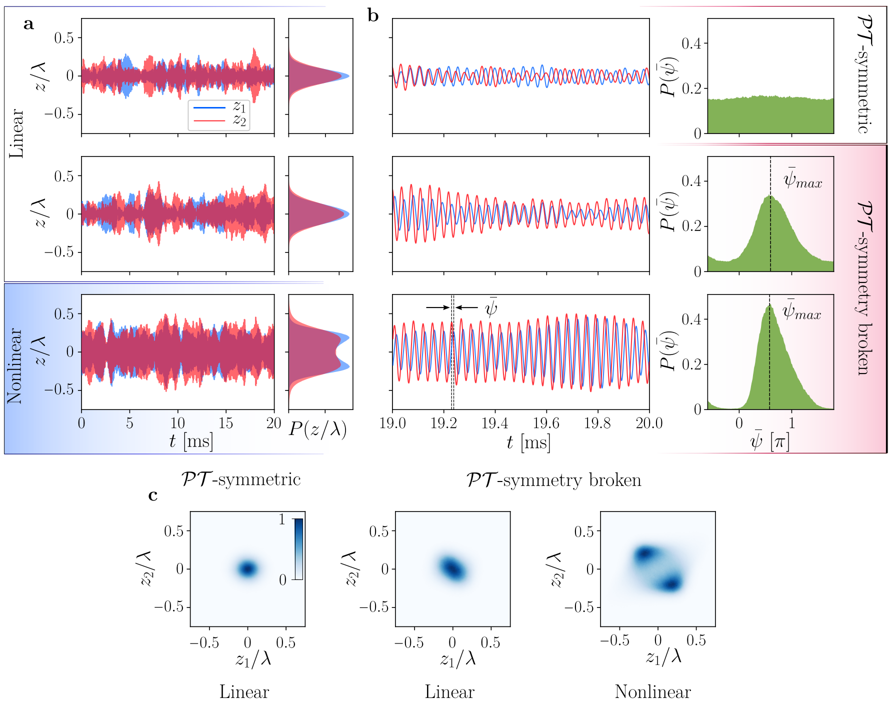

Figure 48: Dynamics from linear to nonlinear motion. **a** shows a larger section of the particle motion and the histogram of all positions. **b** shows a zoomed in section of the particle time trace and the histograms of phase delays $\bar{\psi}$. **c** shows the joint phase space of the particle positions. The first row shows linear dynamics in the $\mathcal{PT}$-symmetric phase. The second row shows linear motion in the $\mathcal{PT}$-symmetry broken phase. The last row shows nonlinear motion in the $\mathcal{PT}$-symmetry broken phase.

sented by a displaced Gaussian distribution. When plotting the distribution of phase delay, we see a highly preferred value $\bar{\psi}_{max}$, which can be resolved in the zoom-in of the time trace. The joint phase space no longer shows a Gaussian distribution, but rather a circular trajectory, which represents a limit cycle.

7.2.2 *Nonlinear Dynamics*

The linearized model predicts the damping rates of the normal modes to be $\gamma_\pm = -2\mathrm{Im}\left[-i\gamma \pm \Lambda\right]$ with $\Lambda = \sqrt{\Delta\Omega^2 - 4g_a\Delta\Omega}$. Once γ_+ changes sign at the threshold $g_a^{thr} = (\gamma^2 + \Delta\Omega^2)/(4\Delta\Omega)$, the linear model breaks down as it would predict an amplified mode a_+, leading to an infinite oscillation amplitude. Instead of the linear model, we can use an analytical model that includes the full nonlinear dynamics but no thermal fluctuations. The nonlinearity of the system stems from the light-induced dipole-dipole interaction itself, which stabilizes the motion again. The trap nonlinearity is negligible in comparison [105]. The model yields two coupled differential equations for the joint motional amplitude $A = 2k\sqrt{\hbar/m\Omega_0}\sqrt{|a_2|^2 + |a_1|^2}$ and the phase delay $\psi = \mathrm{Arg}\left[a_2^* a_1\right]$ as

$$\dot{A} = -\frac{\gamma}{2}A + g_a A \sin(\psi) f\left(A \sin\frac{\psi}{2}\right), \tag{187}$$

$$\dot{\psi} = \Delta\Omega - 4g_a \sin^2\left(\frac{\psi}{2}\right) f\left(A \sin\frac{\psi}{2}\right), \tag{188}$$

where $f(x) = J_1(x)/x$ contains the first-order Bessel function of the first kind J_1. The model is only valid in the $\mathcal{PT}$-symmetry broken phase and has two solutions. The first solution has a trivial joint amplitude and a stable phase delay

$$A = 0, \tag{189}$$

$$\psi = 2\arcsin\left(\sqrt{\frac{\Delta\Omega}{4g_a}}\right). \tag{190}$$

The second solution emerges at the threshold coupling rate g_a^{thr}, where the first solution becomes unstable. The change in the number of solutions defines a Hopf bifurcation, which is discussed later in more detail. This solution yields a collective amplitude A and a stable phase delay ψ satisfying

$$f\left(\frac{A\Delta\Omega}{\sqrt{\gamma^2 + \Delta\Omega^2}}\right) = \frac{\gamma^2 + \Delta\Omega^2}{4g_a\Delta\Omega} \tag{191}$$

$$\psi = 2\arctan\left(\frac{\Delta\Omega}{\gamma}\right). \tag{192}$$

The second solution is truly nonlinear and defines particle motion along a stable limit cycle. To compare the joint motional amplitude

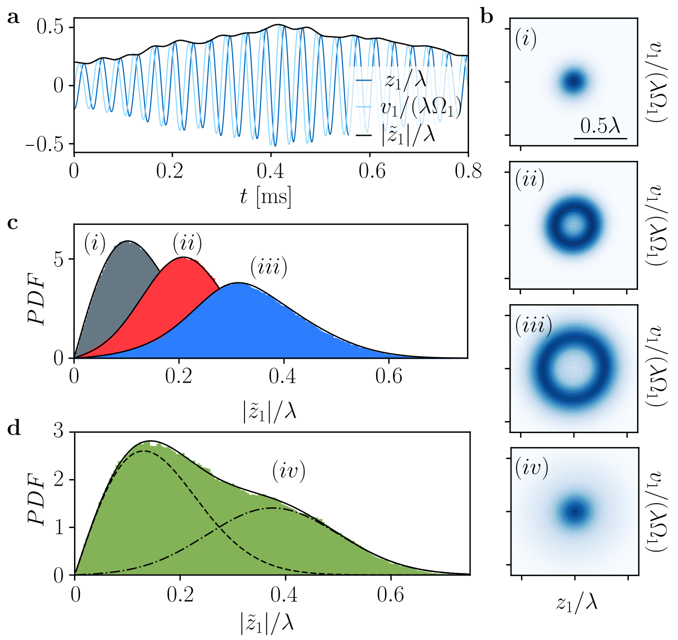

Figure 49: **a** Oscillation amplitudes $|\tilde{z}_j|$ are obtained from the Hilbert transform of the particle time traces. **b** Position-velocity distributions for parameters $(\Delta\Omega/2\pi, g_a/2\pi)$ (i): $(4.78, 0.00)$ kHz, (ii): $(0.40, 0.28)$ kHz, (iii): $(0.35, 0.49)$ kHz, (iv): $(-0.22, 0.49)$ kHz. (i) shows thermal motion, and (ii) and (iii) show limit cycle motion with increasing amplitude $\bar{A}_j$. (iv) shows motion that is sometimes in a thermal state and sometimes in a limit cycle. **c** Fits of the histograms of the oscillation amplitudes corresponding to the motion shown in b. **d** A bimodal distribution is needed for the distribution of the motion shown in (iv).

obtained from theory to experimental values, we extract the motional displacement amplitude $\bar{A}_{1,2}$ from the motion of particle 1 and particle 2.

In the regime below the threshold coupling rate, the particle motion is well described as thermal harmonic oscillators, which have a vanishing displacement amplitude $\bar{A}_{1,2} = 0$. The positions $z_{1,2}$ assume Gaussian distributions centered around zero with a width $\sigma_{1,2}$ given by the thermal occupation. We can compute the oscillation amplitudes using the Hilbert transform

$$|\tilde{z}_{1,2}(t)| = |\mathcal{H}\left[z_{1,2}(t)\right]| . \tag{193}$$

The histogram of the amplitudes $|\tilde{z}_{1,2}(t)|$ is described by a Rayleigh distribution, given by

$$P_{Ray}(|\tilde{z}_j|, \sigma) = \frac{|\tilde{z}_j|^2}{\sigma^2} \exp\left(-\frac{|\tilde{z}_j|^2}{2\sigma^2}\right) . \tag{194}$$

Once the particle motion enters the non-linear regime, a nonzero displacement amplitude $\bar{A}_{1,2} > 0$ emerges, and the particle motion can be described by a displaced thermal state. The distributions of the particle positions are now non-Gaussian, but are still centered around zero. However, the histograms of the motional amplitudes are now given by a Rice distribution, defined as

$$P_{Rice}(|\tilde{z}_j|, \sigma_j, \bar{A}_j) = \frac{|\tilde{z}_j|}{\sigma_j^2} e^{\frac{|\tilde{z}_j|^2 + \bar{A}_j^2}{2\sigma_j^2}} I_0\left(\frac{|\tilde{z}_j|\,\bar{A}_j}{\sigma_j^2}\right), \tag{195}$$

where I_0 is the modified Bessel function of the first kind. The Rice distribution describes the magnitude of a non-central Gaussian random variable. In the limit of $\bar{A}_j \ll \sigma_j$, the Rayleigh distribution is recovered. For every time trace, we independently compute and fit the histograms of the oscillation amplitudes $|\tilde{z}_j|$ for each particle. The fits yield the displacement amplitudes $\bar{A}_{1,2}$, from which we calculate the joint displacement amplitude $\bar{A} = 2k\sqrt{\hbar/(m\Omega_0)}\sqrt{\bar{A}_1^2 + \bar{A}_2^2}$. Figure 49 shows examples of fits for Rayleigh distributions, Rice distributions, and the corresponding phase space plots of the particle motion. For parameters close to the transitions between linear and nonlinear motion, as shown in Figure 49d, we observe slightly modified distributions. We attribute this behavior to fluctuations in the mechanical frequencies caused by thermal noise. As a result, we see the particles moving along limit cycles with $\bar{A}_j > 0$ for some times while they move like thermal oscillators with $\bar{A}_j = 0$ otherwise. We can fit these distributions well with a weighted sum of two Rice distributions

$$P_j(|\tilde{z}_j|) = cP_{Rice}(|\tilde{z}_j|, \sigma_{j,1}, \bar{A}_{j,1}) + (1-c)P_{Rice}(|\tilde{z}_j|, \sigma_{j,2}, \bar{A}_{j,2}) \tag{196}$$

with a weight parameter $0 \leqslant c \leqslant 1$. In these cases, we use the displacement amplitudes of the Rice distribution associated with the higher weight for further evaluation.

We can now compare the experimentally obtained displacement amplitudes with the theoretically predicted ones. To do so, we look at a detuning scan at a coupling rate of $g_a/\gamma = 0.58 \pm 0.05$, shown in Figure 50. Panel **a** of the figure shows a spectrogram of the combined particle motion. For each mechanical detuning $\Delta\Omega$, we compute the power spectral density for both particles, and the color map shows the amplitude of their sum. We see a region of degenerate eigenfrequencies for $0 < \Delta\Omega/\gamma \lesssim 2.3$, where the motional amplitudes are increased and $\mathcal{PT}$-symmetry is broken. The fit to the normal mode frequencies is plotted as a black line.

In Figure 50**b** we show the experimentally extracted joint displacement amplitudes $\bar{A}$ versus the detuning $\Delta\Omega/\gamma$. Within the $\mathcal{PT}$- symmetry broken phase, nonzero displacement amplitudes emerge. The experimentally obtained values are shown as points, while the theory is plotted as a black line. There is good agreement, even though the theory underestimates the displacement amplitudes slightly. We attribute the discrepancy to the lack of thermal fluctuations in the model.

Lastly, in Figure 50**c**, we compute the histograms of the mechanical

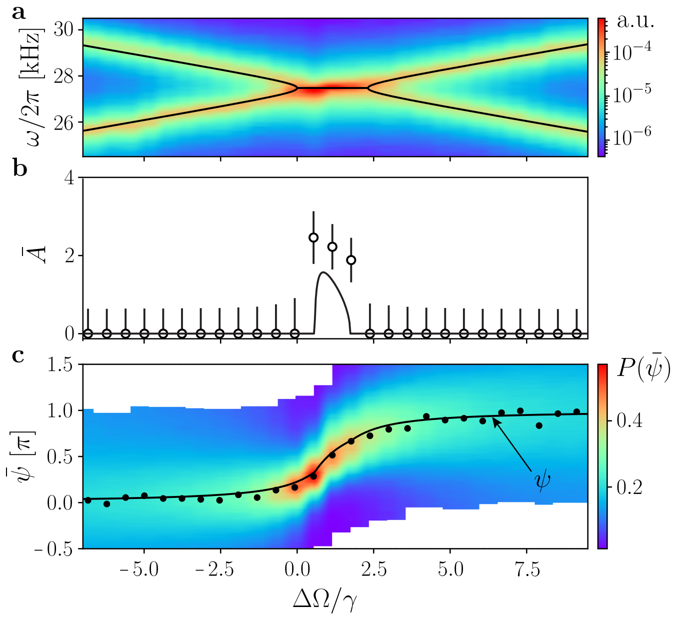

Figure 50: a Spectrogram of the particle motion (color map). The black line represents a fit to the normal mode frequencies, yielding a coupling rate of $g_a/\gamma = 0.58 \pm 0.05$. An amplitude increase can be seen in the region of degenerate eigenfrequencies $0 < \Delta\Omega/\gamma \lesssim 2.3$. **b** The joint displacement amplitude $\bar{A}$ is nonzero in between the exceptional points. Points represent measured values, while the line is the theoretical prediction. **c** Probability density of measured phase delay $\bar{\psi}$ (color map). Points indicate the maximum value of each distribution. The line is a theory curve combining the linear theory with thermal fluctuations in the linear regime and the analytical model in the non-linear regime.

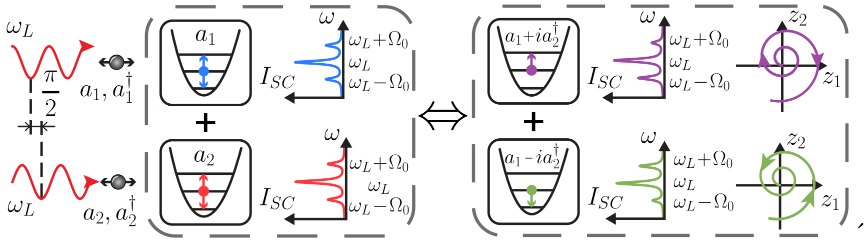

Figure 51: The particle motion leads to scattering of the tweezer mode into the Stokes and the anti-Stokes sidebands. In the eigenmodes, the sidebands interfere, leading to a suppressed anti-Stokes sideband for one mode (purple) and a suppressed Stokes sideband for the other (green).

phase delays $\bar{\psi} \mod 2\pi$ for every detuning and plot them around the most likely phase delay $\bar{\psi}_{max}$. The probability to find a phase delay is given by the color map. The most likely phase delays are indicated by black points in the plot. At large detunings, we see almost uniform distributions. A highly preferred phase delay emerges in the $\mathcal{PT}$-symmetry broken phase induced by the interaction. Outside that region, small correlations are introduced by thermal fluctuations. The black line shows a theory curve that combines the linear theory below the threshold coupling rate and the analytical model above the threshold.

7.2.3 *Mechanical Lasing Transition*

The sudden emergence of a second stable solution ($\bar{A} > 0$) with the change of a parameter (g_a) defines a Hopf bifurcation. Here, the transition can be understood as a mechanical lasing transition. In comparison to a laser, the highly populated tweezer mode represents the upper level of the gain medium, while the Stokes sideband represents the lower level. Scattering from the tweezer mode into the Stokes sideband creates a phonon in the mechanical degrees of freedom of the particles. To suppress the reverse process of scattering into the anti-Stokes sideband, optical cavities are typically used [139]. Here, the interference of the sidebands created by the particles suppresses scattering into the anti-Stokes sideband for the a_+ eigenmode and scattering into the Stokes sideband for the a_- eigenmode. This leads to an overall amplified mode (suppressed anti-Stokes scattering) and a damped mode (suppressed Stokes scattering). The lasing threshold is reached when the total amplification of the interaction surpasses the total damping of the system. A schematic explanation of the interference of the sidebands and the amplification process can be seen in Figure 51.

To characterize this transition, we perform detuning scans for different coupling rates. For every parameter combination, we extract the joint displacement amplitude $\bar{A}$ and plot it in shades of blue in Figure

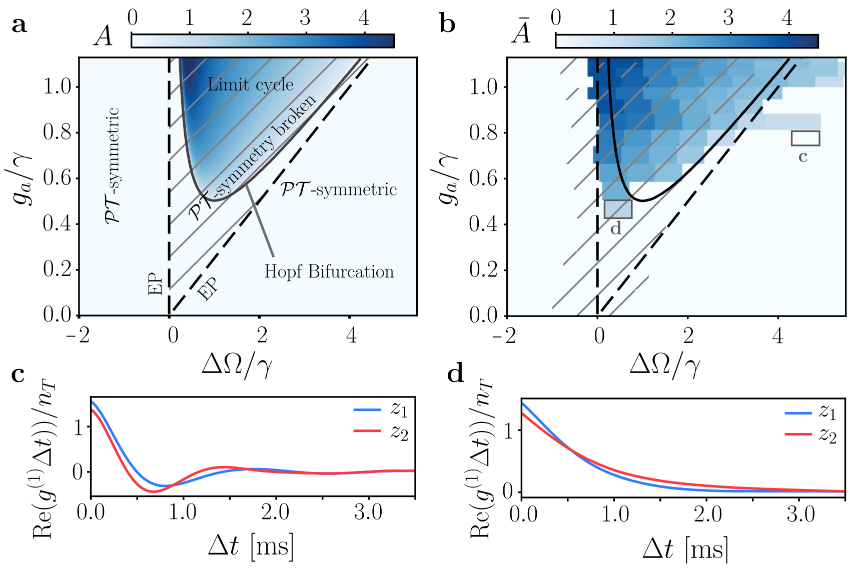

Figure 52: a Displacement amplitude A calculated from the analytical model is plotted in blue (color map). **b** Experimentally obtained displacement amplitudes $\bar{A}$ are plotted in blue (color map). Each pixel in the plot represents one measurement, with its center given by the detuning and its bottom edge by the coupling rate. The dashed and solid black lines are theory curves. In both panels a and b, we distinguish three regions. The hatched region between the exceptional points (EP) represents the $\mathcal{PT}$-symmetry broken phase, while the non-hatched region is the $\mathcal{PT}$-symmetric phase. The blue area represents the mechanical lasing phase. **c** and **d** The autocorrelation functions show oscillatory behavior in the $\mathcal{PT}$-symmetric phase and bi-exponentially decaying behavior in the $\mathcal{PT}$-symmetry broken phase. The measurement shown is indicated in panel b by gray outlines.

52. To compare theory to experiment, we plot the displacement amplitudes obtained from the analytical model (175) side by side with the experimentally obtained values. For the data presented in 52b, each pixel represents one measurement. We position the pixels such that their center is at the detuning of the measurement and their lower edge is given by the coupling rate. To compensate for drifts of the mechanical frequencies during the measurement, we shift the detunings by the offset obtained from the coupling rate calibration presented in Section 7.1.6. We distinguish three regions in the plots: the hatched region between the exceptional points (dashed lines) represents the $\mathcal{PT}$-symmetry broken phase, while the non-hatched region represents the $\mathcal{PT}$-symmetric phase. The limit cycle phase is above the Hopf bifurcation marked by the black theory line in both plots.

To determine whether the particles are in the $\mathcal{PT}$-symmetric or in the $\mathcal{PT}$-symmetry broken phase, we study the behavior of the autocorrelation function as presented in Section 6.1. For each particle, we compute the autocorrelation functions of the complex amplitudes $g^{(1)}_{jj}/n_T = \langle a^*_j(t)a_j(t+\Delta t)/n_T\rangle$ using Python's 'scipy.signal.correlate' function. The correlation function changes from an oscillatory func-

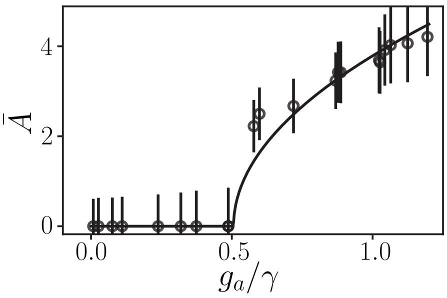

Figure 53: Joint oscillation amplitude $\bar{A}$ versus coupling rate g_a/γ at detuning $\Delta\Omega/\gamma \approx 0.9$. Points show amplitudes obtained from fits, and error bars indicate the standard error of the fit. The solid line is a theoretical curve fitted to the joint amplitudes. The onset of limit cycle motion occurs at the threshold coupling $g_a/\gamma = 0.5$ and follows a square-root dependence on g_a/γ, indicative of a Hopf bifurcation.

tion to a bi-exponentially decaying function as it transitions from $\mathcal{PT}$-symmetric to $\mathcal{PT}$-symmetry broken. Examples can be seen in Figure 52c and 52d. To distinguish the two cases in evaluation, we detect if there are zero crossings present in the traces. Regardless of the detuning $\Delta\Omega$ and coupling rate g_a, the correlation function decays exponentially with a rate given by the gas damping γ. This always leads to zero crossings due to noise at sufficiently long times. We therefore limit the evaluation to short times of $t < 3.5$ ms.

To characterize the lasing transition, we plot the displacement amplitudes $\bar{A}$ for a detuning of $\Delta\Omega/\gamma \approx 0.9$ in Figure 53. We choose this detuning for its low threshold coupling rate. The displacement amplitude stays zero until a threshold coupling rate of $g_a/\gamma \approx 0.5$ is reached, where the Hopf bifurcation is predicted by the analytical model. A nonzero amplitude emerges as the coupling rate increases and follows a square-root dependence on the coupling rate, as predicted by bifurcation theory. This transition can be interpreted as a second-order (non-Hermitian) phase transition[48]. Note, however, that our system does not exhibit an apparent thermodynamic limit.

7.3 DISCUSSION AND OUTLOOK

In this experiment, we demonstrated non-Hermitian dynamics of two anti-reciprocally coupled, levitated nanoparticles in the linear and nonlinear regime. We showed the versatility of the light-induced dipole-dipole interaction in parallel optical tweezers by in situ tuning the coupling rate and mechanical detuning. We utilized individual particle detection to show signatures of $\mathcal{PT}$-symmetry breaking and to reconstruct the normal modes of the system. Within the $\mathcal{PT}$-symmetry broken phase, we observed a Hopf-bifurcation, at which the joint particle motion transitioned into limit cycle motion.

This work shows steady-state effects of two particles and opens the door to studying the dynamical properties of non-Hermitian chains of coupled particles, such as those that arise when an exceptional point is circled [39, 96, 135]. The possibility of creating large particle arrays with controllable interactions has great potential for studying non-Hermitian phase transitions [48] and non-equilibrium physics [75, 78, 136]. Operation near an exceptional point might provide an advantage for sensing applications [73, 82, 84, 101, 117, 134]. Cooling of the particle motion to the ground state [34] or cooling of limit cycle fluctuations [5] might enable the study of collective quantum effects, such as non-Hermitian quantum physics [80] and quantum optical binding [110]. The addition of an optical cavity can enable true long-range interactions and entanglement of particle motion.

Part III

APPENDIX

A

DERIVATION OF THE PHOTON RECOIL HEATING

This derivation is adapted from the single atom case [61] and a version of it can be found in [62].

We start with a particle in a harmonic trap, driven by the scattering of photons from the Gaussian beam trapping the particle. The number of photons fluctuates, which gives rise to the damping and heating effects. The model for each direction is

$$m\ddot{x}_i + m\Omega_i^2 x_i = F(t). \tag{197}$$

The force originates form scattering events with individual photons and is modeled by

$$\mathbf{F}(t) = \sum_j \delta(t - t_j)\hbar(\mathbf{k} - \mathbf{k}_{sc}^j). \tag{198}$$

The j-th photon has initial momentum $\hbar k$, final momentum $\hbar k_{sc}^j$ and scatters at a time t_j. The net momentum transfer is $\mathbf{k} - \mathbf{k_{sc}}$ with

$$\begin{aligned} \mathbf{k} &= (0, 0, k)^T & (199) \\ \mathbf{k}_{sc} &= k_{sc}(\sin\theta\cos\varphi, \sin\theta\sin\varphi, \cos\theta)^T. & (200) \end{aligned}$$

The fluctuating force is split into its mean and its fluctuations $\mathbf{F}(t) = \langle \mathbf{F} \rangle + \mathbf{F}'(t)$. The time averaged force can be calculated via the difference of initial and final photon momentum

$$\langle \mathbf{F} \rangle = \hbar \langle r_{sc}(\mathbf{k} - \mathbf{k_{sc}}) \rangle, \tag{201}$$

with the average photon scattering rate

$$r_{sc} = \frac{I_0}{\hbar\omega}\sigma(\omega), \tag{202}$$

where the intensity at the focus is given by I_0. The scattering cross section is given by

$$\sigma(\omega) = \frac{k^4 \alpha_0^2}{6\pi\varepsilon_0^2}. \tag{203}$$

The frequency of the scattered photons is Doppler shifted due to the motion of the particle. Because of the small particle velocity $v \ll c$ it can be approximated by

$$\omega = \sqrt{1 - \beta^2}\omega_0 + \beta\omega_0\cos\theta \approx \omega_0 + \mathbf{k}_{sc} \cdot \mathbf{v} \tag{204}$$

with $\beta = v/c$ and $\sqrt{1 - \beta} \approx 1$ and $\beta\omega_0\cos\theta = \mathbf{k}_{sc} \cdot \mathbf{v}$. Here ω_0 denotes the frequency of the incoming photons. This gives the approximated scattering cross section of

$$\sigma(\omega) \approx \frac{\alpha_0^2}{6\pi\varepsilon_0^2 c^4}(\omega_0 + \mathbf{k}_{sc} \cdot \mathbf{v})^4 \approx \frac{\alpha_0^2 \omega_0^4}{6\pi\varepsilon_0^2 c^4}(1 + \frac{4\mathbf{k}_{sc} \cdot \mathbf{v}}{\omega_0}). \tag{205}$$

Inserting this approximation into equation 201 gives

$$\begin{aligned}\langle \mathbf{F}\rangle &\approx \frac{I_0\alpha_0^2\omega_0^3}{6\pi\varepsilon_0^2c^4}\left\langle\left(1+\frac{\mathbf{k}_{sc}\cdot\mathbf{v}}{\omega_0}\right)(\mathbf{k}-\mathbf{k}_{sc})\right\rangle & (206)\\ &= \hbar r_0\int_0^{2\pi}\int_0^{\pi}P_s(\theta)\left(1+\frac{4\mathbf{k}_{sc}\cdot\mathbf{v}}{\omega_0}\right)(\mathbf{k}-\mathbf{k}_{sc})\sin\theta\, d\theta\, d\varphi & (207)\end{aligned}$$

The average is evaluated with the dipole emission pattern $P_s(\theta)$ [121]

$$P_s(\theta) = \frac{3}{8\pi}\left(1-\sin^2\theta\cos^2\varphi\right) \tag{208}$$

and the constant is

$$r_0 = \frac{P_0}{3\pi^2 w_0}\frac{\alpha_0^2\omega_0^3}{\hbar\varepsilon_0^2c^4} \tag{209}$$

where I have used

$$I_0 = \frac{2P_0}{w_0^2\pi} \tag{210}$$

with the total power of the Gaussian beam P_0 and the beam waist w_0. The integration can be carried out and leads to the components of the averaged force

$$\begin{aligned}\langle F_x\rangle &= -\frac{9}{16}\hbar k_{sc}\pi - 1\cdot\frac{4}{5}\frac{\hbar k_{sc}^2 r_0}{\omega_0}v_x & (211)\\ \langle F_y\rangle &= -\frac{9}{16}\hbar k_{sc}\pi - 2\cdot\frac{4}{5}\frac{\hbar k_{sc}^2 r_0}{\omega_0}v_y & (212)\\ \langle F_z\rangle &= -\frac{9}{16}\hbar k_{sc}\pi - 2\cdot\frac{4}{5}\frac{\hbar k_{sc}^2 r_0}{\omega_0}v_z & (213)\end{aligned}$$

The averaged force has a component proportional to the velocity of the particle which can be interpreted as a friction term. Inserting this result into the equation of motion from Equation (197) leads to

$$m\ddot{x}_i + m\gamma^i_{recoil}\dot{X}_i + m\Omega_i^2 X_i = -\frac{9\pi}{16}r_0\hbar k_{sc} + F_i'(t). \tag{214}$$

One can apply the coordinate transformation $X_i = x_i + (9\pi/16)r_0\hbar k_{sc}$ to get equations for a damped harmonic oscillator driven by the fluctuations of the force

$$m\ddot{X} + m\gamma^i_{recoil}\dot{X} + m\Omega_i^2 X = F_i'(t) \tag{215}$$

with the damping rate

$$\gamma^i_{recoil} = \xi_i\frac{4}{5}\frac{\hbar k^2 r_0}{m\omega_0} \tag{216}$$

and $\xi_i = (1,2,2)$ for $i = (x,y,z)$. In the last step it was assumed that the change in photon energy is small $k_{sc}\approx k$ and $\omega\approx\omega_0$.

B
CAVITY DETECTION CALCULATIONS

I show here how to calculate the spectrum of the detected current from a balanced heterodyne detection setup detecting the ouput mode of a coherent scattering cavity setup.
The two photo detectors produce the currents

Thank you Klemens <3

$$
\begin{aligned}
\hat{i}_1(t) = &\left(\eta \frac{1}{\sqrt{2}} a^\dagger_{in}(t) - \eta\sqrt{\kappa}\frac{1}{\sqrt{2}} a^\dagger(t) + \eta\frac{1}{\sqrt{2}} a^\dagger_{LO}(t) + \sqrt{1-\eta^2} a^\dagger_{\nu 1}(t)\right) \cdot \\
&\left(\eta \frac{1}{\sqrt{2}} a_{in}(t) - \eta\sqrt{\kappa}\frac{1}{\sqrt{2}} a(t) + \eta\frac{1}{\sqrt{2}} a_{LO}(t) + \sqrt{1-\eta^2} a_{\nu 1}(t)\right) \\
\hat{i}_2(t) = &\left(\eta \frac{1}{\sqrt{2}} a^\dagger_{in}(t) - \eta\sqrt{\kappa}\frac{1}{\sqrt{2}} a^\dagger(t) - \eta\frac{1}{\sqrt{2}} a^\dagger_{LO}(t) - \sqrt{1-\eta^2} a^\dagger_{\nu 1}(t)\right) \cdot \\
&\left(\eta \frac{1}{\sqrt{2}} a_{in}(t) - \eta\sqrt{\kappa}\frac{1}{\sqrt{2}} a(t) - \eta\frac{1}{\sqrt{2}} a_{LO}(t) - \sqrt{1-\eta^2} a_{\nu 1}(t)\right)
\end{aligned}
$$

The difference current is given by

$$
\begin{aligned}
&\Delta\hat{i}(t) = \hat{i}_1(t) - \hat{i}_2(t) \\
&= \eta^2 a^\dagger_{in}(t) a_{LO}(t) + \frac{1}{\sqrt{2}}\eta\sqrt{1-\eta^2} a^\dagger_{in}(t)\left(a_{\nu 1}(t) + a_{\nu 2}(t)\right) \\
&-\eta^2\sqrt{\kappa} a^\dagger(t) a_{LO}(t) \\
&-\frac{1}{\sqrt{2}}\sqrt{\kappa}\eta\sqrt{1-\eta^2} a^\dagger(t)\left(a_{\nu 1}(t) + a_{\nu 2}(t)\right) + \eta^2 a^\dagger_{LO}(t) a_{in}(t) \\
&-\eta^2\sqrt{\kappa} a^\dagger_{LO}(t) a(t) + \frac{1}{\sqrt{2}}\eta\sqrt{1-\eta^2} a^\dagger_{LO}(t)\left(a_{\nu 1}(t) - a_{\nu 2}(t)\right) \\
&+\frac{1}{\sqrt{2}}\eta\sqrt{1-\eta^2}\left(a^\dagger_{\nu 1}(t) + a^\dagger_{\nu 2}(t)\right) a_{in}(t) \\
&-\frac{1}{\sqrt{2}}\sqrt{\kappa}\eta\sqrt{1-\eta^2}\left(a^\dagger_{\nu 1}(t) + a^\dagger_{\nu 2}(t)\right) a(t) \\
&+\frac{1}{\sqrt{2}}\eta\sqrt{1-\eta^2}\left(a^\dagger_{\nu 1}(t) + a^\dagger_{\nu 2}(t)\right) a_{LO}(t) \\
&+(1-\eta^2) a^\dagger_{\nu 1}(t) a_{\nu 1}(t) + (1-\eta^2) a^\dagger_{\nu 2}(t) a_{\nu 2}(t)
\end{aligned}
$$

I assume that the local oscillator is a large amplitude coherent state $a_{LO}(t) = |\alpha_{LO}| e^{-i\omega_{LO} t} + a_{LO}$ allowing me to neglect all terms not proportional to $|\alpha_{LO}|$. The signal fields will be moved to the frame rotating with its optical frequency $a(t)e^{-i\omega_{sig} t}$. Further the noise terms can be redefined to $a_\nu(t) = 1/\sqrt{2}(a_{\nu 1}(t) - a_{\nu 2}(t))$. That leaves the current as

$$
\begin{aligned}
\Delta\hat{i}(t) \simeq\ & |\alpha_{LO}|\left(\eta^2 a_{in}(t) e^{-i\omega_{het} t} - \eta^2\sqrt{\kappa} a(t) e^{-i\omega_{het} t}\right. \\
&\left. +\eta\sqrt{1-\eta^2} a_\nu(t) e^{-i\omega_{het} t} + \text{H.c.}\right)
\end{aligned} \tag{217}
$$

where $\omega_{het} = \omega_{sig} - \omega_{LO}$. To compute the spectrum the Fourier transformed current is needed

$$\begin{aligned}
\Delta\hat{i}(\omega) &= \int dt e^{i\omega t}\Delta\hat{i}(t) \\
&= |\alpha_{LO}|\Big(\eta^2 a_{in}^\dagger(-\omega-\omega_{het}) - \eta^2\sqrt{\kappa}a^\dagger(-\omega-\omega_{het}) \\
&\quad +\eta\sqrt{1-\eta^2}a_v^\dagger(-\omega-\omega_{het}) + \eta^2 a_{in}(\omega-\omega_{het}) \\
&\quad -\eta^2\sqrt{\kappa}a(\omega-\omega_{het}) + \eta\sqrt{1-\eta^2}a_v(\omega-\omega_{het})\Big) \qquad (218)
\end{aligned}$$

Using the equation 138 and 141 from the matrix formalism, I can rewrite this into

$$\begin{aligned}
&\Delta\hat{i}(\omega) = \\
&|\alpha_{LO}|\,(\eta^2 I^2_{2\alpha}\mathbf{N}_\alpha(\omega+\omega_{het}) - \eta^2\sqrt{\kappa}\overline{\chi}_{2\alpha}(\omega+\omega_{het})\mathbf{N}_\alpha(\omega+\omega_{het}) \\
&\quad \eta^2 I^1_{1\alpha}\mathbf{N}_\alpha(\omega-\omega_{het}) - \eta^2\sqrt{\kappa}\overline{\chi}_{1\alpha}(\omega-\omega_{het})\mathbf{N}_\alpha(\omega-\omega_{het}) \\
&\quad +\eta\sqrt{1-\eta^2}a_v^\dagger(-\omega-\omega_{het}) + \eta\sqrt{1-\eta^2}a_v(\omega-\omega_{het})\Big) \qquad (219)
\end{aligned}$$

where the sum is to be taken over matching indices. The two transfer matrices are defined such that $I^1_{1\alpha}\mathbf{N}_\alpha(\omega) = a_{in}(\omega)$ and $I^2_{2\alpha}\mathbf{N}_\alpha(\omega) = a_{in}^\dagger(-\omega)$ with

$$I^1 = \begin{pmatrix} \frac{1}{\sqrt{\kappa}} & 0 & 0 & 0 \\ 0 & 0 & 0 & 0 \\ 0 & 0 & 0 & 0 \\ 0 & 0 & 0 & 0 \end{pmatrix} \qquad (220)$$

$$I^2 = \begin{pmatrix} 0 & 0 & 0 & 0 \\ 0 & \frac{1}{\sqrt{\kappa}} & 0 & 0 \\ 0 & 0 & 0 & 0 \\ 0 & 0 & 0 & 0 \end{pmatrix}. \qquad (221)$$

The current is further simplified to

$$\Delta\hat{i}(\omega) = |\alpha_{LO}|\Big(\overline{\overline{\chi}}^2_{2\alpha}(\omega+\omega_{het})\mathbf{N}_\alpha(\omega+\omega_{het}) \qquad (222)$$

$$+\overline{\overline{\chi}}^1_{1\alpha}(\omega-\omega_{het})\mathbf{N}_\alpha(\omega-\omega_{het}) \qquad (223)$$

$$+\eta\sqrt{1-\eta^2}a_v^\dagger(-\omega-\omega_{het}) + \eta\sqrt{1-\eta^2}a_v(\omega-\omega_{het})\Big) \qquad (224)$$

with

$$\overline{\overline{\chi}}^1_{ij}(\omega) = \eta^2 I^1_{ij} - \eta^2\sqrt{\kappa}\overline{\chi}_{ij}(\omega) \qquad (225)$$

$$\overline{\overline{\chi}}^2_{ij}(\omega) = \eta^2 I^2_{ij} - \eta^2\sqrt{\kappa}\overline{\chi}_{ij}(\omega). \qquad (226)$$

Finally the Spectrum is defined as $S_{\Delta\hat{\imath}\Delta\hat{\imath}}(\omega) = \int\langle\Delta\hat{\imath}(\omega)\Delta\hat{\imath}(\omega')\rangle d\omega'$. Note that the current is a hermitian operator $\Delta\hat{\imath}(t)^\dagger = \Delta\hat{\imath}(t)$.

$$\begin{aligned} S_{\Delta\hat{\imath}\Delta\hat{\imath}}(\omega) = \\ \int d\omega' \Big(& \overline{\overline{X}}^2_{2\alpha}(\omega+\omega_{het})\overline{\overline{X}}^2_{2\beta}(\omega'+\omega_{het})\langle\mathbf{N}_\alpha(\omega+\omega_{het})\mathbf{N}_\beta(\omega'+\omega_{het})\rangle \\ & \overline{\overline{X}}^1_{1\alpha}(\omega-\omega_{het})\overline{\overline{X}}^1_{1\beta}(\omega'-\omega_{het})\langle\mathbf{N}_\alpha(\omega-\omega_{het})\mathbf{N}_\beta(\omega'-\omega_{het})\rangle \\ & \overline{\overline{X}}^2_{2\alpha}(\omega+\omega_{het})\overline{\overline{X}}^1_{1\beta}(\omega'-\omega_{het})\langle\mathbf{N}_\alpha(\omega+\omega_{het})\mathbf{N}_\beta(\omega'-\omega_{het})\rangle \\ & \overline{\overline{X}}^1_{1\alpha}(\omega-\omega_{het})\overline{\overline{X}}^2_{2\beta}(\omega'+\omega_{het})\langle\mathbf{N}_\alpha(\omega-\omega_{het})\mathbf{N}_\beta(\omega'+\omega_{het})\rangle \\ & +\eta^2(1-\eta^2)\langle a_v(\omega-\omega_{het})a_v^\dagger(-\omega'-\omega_{het})\rangle\Big)\,|\alpha_{LO}|^2 \end{aligned} \tag{227}$$

The first two terms are fast rotating and will average out in any real measurement. All the remaining correlators can be calculated with the assumption that the fields are thermal states and all optical fields are in a vacuum state. The basic correlators for thermal states are

$$\langle a_{th}(t)a_{th}(t')\rangle = \langle a^\dagger_{th}(t)a^\dagger_{th}(t')\rangle = 0 \tag{228}$$

$$\langle a_{th}(t)a^\dagger_{th}(t')\rangle = (n_{th}+1)\delta(t-t') \tag{229}$$

$$\langle a^\dagger_{th}(t)a_{th}(t')\rangle = n_{th}\delta(t-t'). \tag{230}$$

and their Fourier transforms are straight forwardly calculated which leads to the matrix of all correlators

$$\begin{aligned} &\langle\mathbf{N}_\alpha(\omega)\mathbf{N}_\beta(\omega')\rangle = \\ &= \begin{pmatrix} 0 & \kappa\langle a_{in}(\omega)a^\dagger_{in}(\omega')\rangle & 0 & 0 \\ 0 & 0 & 0 & 0 \\ 0 & 0 & -\gamma\langle P_{in}(\omega)P_{in}(\omega')\rangle & \gamma\langle P_{in}(\omega)P^\dagger_{in}(\omega')\rangle \\ 0 & 0 & \gamma\langle P^\dagger_{in}(\omega)P_{in}(\omega')\rangle & -\gamma\langle P^\dagger_{in}(\omega)P^\dagger_{in}(\omega')\rangle \end{pmatrix}_{\alpha\beta} \\ &= \begin{pmatrix} 0 & \kappa & 0 & 0 \\ 0 & 0 & 0 & 0 \\ 0 & 0 & -\gamma\left(1+\frac{n}{2}\right) & \gamma\left(1+\frac{n}{2}\right) \\ 0 & 0 & \gamma\left(1+\frac{n}{2}\right) & -\gamma\left(1+\frac{n}{2}\right) \end{pmatrix}_{\alpha\beta} \delta(\omega+\omega') = C_{\alpha\beta}\delta(\omega+\omega') \end{aligned} \tag{231}$$

where n is the occupation of the mechanical motion. The matrix of correlators is used to further simplify equation 227 to

$$\begin{aligned} S_{\Delta\hat{\imath}\Delta\hat{\imath}}(\omega) = \\ |\alpha_{LO}|^2\int d\omega'\Big(&\overline{\overline{X}}^2_{2\alpha}(\omega+\omega_{het})\overline{\overline{X}}^1_{1\beta}(\omega'-\omega_{het})C_{\alpha\beta}\delta(\omega+\omega') \\ &\overline{\overline{X}}^1_{1\alpha}(\omega-\omega_{het})\overline{\overline{X}}^2_{2\beta}(\omega'+\omega_{het})C_{\alpha\beta}\delta(\omega+\omega') \\ &+\eta^2(1-\eta^2)\Big) \\ = |\alpha_{LO}|^2\Big(&\overline{\overline{X}}^2_{2\alpha}(\omega+\omega_{het})C_{\alpha\beta}\overline{\overline{X}}^{1\,T}_{\beta 1}(-\omega-\omega_{het}) \\ &+\overline{\overline{X}}^1_{1\alpha}(\omega-\omega_{het})C_{\alpha\beta}\overline{\overline{X}}^{2\,T}_{\beta 2}(-\omega+\omega_{het})+\eta^2(1-\eta^2)\Big) \end{aligned} \tag{232}$$

which can be easily calculated by Mathematica and is the final expression for the quantum spectrum.

C

CALCULATIONS RELATED TO THE COHERENT SCATTERING HAMILTONIAN

Here, I write out some parts of the calculations for the coherent scattering Hamiltonian explicitly. This calculation starts with Equation (120) of the main text repeated here for reference

$$\left|\hat{\mathbf{E}}(\mathbf{x},t)\right|^2 = \left|\hat{\mathbf{E}}_{tw} + \hat{\mathbf{E}}_{cav}\right|^2 = \left|\hat{\mathbf{E}}_{tw}\right|^2 + \left|\hat{\mathbf{E}}_{cav}\right|^2 + \hat{\mathbf{E}}^*_{tw}\hat{\mathbf{E}}_{cav} + \hat{\mathbf{E}}_{tw}\hat{\mathbf{E}}^*_{cav}. \tag{233}$$

The displacement $x_c \to x_c - x_s$ impacts the spatial part of the fields only. It keeps most of the spatial field distribution approximately unchanged except for the cosine term

$$w_c(x_c) \to w_c(x_c - x_s) \sim w_c(x_c) \tag{234}$$

$$R_c(x_c) \to R_c(x_c - x_s) \sim R_c(x_c) \tag{235}$$

$$\phi_{gc}(x_c) \to \phi_{gc}(x_c - x_s) \sim \phi_{gc}(x_c) \tag{236}$$

$$\cos\left(k_c(x_c - x_s) + \frac{k_c(y_c^2 + z_c^2)}{2R_c(x_c)}\right) \to \tag{237}$$

$$\cos\left(k_c x_c + \frac{k_c(y_c^2 + z_c^2)}{2R_c(x_c)} - \phi\right) \tag{238}$$

where the phase shift $\phi = k_c x_s$ was introduced in the last line.
I will proceed to calculate the terms of Equ. (120): first the tweezer part:

$$|E_{tw}(\mathbf{x},t)|^2 = \frac{1}{4}|E_{tw}(\mathbf{x})e^{-i\omega_{tw}t} + E^*_{tw}e^{i\omega_{tw}t}|^2 \tag{239}$$

$$= \frac{1}{4}\left(E^2_{tw}e^{-i2\omega_{tw}t} + {E^*_{tw}}^2 e^{i2\omega_{tw}t} + 2E_{tw}E^*_{tw}\right) \tag{240}$$

Writing out the first part explicitly

$$E^2_{tw}e^{-2\omega_{tw}t} = \frac{E^2_{0t}w^2_{0t}}{w^2_t(z)}\mathbf{e}^2_t \exp\left(-\frac{2x^2}{w^2_{xt}(z)} - \frac{2y^2}{w^2_{yt}(z)}\right) \tag{241}$$

$$\times \exp\left(-\frac{i2k_t(x^2+y^2)}{2R_t(z)} + i2\phi_{gt}(z) - i2k_t z\right) e^{-i2\omega_{tw}t} \tag{242}$$

This and the similar term ${E^*_{tw}}^2 e^{i2\omega_{tw}t}$ will be neglected when applying a rotating wave approximation. The last term is

$$2E_{tw}E^*_{tw} = \frac{2E^2_{0t}w^2_{0t}}{w^2_t(z)}\mathbf{e}^2_t \exp\left(-\frac{2x^2}{w^2_{xt}(z)} - \frac{2y^2}{w^2_{yt}(z)}\right). \tag{243}$$

The cavity term

$$|E_{cav}(\mathbf{x},t)|^2 = \frac{\hbar\omega_{cav}}{2\varepsilon_0 V_{cav}} \mathbf{e}_c^2 \left| f(\mathbf{x}) e^{-i\omega_{cav}t} a + f^*(\mathbf{x}) e^{i\omega_{cav}t} a^\dagger \right|^2 \tag{244}$$

$$= \frac{\hbar\omega_{cav}}{2\varepsilon_0 V_{cav}} \Big(f(\mathbf{x})^2 e^{-i2\omega_{cav}t} aa + f^*(\mathbf{x})^2 e^{i2\omega_{cav}t} a^\dagger a^\dagger \tag{245}$$

$$+ f(\mathbf{x}) f^*(\mathbf{x}) a a^\dagger + f^*(\mathbf{x}) f(\mathbf{x}) a^\dagger a \Big). \tag{246}$$

Neglecting again the fast rotating terms due to the rotating wave approximation and using the commutator $[a, a^\dagger] = 1$ leads to

$$|E_{cav}|^2 \simeq \frac{\hbar\omega_{cav}}{2\varepsilon_0 V_{cav}} 2 f^*(\mathbf{x}) f(\mathbf{x}) \left(a^\dagger a + \frac{1}{2} \right) \tag{247}$$

with

$$f(\mathbf{x}) f^*(\mathbf{x}) = f^*(\mathbf{x}) f(\mathbf{x}) \tag{248}$$

$$= \frac{w_{0c}^2}{w_c^2(x_c)} \exp\left(-\frac{2(y_c + z_c)}{w_c^2(x_c)} \right) \cos^2\left(k_c x_c + \frac{k_c(y_c^2 + z_c^2)}{2R_c(x_c)} - \phi \right) \tag{249}$$

The interesting cross term is

$$E_{tw}^*(\mathbf{x},t) E_{cav}(\mathbf{x},t) \tag{250}$$

$$= \sqrt{\frac{\hbar\omega_{cav}}{2\varepsilon_0 V_{cav}}} \frac{1}{2} \mathbf{e}_c \cdot \mathbf{e}_t \left(E_{tw}^*(\mathbf{x}) e^{i\omega_{tw}t} + E_{tw}(\mathbf{x}) e^{-i\omega_{tw}t} \right) \tag{251}$$

$$\times \left(f(\mathbf{x}) e^{-i\omega_{cav}t} a + f^*(\mathbf{x}) e^{i\omega_{cav}t} a^\dagger \right) \tag{252}$$

$$= \sqrt{\frac{\hbar\omega_{cav}}{2\varepsilon_0 V_{cav}}} \frac{1}{2} \mathbf{e}_c \cdot \mathbf{e}_t \Big[E_{tw}^*(\mathbf{x}) f(\mathbf{x}) e^{-i(\omega_{cav} - \omega_{tw})t} a \tag{253}$$

$$+ E_{tw}(\mathbf{x}) f^*(\mathbf{x}) e^{i(\omega_{cav} - \omega_{tw})t} a^\dagger \tag{254}$$

$$+ E_{tw}^*(\mathbf{x}) f^*(\mathbf{x}) e^{i(\omega_{cav} + \omega_{tw})t} a^\dagger + E_{tw}(\mathbf{x}) f(\mathbf{x}) e^{-(\omega_{cav} + \omega_{tw})t} a \Big] \tag{255}$$

the last two terms rotating with $(\omega_{cav} + \omega_{tw})$ can be neglected again due to the rotating wave approximation. The spatial parts are given by

$$E_{tw}^*(\mathbf{x}) f(\mathbf{x}) = \frac{E_{0t} w_{0t} w_{0c}}{w_t(z) w_c(x_c)} \exp\left(-\frac{x^2}{w_{xt}^2(z)} - \frac{y^2}{w_{yt}^2(z)} \right)$$
$$\times \exp\left(\frac{ik_t(x^2 + y^2)}{2R_t(z)} - i\phi_{gt}(z) + ikz \right) \exp\left(-\frac{y_c^2 + z_c^2}{w_c^2(x_c)} \right)$$
$$\exp\left(-\phi_{gc}(x_c) \right) \cos\left(k_c x_c + \frac{k_c(y_c^2 + z_c^2)}{2R_c(x_c)} - \phi \right) \tag{256}$$

$$E_{tw}(\mathbf{x}) f^*(\mathbf{x}) = \frac{E_{0t} w_{0t} w_{0c}}{w_t(z) w_c(x_c)} \exp\left(-\frac{x^2}{w_{xt}^2(z)} - \frac{y^2}{w_{yt}^2(z)} \right)$$
$$\times \exp\left(-\frac{ik_t(x^2 + y^2)}{2R_t(z)} + i\phi_{gt}(z) - ikz \right) \exp\left(-\frac{y_c^2 + z_c^2}{w_c^2(x_c)} \right)$$
$$\exp\left(\phi_{gc}(x_c) \right) \cos\left(k_c x_c + \frac{k_c(y_c^2 + z_c^2)}{2R_c(x_c)} - \phi \right) \tag{257}$$

Now two approximations will be made to all of the terms derived above. First as already mentioned the rotating wave approximation allows us the neglect terms $\propto e^{\pm i 2\omega_{cav,tw}t}$, $e^{\pm i(\omega_{cav}+\omega_{tw})t}$. The second approximation will be for small displacements $x, y, z \ll \lambda < w_{x,y}, w_{0c} < x_0, z_0$.

$$|E_{tw}(\mathbf{x},t)|^2 \overset{\text{RWA}}{\simeq} \frac{E_{0t}w_{0t}^2}{w_t^2(z)} \exp\left(-\frac{2x^2}{w_{xt}^2(z)} - \frac{2y^2}{w_{yt}^2(z)}\right) \tag{258}$$

$$\overset{|\mathbf{x}|\ll\lambda}{\simeq} E_{0t}^2 - E_{0t}^2\left(\frac{2x^2}{A_x^2 w_{0t}^2} + \frac{2y^2}{A_y^2 w_{0t}^2} + \frac{z^2}{z_0^2}\right) \tag{259}$$

$$= \frac{1}{2}\sum_{j=x,y,z} m\Omega_j^2 j^2. \tag{260}$$

With the approximations

$$\frac{1}{w_t^2(z)} \simeq \frac{1}{w_{0t}^2} - \frac{z^2}{w_{0t}^2} z_0^2 \tag{261}$$

$$\exp\left(-\frac{2x^2}{w_{xt}^2(z)}\right) \simeq 1 - \frac{2x^2}{A_x^2 w_{0t}^2}. \tag{262}$$

Only terms up to quadratic order were kept. In Equation (260) the constant term was neglected and the frequencies Ω_j were introduced to emphasize the similarity to a harmonic potential

$$\Omega_x^2 = \frac{2\alpha E_{0t}^2}{A_x^2 w_{0t}^2 m} \tag{263}$$

$$\Omega_y^2 = \frac{2\alpha E_{0t}^2}{A_y^2 w_{0t}^2 m} \tag{264}$$

$$\Omega_z^2 = \frac{\alpha E_{0t}^2 \lambda_t^2}{\pi^2 w_{0t}^4 m}. \tag{265}$$

The cavity term approximates to

$$|E_{cav}(\mathbf{x},t)|^2 \overset{\text{RWA}}{\simeq} \frac{\hbar\omega_{cav}}{\varepsilon_0 V_{cav}}\left[f^*(\mathbf{x})f(\mathbf{x})\left(a^\dagger a + \frac{1}{2}\right)\right] \tag{266}$$

$$\overset{|\mathbf{x}|\ll\lambda}{\simeq} \frac{\hbar\omega_{cav}}{2\varepsilon_0 V_{cav}}\big(\cos^2(\phi)k_c x_c + \sin(2\phi)\big)\left(a^\dagger a + \frac{1}{2}\right) \tag{267}$$

where only linear terms were kept. The following approximations were used to obtain this equation

$$\exp\left(-\frac{2y_c^2}{w_c^2(x_c)}\right) \simeq 1 - \frac{2y_c^2}{w_{0c}^2} \tag{268}$$

$$\frac{k_c(y_c^2+z_c^2)}{2R_c(x_c)} = \frac{k_c x_c(y_c^2+z_c^2)}{2(x_c^2+x_0^2)} \ll k_c x_c \tag{269}$$

$$\begin{aligned}\cos^2\left(k_c x_c + \frac{k_c x_c(y_c^2+z_c^2)}{2(x_c^2+x_0^2)} - \phi\right) &\simeq \cos^2\left(k_c x_c - \phi\right) \\ &= \frac{1}{2}\left(1+\cos(2k_c x_c - 2\phi)\right) \\ &\simeq \cos^2(\phi) + k_c x_c \sin(2\phi).\end{aligned} \tag{270}$$

The two cross terms are complex conjugates of each other and I will write only one explicitly here.

$$\begin{aligned}E_{tw}^*(\mathbf{x},t)E_{cav}(\mathbf{x},t) &\overset{\text{RWA}}{\simeq} \sqrt{\frac{\hbar\omega_{cav}}{2\varepsilon_0 V_{cav}}}\frac{1}{2}\mathbf{e}_c\cdot\mathbf{e}_t\Big[E_{tw}^*(\mathbf{x})f(\mathbf{x})e^{-i(\omega_{cav}-\omega_{tw})t}a \\ &\quad + E_{tw}(\mathbf{x})f^*(\mathbf{x})e^{i(\omega_{cav}-\omega_{tw})t}a^\dagger\Big]\end{aligned} \tag{271}$$

$$\begin{aligned}E_{tw}^*(\mathbf{x})f(\mathbf{x}) &\overset{|\mathbf{x}|\ll\lambda}{\simeq} E_{0t}\left(1-\frac{z^2}{2z_0^2}\right)\left(1-\frac{x_c^2}{2x_0^2}\right) \\ &\quad\times\left(1-\frac{x^2}{A_x^2w_{0t}^2}-\frac{y^2}{A_y^2w_{0t}^2}-iz\left(\frac{1}{z_0}-k_t\right)\right. \\ &\quad\left.-\frac{y_c^2}{w_{0c}^2}-\frac{z_c^2}{w_{0c}^2}-i\frac{x_c}{x_0}\right)\left(\cos(\phi)+k_c x_c\sin(\phi)\right)\end{aligned} \tag{272}$$

$$\simeq E_{0t}\left(\cos\phi - i\cos\phi\frac{x_c}{x_0} - i\cos\phi z\left(\frac{1}{z_0}-k_t\right) + k_c x_c\sin\phi\right) \tag{273}$$

where only term to leading order where kept. Inserting Equation (273) into the mixed term results in

$$\begin{aligned}E_{tw}^*(\mathbf{x},t)E_{cav}(\mathbf{x},t) &\simeq \sqrt{\frac{\hbar\omega_{cav}}{2\varepsilon_0 V_{cav}}}E_{0t}\mathbf{e}_t\cdot\mathbf{e}_c\Big[\cos\phi\left(a^\dagger e^{i\Delta t}+ae^{-i\Delta t}\right) \\ &+i\cos\phi\frac{x_c}{x_0}\left(a^\dagger e^{i\Delta t}-ae^{-i\Delta t}\right)+i\cos\phi z\left(\frac{1}{z_0}-k_t\right)\left(a^\dagger e^{i\Delta t}-ae^{-i\Delta t}\right) \\ &+k_c x_c\sin\phi\left(a^\dagger e^{i\Delta t}+ae^{-i\Delta t}\right)\Big]\end{aligned} \tag{274}$$

where $\Delta = \omega_{cav} - \omega_{tw}$.

D RANDOM CAVITY EQUATIONS

Maybe rewrite this at the end if there is time. Noone reads the appendix anyways. I wrote those so they are in here now! Have fun y'all.

Note that this description already has a rotating wave approximation. The bath - system coupling is assumed to be weak and non-energy conserving terms are neglected. See [132] page 28.

We can derive the Heisenberg equations of motion for $c(\omega)$ and a

$$\dot{c}(\omega) = -i\omega c(\omega) + \sqrt{\frac{\kappa(\omega)}{2\pi}}a \tag{275}$$

$$\dot{a} = -\frac{i}{\hbar}[a, H_{sys}] - \int d\omega \sqrt{\frac{\kappa(\omega)}{2\pi}}c(\omega). \tag{276}$$

A solution to Equation (275) is

$$c(\omega) = e^{-i\omega(t-t_0)}c_0(\omega) + \sqrt{\frac{\kappa(\omega)}{2\pi}}\int_{t_0}^{t} e^{-i\omega(t-t')}a(t')dt'. \tag{277}$$

Inserting this and Equation (46) into (276) leads to

$$\dot{a} = -i\omega_{cav}a - \int d\omega \sqrt{\frac{\kappa(\omega)}{2\pi}}\left(e^{-i\omega(t-t')}c_0(\omega)\right. \tag{278}$$

$$\left.+\sqrt{\frac{\kappa(\omega)}{2\pi}}\int_{t_0}^{t} e^{-i\omega(t-t')}a(t')dt'\right), \tag{279}$$

where c_0 is the value of $c(t)$ at $t = t_0$. To further simplify this, we make the first Markov approximation, which assumes that the coupling is frequency independent $\kappa(\omega) = \kappa$, to finally arrive at the Langevin equation

$$\dot{a} = -i\omega_{cav}a - \frac{\kappa}{2}a - \sqrt{\kappa}c_{in}(\omega). \tag{280}$$

Here, an input field has been defined

$$c_{in}(t) = \frac{1}{\sqrt{2\pi}}\int d\omega e^{-i\omega(t-t_0)}c_0(\omega), \tag{281}$$

which satisfies the commutation relation $[c_{in}(t), c^{\dagger}_{in}(t')] = \delta(t-t')$. The previous derivation can be adapted to include outgoing fields by considering $t_1 > t$ in the solution to Equation (275)

$$c(\omega) = e^{-i(t-t_1)}c_1(\omega) - \sqrt{\frac{\kappa(\omega)}{2\pi}}\int_{t}^{t_1} e^{-i\omega(t-t')}a(t')dt'. \tag{282}$$

Following the same steps as above, one arrives at the Langevin equation including the output field

$$\dot{a} = -i\omega_{cav}a + \frac{\kappa}{2}a - \sqrt{\kappa}c_{out}(t), \tag{283}$$

with the definition of the output field as

$$c_{out}(t) = \frac{1}{\sqrt{2\pi}}\int d\omega e^{-i\omega(t-t_1)}c_1(\omega). \tag{284}$$

By integrating Equation (277) and (282)

$$\int c(\omega)d\omega = c_{in}(t) + \frac{\sqrt{\kappa}}{2}a(t) \tag{285}$$

$$\int c(\omega)d\omega = c_{out}(t) - \frac{\sqrt{\kappa}}{2}a(t), \tag{286}$$

one gets an identity relating in and out fields

$$c_{out}(t) - c_{in}(t) = \sqrt{\kappa}a(t). \tag{287}$$

The input and output fields are typically vacuum states for optical frequencies or high amplitude coherent states for a cavity driven by a strong laser field. To explicitly model this, we can apply the displacement operator $D(\alpha_D(t)) = \exp(\alpha_D(t)c^\dagger(\omega_D) - \alpha^*(t)c(\omega_D))$ to the Hamiltonian (47), resulting in the driven Hamiltonian

$$H = H_{sys} + H_B + H_{int}^D \tag{288}$$

$$H_{int}^D = i\hbar\int d\omega\sqrt{\frac{\kappa(\omega)}{2\pi}}\left(c^\dagger(\omega)a - a^\dagger c(\omega)\right) + \ldots$$
$$\ldots i\hbar E_D\left(ae^{i\omega_D t} - a^\dagger e^{-i\omega_D t}\right). \tag{289}$$

The complex coherent amplitude is rewritten as $\alpha_D = |\alpha_D|\exp(-i\omega_D t)$ and the definition $E_D = |\alpha_D|\sqrt{\kappa_{in}/2\pi}$ used, where κ_{in} quantifies the coupling of the cavity mode to the driven mode. One can associate E_D with the power of an incident laser via $E_D = \sqrt{P_{in}\kappa_{in}/\hbar\omega_D}$. Further, we can move to a frame that is rotating with the coherent drive by applying the transformation $H \to H_R = U^\dagger H U - A$, with

$$A = \hbar\omega_D a^\dagger a + \hbar\omega_D\int d\omega c^\dagger(\omega)c(\omega) \tag{290}$$

$$U = e^{-i\omega_D a^\dagger a t}e^{-i\omega_D\int d\omega c^\dagger(\omega)c(\omega)t}. \tag{291}$$

The annihilation operator $a_R = U^\dagger a U = ae^{-i\omega_D t}$ is transformed to have an explicit time dependence in the old frame. In the following, we drop the subscript $_R$ for convenience and the energy shift of the bath modes $\omega \to (\omega - \omega_D)$ has been ignored. The Hamiltonian in the rotating frame is given by

$$\begin{aligned} H &\to U^\dagger H U - A \\ &= \hbar\omega_{cav}\left(a^\dagger a + \frac{1}{2}\right) - \hbar\omega_D a^\dagger a + \hbar\int d\omega(\omega - \omega_D)c^\dagger(\omega)c(\omega) + \\ &\quad i\hbar\int d\omega\sqrt{\frac{\kappa}{2\pi}}\left(c^\dagger(\omega)a - a^\dagger c(\omega)\right) + \\ &\quad i\hbar E_D\left(a - a^\dagger\right). \end{aligned} \tag{292}$$

This finally leads to the Langevin equation

$$\dot{a} = -i\Delta a - \frac{\kappa}{2}a - \sqrt{\kappa}c_{in} - E_D. \tag{293}$$

Note that the external modes $c(\omega)$ may consist of modes that can be measured, like modes that are transmitted through the end mirrors of the cavity, and modes that are inaccessible, like modes that are scattered or absorbed within the cavity. It is therefore sometimes convenient to split those modes and define separate couplings such that $\kappa = \kappa_{in} + \kappa_0$.

The mode supported by the boundary conditions given by the mirrors are Hermite-Gaussian beams. Those are reflected back and forth between the mirrors. The right going contribution is

$$\begin{aligned} E_r(x,y,z) = \frac{E_0 w_0}{w(z)} \exp\left(-\frac{x^2+y^2}{w^2(z)} - \frac{ik(x^2+y^2)}{2R(z)}\right) H_m\left(\frac{\sqrt{2}x}{w(z)}\right) \times \\ H_n\left(\frac{\sqrt{2}y}{w(z)}\right) \exp\left(-i(m+n+1)\arctan\left(\frac{z}{z_0}\right)\right) \exp\left(-ikz\right) \end{aligned} \tag{294}$$

For the left going contribution E_l we flip the sign of the wavenumber $(k \to -k)$. Finally we sum them up to get the electric field (technically we do an infinite sum $E = E_l + rE_r + r^2E_l + ...$) but whateva

$$E(x,y,z) = E_r + E_l \tag{295}$$

$$\begin{aligned} &= \frac{E_0 w_0}{w(z)} \exp\left(-\frac{x^2+y^2}{w^2(z)}\right) H_m\left(\frac{\sqrt{2}x}{w(z)}\right) H_n\left(\frac{\sqrt{2}y}{w(z)}\right) \times \\ &\quad \exp\left(-i(m+n+1)\arctan\left(\frac{z}{z_0}\right)\right) \times \\ &\quad \left[\exp\left(-i\left(kz + \frac{k(x^2+y^2)}{2R(z)}\right)\right) + \exp\left(i\left(kz + \frac{k(x^2+y^2)}{2R(z)}\right)\right)\right] \\ &= \frac{2E_0 w_0}{w(z)} \exp\left(-\frac{x^2+y^2}{w^2(z)}\right) H_m\left(\frac{\sqrt{2}x}{w(z)}\right) H_n\left(\frac{\sqrt{2}y}{w(z)}\right) \times \\ &\quad \exp\left(-i(m+n+1)\arctan\left(\frac{z}{z_0}\right)\right) \cos\left(kz + \frac{k(x^2+y^2)}{2R(z)}\right). \end{aligned} \tag{296}$$

This gives the intensity distribution of

$$I(x,y,z) = |E^2| = \frac{4E_0^2 w_0^2}{w^2(z)} \exp\left(-\frac{2(x^2+y^2)}{w^2(z)}\right) H_m^2\left(\frac{\sqrt{2}x}{w(z)}\right) \times \\ H_n^2\left(\frac{\sqrt{2}y}{w(z)}\right) \cos^2\left(kz + \frac{k(x^2+y^2)}{2R(z)}\right)$$

E
EQUATIONS CONCERNING TIGHT FOCUSING

The force on an arbitrary rigid body exerted by an electromagnetic field can derived from Maxwell's equations and can be written in the form [92]

$$\langle \mathbf{F} \rangle = \int_{\partial V} \langle \mathbb{T}(\mathbf{r}, t) \rangle \cdot \mathbf{n}(\mathbf{r}) da. \tag{297}$$

Here $\langle\ .\ \rangle$ denotes a time average over one cycle of the electromagnetic field, $\mathbb{T}$ is Maxwell's stress tensor in vacuum. The integral is to be taken over a surface ∂V of a volume V containing the body of interest and $\mathbf{n}$ is the unit vector perpendicular to the infinitesimal surface element da. If one considers instead of a general rigid body a dipole with a dipole moment $\mathbf{p}$ the force can be put in a simpler and more intuitive way. This approximation is valid if the arbitrary body considered in Equation (297) is a dielectric sphere with radius a much smaller than the wavelength of the illuminating field $a \ll \lambda$. In this case the illuminating filed $\mathbf{E}$ induces a dipole moment $\mathbf{p}$ in the material which interacts with the field again to generate the force

$$\mathbf{F} = (\mathbf{p} \cdot \nabla)\mathbf{E} + \dot{\mathbf{p}} \times (\nabla \times \mathbf{E}) + \frac{d}{dt}(\mathbf{p} \times \mathbf{B}). \tag{298}$$

It is assumed that the motion of the particle is small compared to the speed of light. In the time average of the force the last term vanished and the first two terms can be rewritten to

$$\langle \mathbf{F} \rangle = \sum_i \langle p_i(t) \nabla E_i(t) \rangle \tag{299}$$

where the sum is taken over the components $i = x, y, z$ of the vectors and $\langle \cdot \rangle$ is the time average. As a next step we consider only monochromatic fields illuminating the particle with frequency ω which can be represented by

$$\mathbf{E}(\mathbf{r}, t) = \mathrm{Re}\left[\underline{\mathbf{E}}(\mathbf{r}) e^{-i\omega t}\right] \tag{300}$$

$$\mathbf{B}(\mathbf{r}, t) = \mathrm{Re}\left[\underline{\mathbf{B}}(\mathbf{r}) e^{-i\omega t}\right] \tag{301}$$

where the underline denotes the complex amplitudes of the fields. Further we assume that the induced dipole moment of the particle is directly proportional to the illuminating field at the particles position $\mathbf{r}_0$ and has the same time dependence

$$\mathbf{p} = \mathrm{Re}\left[\underline{\mathbf{p}} e^{-i\omega t}\right], \qquad \text{with} \tag{302}$$

$$\underline{\mathbf{p}} = \alpha \underline{\mathbf{E}}(\mathbf{r}_0). \tag{303}$$

The polarizability of the particle α is assumed to be frequency independent which is true for the materials and frequency range used in the following experiments but will not hold in general. Under those assumptions the cycle averaged force can be written as

$$\langle \mathbf{F} \rangle = \frac{\alpha'}{2} \sum_i \mathrm{Re}\left[\underline{E}_i^* \nabla \underline{E}_i\right] + \frac{\alpha''}{2} \sum_i \mathrm{Im}\left[\underline{E}_i^* \nabla \underline{E}_i\right]. \tag{304}$$

The effective polarizability is split in its real and imaginary part $\alpha = \alpha' + i\alpha''$. For the induced dipole of a spherical dielectric it is given by

$$\alpha = \alpha_0 \left(1 - i\frac{k^3}{6\pi\varepsilon_0}\alpha_0\right), \quad \text{with} \tag{305}$$

$$\alpha_0 = 3V\varepsilon_0 \frac{\varepsilon_p - \varepsilon_m}{\varepsilon_p + 2\varepsilon_m} \tag{306}$$

where $k = 2\pi/\lambda$, ε_0 is the vacuum permittivity, ε_p is the relative permittivity of the dielectric particle, $\varepsilon_m = 1$ is the relative permittivity of the surrounding medium, which is assumed to be vacuum here and the volume of the particle is given by V. The first term of the force given in 70 arises due to the gradient of the field and can be rewritten as $\langle \mathbf{F}_{grad} \rangle = (\alpha'/4)\nabla(\underline{\mathbf{E}}^* \cdot \underline{\mathbf{E}})$. It is called gradient force and can be associated with a potential. It points to the local maximum of the intensity distribution of the electric field. The second term cannot be associated with a potential but with a momentum transfer from the electromagnetic field to the particle. For fields with uniform helicity it can be rewritten as $\langle \mathbf{F}_{scatt} \rangle = \sigma/c\langle \mathbf{S} \rangle$, where $\sigma = \alpha'' k/\varepsilon_0$ is the absorption cross-section and $\langle \mathbf{S} \rangle$ is the averaged pointing vector. It is called scattering force and points in the direction of propagation of the illuminating field. In order to have a stable trapping configuration the gradient force must cancel out the scattering force such that the total force is zero. In a single beam tweezer trap the high gradients along beam propagation can be achieved by strongly focusing a laser beam. Laser beams are well described by a Gaussian TEM_{00} beam. The electric field distribution is given in equation 59 with $n = m = 0$. It relies on the paraxial approximation however which does not hold in a tight focusing scenario. A procedure to calculate the electric field near the focus is given in [92]. It is assumed that the electric field distribution of a Gaussian beam is incident on an aplanatic lens. The incoming field is entirely polarized along the x direction and propagates in positive z direction. The electric field distribution near the focus can be calculated to be

$$\mathbf{E}(\rho, \varphi, z) = -\frac{ikf}{2} E_0 e^{-ikf} \begin{bmatrix} I_{00} + I_{02}\cos(2\varphi) \\ I_{02}\sin(2\varphi) \\ -2iI_{01}\cos(\varphi) \end{bmatrix}. \tag{307}$$

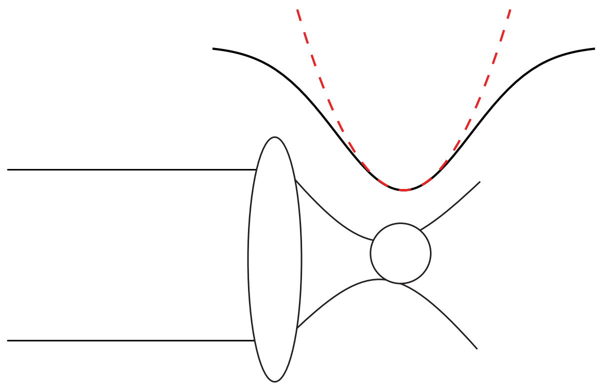

Figure 54: Single beam tweezer trap configuration. Gaussian beam coming form the right is tightly focused to form a three dimensional trap for a small dielectric particle. Trapping potential can be approximated by a harmonic one near the equilibrium position for all axes.

The distance ρ and angle φ are defined by $x = \rho \cos\varphi$ and $y = \rho \sin\varphi$, k is the wavenumber, f is the focal length of the lens and I_{00}, I_{01} and I_{02} are given by

$$I_{00} = \int_0^{\theta_m} f_w(\theta)\sqrt{\cos\theta}\sin\theta(1+\cos\theta)J_0(k\rho\sin\theta)e^{ikz\cos\theta}d\theta, \quad (308)$$

$$I_{01} = \int_0^{\theta_m} f_w(\theta)\sqrt{\cos\theta}\sin^2\theta J_1(k\rho\sin\theta)e^{ikz\cos\theta}d\theta, \quad (309)$$

$$I_{02} = \int_0^{\theta_m} f_w(\theta)\sqrt{\cos\theta}\sin\theta(1-\cos\theta)J_2(k\rho\sin\theta)e^{ikz\cos\theta}d\theta \quad (310)$$

Here θ is the angle between the incoming rays and the z axis and θ_m is the opening angle of the lens connected to the numerical aperture via $NA = \sin\theta_m$. The function $f_w(\theta)$ is called the apodization function

$$f_w(\theta) = e^{-\frac{f^2\sin^2\theta}{w_0^2}} \quad (311)$$

and J_n is the n-th order Bessel function. In this configuration the average scattering force will point in positive z direction only and shift the stable trapping position away form the focal point to $z = z_{eq}$. The calculated force for a spherical silica nanoparticle of radius $r = 105$ nm trapped by a Gaussian beam with waist of $w_0 = 4$ mm by a lens with $NA = 0.77$ and $f = 3.1$ mm is shown in figure 4 together with the intensity distribution along the x and y direction in the trapping plane $z = z_{eq}$. Near the focus the initial rotational symmetry of the input Gaussian beam is broken. The width of the intensity distribution along and across the direction of polarization of the input beam is non-degenerate. The intensity distribution is also no longer Gaussian.

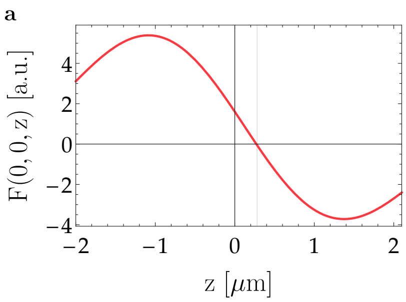

(a) Force along z.

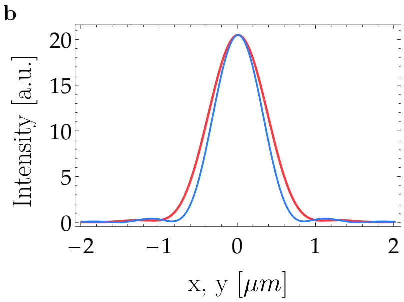

(b) Intensity along x and y.

Figure 55: Strongly focused Gaussian beam. **a.** Force along z direction on the optical axis ($x = y = 0$). The scattering force shifts the stable trapping position away from the beam waist at $z = 0$. **b.** Intensity distribution along x and y direction in the plane of $z = z_{eq}$ the stable trapping position. Due to strong focusing the width of the distribution is different along and across the polarization of the input beam.

Side maxima emerge which do not disturb the trapping of one particle but may introduce significant trap overlap when placing multiple traps close to each other.
For small displacements away form the equilibrium position $\rho, z \ll k$ the local trapping potentials can be approximated by harmonic potentials. The scattering force will be ignored for the following discussion since it adds only a tiny correction to the stiffness of the harmonic potential. The equilibrium position and trap stability can be analysed with the approach form above. In the harmonic approximation we aim to express the trapping potential as

$$\begin{aligned} U_h(x, y, z) &= \frac{m}{2}\left(\Omega_x^2 x^2 + \Omega_y^2 y^2 + \Omega_z^2 z^2\right) && (312) \\ &\approx -\frac{\alpha'}{4}\left(\mathbf{E}^* \cdot \mathbf{E}\right). && (313) \end{aligned}$$

This can be achieved by expanding the Bessel functions and exponential functions of the integrals 308, 309 and 310 by Taylor series and keeping only the quadratic terms in position.
Note to self. Maybe move this part to appendix or something.
The approximations used are

$$J_0(x) \approx 1 - \frac{x^2}{2} \tag{314}$$

$$J_1(x) \approx \frac{x}{2} \tag{315}$$

$$J_2(x) \approx \frac{x^2}{8} \tag{316}$$

$$e^{ix} \approx 1 + ix - \frac{x^2}{2}. \tag{317}$$

The integrals I_{00}, I_{01} and I_{02} simplify to

$$\begin{aligned}
I_{00} \quad \approx \quad & \int f_w(\theta)\sqrt{\cos\theta}\sin\theta(1+\cos\theta)\left(1-\frac{k^2\rho^2\cos^2\theta}{4}\right) \\
& \times\left(1+ikz\cos\theta-\frac{k^2z^2\cos^2\theta}{2}\right)d\theta \\
\approx \quad & \int f_w(\theta)\sqrt{\cos\theta}\sin\theta(1+\cos)\theta d\theta \\
& +ik\int f_w(\theta)\sqrt{\cos\theta}\sin\theta(1+\cos\theta)\cos\theta d\theta\cdot z \\
& -\frac{k^2}{2}\int f_w(\theta)\sqrt{\cos\theta}\sin\theta(1+\cos\theta)\cos^2\theta d\theta\cdot z^2 \\
& -\frac{k^2}{2}\int f_w(\theta)\sqrt{\cos\theta}\sin\theta(1+\cos\theta)\sin^2\theta d\theta\cdot\rho^2 \\
& -i\frac{k^3}{4}\int f_w(\theta)\sqrt{\cos\theta}\sin\theta(1+\cos\theta)\sin^2\theta\cos\theta d\theta\cdot\rho^2 z \\
& k\frac{k^4}{8}\int f_w(\theta)\sqrt{\cos\theta}\sin\theta(1+\cos\theta)\sin^2\theta\cos^2\theta d\theta\cdot\rho^2z^2
\end{aligned}$$

$$\begin{aligned}
I_{01} \quad \approx \quad & \int f_w(\theta)\sqrt{\cos\theta}\sin^2\theta\frac{k\rho\sin\theta}{2}\left(1+ikz\cos\theta-\frac{k^2z^2\cos^2\theta}{2}\right)d\theta \\
= \quad & \frac{k}{2}\int f_w(\theta)\sqrt{\cos\theta}\sin^3\theta d\theta\cdot\rho \\
& +i\frac{k^2}{2}\int f_w(\theta)\sqrt{\cos\theta}\sin^3\theta\cos\theta d\theta\cdot\rho z \\
& -\frac{k^3}{4}\int f_w(\theta)\sqrt{\cos\theta}\sin^3\theta\cos^2\theta d\theta\cdot\rho z^2
\end{aligned}$$

$$\begin{aligned}
I_{02} \quad \approx \quad & \int f_w(\theta)\sqrt{\cos\theta}\sin\theta(1-\cos\theta)\frac{k^2\rho^2\sin^2\theta}{8}\left(1+ikz\cos\theta-\frac{k^2z^2\cos^2\theta}{2}\right)d\theta \\
= \quad & \frac{k^2}{8}\int f_w(\theta)\sqrt{\cos\theta}\sin^3\theta(1-\cos\theta)d\theta\cdot\rho^2 \\
& +i\frac{k^3}{8}\int f_w(\theta)\sqrt{\cos\theta}\sin^3\theta(1-\cos\theta)\cos\theta d\theta\cdot\rho^2 z \\
& -\frac{k^4}{16}\int f_w(\theta)\sqrt{\cos\theta}\sin^3\theta(1-\cos\theta)\cos^2\theta d\theta\cdot\rho^2z^2
\end{aligned}$$

All mixed terms will be dropped, even at order ρz (but why? cause it doesn't fit the harmonic potential...) That leaves

$$\begin{aligned}
I_{00} &\approx i_{00}+ii_{00}^{z}z+i_{00}^{zz}z^2+i_{00}^{\rho\rho}\rho^2 \\
I_{01} &\approx i_{01}^{\rho}\rho \\
I_{02} &\approx i_{02}^{\rho\rho}\rho^2
\end{aligned}$$

The electric field vector reduces to

$$\mathbf{E}(\rho,\varphi,z) \approx -\frac{ikf}{2}E_0 e^{-ikf}\begin{bmatrix} i_{00} + i i_{00}^{z} z + i_{00}^{zz} z^2 + i_{00}^{\rho\rho}\rho^2 + i_{02}^{\rho\rho}\rho^2\cos(2\varphi) \\ i_{02}^{\rho\rho}\rho^2\sin(2\varphi) \\ -2i i_{01}^{\rho}\cos\varphi 6 \end{bmatrix}, \tag{318}$$

where all terms of order $\mathcal{O}(z^3)$ or $\mathcal{O}(\rho^3)$ or higher and mixed terms are omitted. There are now six simpler integrals that need to be evaluated

$$i_{00} = \int_0^{\theta_m} f_w(\theta)\sqrt{\cos\theta}\sin\theta(1+\cos\theta)d\theta \tag{319}$$

$$i_{00}^{z} = k\int_0^{\theta_m} f_w(\theta)\sqrt{\cos\theta}\sin\theta(1+\cos\theta)\cos\theta d\theta \tag{320}$$

$$i_{00}^{zz} = -\frac{k^2}{2}\int_0^{\theta_m} f_w(\theta)\sqrt{\cos\theta}\sin\theta(1+\cos\theta)\cos^2\theta d\theta \tag{321}$$

$$i_{00}^{\rho\rho} = -\frac{k^2}{2}\int_0^{\theta_m} f_w(\theta)\sqrt{\cos\theta}\sin^3\theta(1+\cos\theta)d\theta \tag{322}$$

$$i_{01}^{\rho} = \frac{k}{2}\int_0^{\theta_m} f_w(\theta)\sqrt{\cos\theta}\sin^3\theta d\theta \tag{323}$$

$$i_{02}^{\rho\rho} = \frac{k^2}{8}\int_0^{\theta_m} f_w(\theta)\sqrt{\cos\theta}\sin^3\theta(1-\cos\theta)d\theta. \tag{324}$$

First to calculate the potential E^*E is calculated with ρ and φ in the expression. Next step is to replace them.

$$\begin{aligned} U_h(\rho,\varphi,z) = & -\frac{\alpha'}{4}E_0^2\frac{k^2f^2}{4}\Big({i_{00}}^2 + {i_{00}^{z}}^2 z^2 + 2i_{00}i_{00}^{zz}z^2 + 2i_{00}i_{00}^{\rho\rho}\rho^2 \\ & +2i_{00}i_{02}^{\rho\rho}\cos(2\varphi)\rho^2 + 4{i_{01}^{\rho}}^2\rho^2\cos^2\varphi\Big) \end{aligned} \tag{325}$$

End of note

Finally calculating the potential and again dropping all higher order and mixed terms leads to

$$\begin{aligned} U_h(x,y,z) = & -\frac{\alpha'}{4}\frac{P_0k^2f^2}{\varepsilon_0 c\pi w_0^2}\Big[\Big({i_{00}^{z}}^2 + 2i_{00}i_{00}^{zz}\Big)z^2 \\ & + \big(2i_{00}i_{00}^{\rho\rho} - 2i_{00}i_{02}^{\rho\rho}\big)y^2 \\ & + \Big(2i_{00}i_{00}^{\rho\rho} + 2i_{00}i_{02}^{\rho\rho} + 4{i_{01}^{\rho}}^2\Big)x^2\Big]. \end{aligned} \tag{326}$$

The electric field was replaced by the incident power $|E_0|^2 = 4P_0/(\varepsilon_0 c\pi w_0^2)$ of a Gaussian beam. This lets us read off the oscillation frequencies for the respective center of mass motion as

$$\Omega_x = \frac{kf}{w_0}\sqrt{-\frac{\alpha'}{m}\frac{P_0}{\varepsilon_0 c\pi}\Big(i_{00}i_{00}^{\rho\rho} + i_{00}i_{02}^{\rho\rho} + 2{i_{01}^{\rho}}^2\Big)}, \tag{327}$$

$$\Omega_y = \frac{kf}{w_0}\sqrt{-\frac{\alpha'}{m}\frac{P_0}{\varepsilon_0 c\pi}\big(i_{00}i_{00}^{\rho\rho} - i_{00}i_{02}^{\rho\rho}\big)}, \tag{328}$$

$$\Omega_z = \frac{kf}{w_0}\sqrt{-\frac{\alpha'}{2m}\frac{P_0}{\varepsilon_0 c\pi}\big({i_{00}^{z}}^2 + 2i_{00}i_{00}^{zz}\big)}. \tag{329}$$

For an effective numerical aperture of $NA_{eff} = 0.7$ this gives frequencies of $(\Omega_x, \Omega_y, \Omega_z)/2\pi = (287.1, 305.6, 72.2)$ kHz which is similar to the measured oscillation frequencies. The root mean square displacement for a particle in a harmonic trap is given by

$$i_{rms} = \sqrt{\frac{2k_B T}{m\Omega_i^2}} \qquad , \text{for } i = x, y, z \tag{330}$$

which is, for the above parameters and the bath temperature of $T = 300$ K, $(x_{rms}, y_{rms}, z_{rms}) = (19, 18, 75)$ nm. The error made by the harmonic approximation on the force acting on the particle for these displacements is less than 3% compared to the full calculation. Especially if the particle motion is further cooled, the harmonic approximation is valid.

[1] B. P. Abbott et al. "Observation of Gravitational Waves from a Binary Black Hole Merger." In: *Phys. Rev. Lett.* 116 (6 Feb. 2016), p. 061102. DOI: 10.1103/PhysRevLett.116.061102. URL: https://link.aps.org/doi/10.1103/PhysRevLett.116.061102.

[2] Alex Abramovici et al. "LIGO: The Laser Interferometer Gravitational -Wave Observatory." In: *Science* 256.5055 (Apr. 1992), pp. 325–333. DOI: 10.1126/science.256.5055.325. URL: https://doi.org/10.1126/science.256.5055.325.

[3] Gadi Afek, Fernando Monteiro, Jiaxiang Wang, Benjamin Siegel, Sumita Ghosh, and David C. Moore. "Limits on the abundance of millicharged particles bound to matter." In: *Phys. Rev. D* 104 (1 July 2021), p. 012004. DOI: 10.1103/PhysRevD.104.012004. URL: https://link.aps.org/doi/10.1103/PhysRevD.104.012004.

[4] Yoshihiko Arita, Mingzhou Chen, Ewan M. Wright, and Kishan Dholakia. "Dynamics of a levitated microparticle in vacuum trapped by a perfect vortex beam: three-dimensional motion around a complex optical potential." In: *J. Opt. Soc. Am. B* 34.6 (June 2017), pp. C14–C19. URL: https://opg.optica.org/josab/abstract.cfm?URI=josab-34-6-C14.

[5] Yoshihiko Arita, Stephen H. Simpson, Graham D. Bruce, Ewan M. Wright, Pavel Zemánek, and Kishan Dholakia. "Cooling the optical-spin driven limit cycle oscillations of a levitated gyroscope." In: *Communications Physics* 6.1 (2023), p. 238. ISSN: 2399-3650. DOI: 10.1038/s42005-023-01336-4. URL: https://doi.org/10.1038/s42005-023-01336-4.

[6] Yoshihiko Arita, Ewan M. Wright, and Kishan Dholakia. "Optical binding of two cooled micro-gyroscopes levitated in vacuum." In: *Optica* 5.8 (Aug. 2018), pp. 910–917. DOI: 10.1364/OPTICA.5.000910. URL: https://opg.optica.org/optica/abstract.cfm?URI=optica-5-8-910.

[7] Peter Asenbaum, Stefan Kuhn, Stefan Nimmrichter, Ugur Sezer, and Markus Arndt. "Cavity cooling of free silicon nanoparticles in high vacuum." In: *Nature Communications* 4.1 (2013), p. 2743. ISSN: 2041-1723. DOI: 10.1038/ncomms3743. URL: https://doi.org/10.1038/ncomms3743.

[8] A. Ashkin and J. M. Dziedzic. "Optical Levitation by Radiation Pressure." In: *Appl. Phys. Lett.* 19.8 (Oct. 1971), pp. 283–285. ISSN: 0003-6951. DOI: 10.1063/1.1653919. URL: https://doi.org/10.1063/1.1653919.

[9] Markus Aspelmeyer, Tobias J. Kippenberg, and Florian Marquardt. "Cavity optomechanics." In: *Rev. Mod. Phys.* 86 (4 Dec. 2014), pp. 1391–1452. DOI: 10.1103/RevModPhys.86.1391. URL: http://link.aps.org/doi/10.1103/RevModPhys.86.1391.

[10] Daniel Barredo, Sylvain de Léséleuc, Vincent Lienhard, Thierry Lahaye, and Antoine Browaeys. "An atom-by-atom assembler of defect-free arbitrary two-dimensional atomic arrays." In: *Science* 354.6315 (Nov. 2016), pp. 1021–1023. DOI: 10.1126/science.aah3778. URL: https://doi.org/10.1126/science.aah3778.

[11] Charles P. Blakemore, Alexander Fieguth, Akio Kawasaki, Nadav Priel, Denzal Martin, Alexander D. Rider, Qidong Wang, and Giorgio Gratta. "Search for non-Newtonian interactions at micrometer scale with a levitated test mass." In: *Phys. Rev. D* 104 (6 Sept. 2021), p. L061101. DOI: 10.1103/PhysRevD.104.L061101. URL: https://link.aps.org/doi/10.1103/PhysRevD.104.L061101.

[12] I. Brandão, D. Tandeitnik, and Guerreiro T. "Coherent scattering-mediated correlations between levitated nanospheres." In: *Quantum Science and Technology* 6.4 (2021), p. 045013. DOI: 10.1088/2058-9565/ac1a01. URL: https://doi.org/10.1088/2058-9565/ac1a01.

[13] O. Brzobohatý, V. Karásek, M. Šiler, L. Chvátal, T. Čižmár, and P. Zemánek. "Experimental demonstration of optical transport, sorting and self-arrangement using a 'tractor beam'." In: *Nature Photonics* 7.2 (2013), pp. 123–127. ISSN: 1749-4893. DOI: 10.1038/nphoton.2012.332. URL: https://doi.org/10.1038/nphoton.2012.332.

[14] Oto Brzobohatý, Lukáš Chvátal, Alexandr Jonáš, Martin Šiler, Jan Kaňka, Jan Ježek, and Pavel Zemánek. "Tunable Soft-Matter Optofluidic Waveguides Assembled by Light." In: *ACS Photonics* 6.2 (Feb. 2019), pp. 403–410. DOI: 10.1021/acsphotonics.8b01331. URL: https://doi.org/10.1021/acsphotonics.8b01331.

[15] Michael M. Burns, Jean-Marc Fournier, and Jene A. Golovchenko. "Optical binding." In: *Phys. Rev. Lett.* 63 (12 Sept. 1989), pp. 1233–1236. DOI: 10.1103/PhysRevLett.63.1233. URL: https://link.aps.org/doi/10.1103/PhysRevLett.63.1233.

[16] Dmitry S. Bykov, Pau Mestres, Lorenzo Dania, Lisa Schmöger, and Tracy E. Northup. "Direct loading of nanoparticles under high vacuum into a Paul trap for levitodynamical experiments." In: *Appl. Phys. Lett.* 115.3 (July 2019), p. 034101. ISSN: 0003-6951. DOI: 10.1063/1.5109645. URL: https://doi.org/10.1063/1.5109645.

[17] Dmitry S. Bykov, Shangran Xie, Richard Zeltner, Andrey Machnev, Gordon K. L. Wong, Tijmen G. Euser, and Philip St. J. Russell. "Long-range optical trapping and binding of microparticles in hollow-core photonic crystal fibre." In: *Light: Science & Applications* 7.1 (2018), p. 22. ISSN: 2047-7538. DOI: 10.1038/s41377-018-0015-z. URL: https://doi.org/10.1038/s41377-018-0015-z.

[18] A. O. Caldeira and A. J. Leggett. "Influence of Dissipation on Quantum Tunneling in Macroscopic Systems." In: *Phys. Rev. Lett.* 46 (4 Jan. 1981), pp. 211–214. DOI: 10.1103/PhysRevLett.46.211. URL: https://link.aps.org/doi/10.1103/PhysRevLett.46.211.

[19] A. O. Caldeira and A. J. Leggett. "Quantum tunnelling in a dissipative system." In: *Annals of Physics* 149.2 (1983), pp. 374–456. ISSN: 0003-4916. DOI: 10.1016/0003-4916(83)90202-6. URL: https://www.sciencedirect.com/science/article/pii/0003491683902026.

[20] D Carney et al. "Mechanical quantum sensing in the search for dark matter." In: *Quantum Science and Technology* 6.2 (Jan. 2021), p. 024002. DOI: 10.1088/2058-9565/abcfcd. URL: https://doi.org/10.1088/2058-9565/abcfcd.

[21] Hilton W. Chan, Adam T. Black, and Vladan Vuletic. "Observation of Collective-Emission-Induced Cooling of Atoms in an Optical Cavity." In: *Phys. Rev. Lett.* 90 (6 Feb. 2003), p. 063003. DOI: 10.1103/PhysRevLett.90.063003. URL: https://link.aps.org/doi/10.1103/PhysRevLett.90.063003.

[22] Jasper Chan, T. P. Mayer Alegre, Amir H. Safavi-Naeini, Jeff T. Hill, Alex Krause, Simon Gröblacher, Markus Aspelmeyer, and Oskar Painter. "Laser cooling of a nanomechanical oscillator into its quantum ground state." In: *Nature* 478.7367 (2011), pp. 89–92. ISSN: 1476-4687. DOI: 10.1038/nature10461. URL: https://doi.org/10.1038/nature10461.

[23] D. E. Chang, C. A. Regal, S. B. Papp, D. J. Wilson, J. Ye, O. Painter, H. J. Kimble, and P. Zoller. "Cavity opto-mechanics using an optically levitated nanosphere." In: *Proceedings of the National Academy of Sciences* 107.3 (Jan. 2010), pp. 1005–1010. DOI: 10.1073/pnas.0912969107. URL: https://doi.org/10.1073/pnas.0912969107.

[24] Chris Chatfield. *The Analysis of Time Series*. 6th Edition. Chapman and Hall/CRC, 2003. ISBN: 9780429208706. DOI: https://doi.org/10.4324/9780203491683.

[25] Anil Kumar Chauhan, Ondřej Černotík, and Radim Filip. "Stationary Gaussian entanglement between levitated nanoparticles." In: *New Journal of Physics* 22.12 (2020), p. 123021. DOI: 10.1088/1367-2630/abcce6. URL: https://doi.org/10.1088/1367-2630/abcce6.

[26] P. C. Chaumet and M. Nieto-Vesperinas. "Time-averaged total force on a dipolar sphere in an electromagnetic field." In: *Opt. Lett.* 25.15 (2000), pp. 1065–1067. DOI: 10.1364/OL.25.001065. URL: https://opg.optica.org/ol/abstract.cfm?URI=ol-25-15-1065.

[27] Mario A. Ciampini, Tobias Wenzl, Michael Konopik, Gregor Thalhammer-Thurner, Markus Aspelmeyer, Eric Lutz, and Nikolai Kiesel. "Erasure of a nonequilibrium memory beyond Landauer's bound using levitated optomechanics with spatio-temporal optical control." In: *Phys. Rev. Res.* 7 (4 Dec. 2025), p. 043321. DOI: 10.1103/r81x-zblx. URL: https://link.aps.org/doi/10.1103/r81x-zblx.

[28] A. A. Clerk, M. H. Devoret, S. M. Girvin, Florian Marquardt, and R. J. Schoelkopf. "Introduction to quantum noise, measurement, and amplification." In: *Rev. Mod. Phys.* 82 (2 Apr. 2010), pp. 1155–1208. DOI: 10.1103/RevModPhys.82.1155. URL: http://link.aps.org/doi/10.1103/RevModPhys.82.1155.

[29] M. F. Colombano, G. Arregui, F. Bonell, N. E. Capuj, E. Chavez-Angel, A. Pitanti, S. O. Valenzuela, C. M. Sotomayor-Torres, D. Navarro-Urrios, and M. V. Costache. "Ferromagnetic Resonance Assisted Optomechanical Magnetometer." In: *PRL* 125.14 (Oct. 2020), p. 147201. DOI: 10.1103/PhysRevLett.125.147201. URL: https://link.aps.org/doi/10.1103/PhysRevLett.125.147201.

[30] Corentin Coulais, Romain Fleury, and Jasper van Wezel. "Topology and broken Hermiticity." In: *Nature Physics* 17.1 (2021), pp. 9–13. ISSN: 1745-2481. DOI: 10.1038/s41567-020-01093-z. URL: https://doi.org/10.1038/s41567-020-01093-z.

[31] Jennifer E. Curtis, Brian A. Koss, and David G. Grier. "Dynamic holographic optical tweezers." In: *Optics Communications* 207.1 (2002), pp. 169–175. ISSN: 0030-4018. DOI: 10.1016/S0030-4018(02)01524-9. URL: https://www.sciencedirect.com/science/article/pii/S0030401802015249.

[32] Lorenzo Dania, Oscar Schmitt Kremer, Johannes Piotrowski, Davide Candoli, Jayadev Vijayan, Oriol Romero-Isart, Carlos Gonzalez-Ballestero, Lukas Novotny, and Martin Frimmer. "High-

purity quantum optomechanics at room temperature." In: *Nature Physics* 21.10 (2025), pp. 1603–1608. ISSN: 1745-2481. DOI: 10.1038/s41567-025-02976-9. URL: https://doi.org/10.1038/s41567-025-02976-9.

[33] Uroš Delić. "Quantum control of levitated nanospheres." PhD thesis. univie, 2018.

[34] Uroš Delić, Manuel Reisenbauer, Kahan Dare, David Grass, Vladan Vuletić, Nikolai Kiesel, and Markus Aspelmeyer. "Cooling of a levitated nanoparticle to the motional quantum ground state." In: *Science* 367.6480 (Feb. 2020), p. 892. DOI: 10.1126/science.aba3993. URL: http://science.sciencemag.org/content/367/6480/892.abstract.

[35] Uroš Delić, Manuel Reisenbauer, David Grass, Nikolai Kiesel, Vladan Vuletić, and Markus Aspelmeyer. "Cavity Cooling of a Levitated Nanosphere by Coherent Scattering." In: *Phys. Rev. Lett.* 122 (12 Mar. 2019), p. 123602. DOI: 10.1103/PhysRevLett.122.123602. URL: https://link.aps.org/doi/10.1103/PhysRevLett.122.123602.

[36] Q. Deplano, A. Pontin, A. Ranfagni, F. Marino, and F. Marin. "High purity two-dimensional levitated mechanical oscillator." In: *Nature Communications* 16.1 (2025), p. 4215. ISSN: 2041-1723. DOI: 10.1038/s41467-025-59213-3. URL: https://doi.org/10.1038/s41467-025-59213-3.

[37] Kishan Dholakia and Pavel Zemánek. "Colloquium: Gripped by light: Optical binding." In: *Rev. Mod. Phys.* 82 (2 June 2010), pp. 1767–1791. DOI: 10.1103/RevModPhys.82.1767. URL: https://link.aps.org/doi/10.1103/RevModPhys.82.1767.

[38] Lajos Diósi. "Laser linewidth hazard in optomechanical cooling." In: *Phys. Rev. A* 78 (2 Aug. 2008), p. 021801. DOI: 10.1103/PhysRevA.78.021801. URL: https://link.aps.org/doi/10.1103/PhysRevA.78.021801.

[39] Jörg Doppler, Alexei A. Mailybaev, Julian Böhm, Ulrich Kuhl, Adrian Girschik, Florian Libisch, Thomas J. Milburn, Peter Rabl, Nimrod Moiseyev, and Stefan Rotter. "Dynamically encircling an exceptional point for asymmetric mode switching." In: *Nature* 537.7618 (2016), pp. 76–79. ISSN: 1476-4687. DOI: 10.1038/nature18605. URL: https://doi.org/10.1038/nature18605.

[40] R. W. P. Drever, J. L. Hall, F. V. Kowalski, J. Hough, G. M. Ford, A. J. Munley, and H. Ward. "Laser phase and frequency stabilization using an optical resonator." In: *Applied Physics B* 31.2 (1983), pp. 97–105. ISSN: 1432-0649. DOI: 10.1007/BF00702605. URL: https://doi.org/10.1007/BF00702605.

[41] Manuel Endres, Hannes Bernien, Alexander Keesling, Harry Levine, Eric R. Anschuetz, Alexandre Krajenbrink, Crystal Senko, Vladan Vuletic, Markus Greiner, and Mikhail D. Lukin. "Atom-by-atom assembly of defect-free one-dimensional cold atom arrays." In: *Science* 354.6315 (Nov. 2016), pp. 1024–1027. DOI: 10.1126/science.aah3752. URL: https://doi.org/10.1126/science.aah3752.

[42] Paul S. Epstein. "On the Resistance Experienced by Spheres in their Motion through Gases." In: *PR* 23.6 (June 1924), pp. 710–733. DOI: 10.1103/PhysRev.23.710. URL: https://link.aps.org/doi/10.1103/PhysRev.23.710.

[43] Jana Flajšmanová, Martin Šiler, Petr Jedlička, František Hrubý, Oto Brzobohatý, Radim Filip, and Pavel Zemánek. "Using the transient trajectories of an optically levitated nanoparticle to characterize a stochastic Duffing oscillator." In: *Scientific Reports* 10.1 (2020), p. 14436. ISSN: 2045-2322. DOI: 10.1038/s41598-020-70908-z. URL: https://doi.org/10.1038/s41598-020-70908-z.

[44] P. Z. G. Fonseca, E. B. Aranas, J. Millen, T. S. Monteiro, and P. F. Barker. "Nonlinear Dynamics and Strong Cavity Cooling of Levitated Nanoparticles." In: *Phys. Rev. Lett.* 117 (17 Oct. 2016), p. 173602. DOI: 10.1103/PhysRevLett.117.173602. URL: https://link.aps.org/doi/10.1103/PhysRevLett.117.173602.

[45] G. W. Ford, J. T. Lewis, and R. F. O'Connell. "Quantum Langevin equation." In: *Phys. Rev. A* 37 (11 June 1988), pp. 4419–4428. DOI: 10.1103/PhysRevA.37.4419. URL: https://link.aps.org/doi/10.1103/PhysRevA.37.4419.

[46] Moritz Forsch, Robert Stockill, Andreas Wallucks, Igor Marinković, Claus Gärtner, Richard A. Norte, Frank van Otten, Andrea Fiore, Kartik Srinivasan, and Simon Gröblacher. "Microwave-to-optics conversion using a mechanical oscillator in its quantum ground state." In: *Nature Physics* 16.1 (2020), pp. 69–74. ISSN: 1745-2481. DOI: 10.1038/s41567-019-0673-7. URL: https://doi.org/10.1038/s41567-019-0673-7.

[47] Kevin M. Fortier, Soo Y. Kim, Michael J. Gibbons, Peyman Ahmadi, and Michael S. Chapman. "Deterministic Loading of Individual Atoms to a High-Finesse Optical Cavity." In: *Phys. Rev. Lett.* 98 (23 June 2007), p. 233601. DOI: 10.1103/PhysRevLett.98.233601. URL: https://link.aps.org/doi/10.1103/PhysRevLett.98.233601.

[48] Michel Fruchart, Ryo Hanai, Peter B. Littlewood, and Vincenzo Vitelli. "Non-reciprocal phase transitions." In: *Nature* 592.7854 (2021), pp. 363–369. ISSN: 1476-4687. DOI: 10.1038/s41586-021-03375-9. URL: https://doi.org/10.1038/s41586-021-03375-9.

[49] C. W. Gardiner and M. J. Collett. "Input and output in damped quantum systems: Quantum stochastic differential equations and the master equation." In: *Phys. Rev. A* 31 (6 June 1985), pp. 3761–3774. DOI: 10.1103/PhysRevA.31.3761. URL: https://link.aps.org/doi/10.1103/PhysRevA.31.3761.

[50] E. Gavartin, P. Verlot, and T. J. Kippenberg. "A hybrid on-chip optomechanical transducer for ultrasensitive force measurements." In: *Nature Nanotechnology* 7.8 (2012), pp. 509–514. ISSN: 1748-3395. DOI: 10.1038/nnano.2012.97. URL: https://doi.org/10.1038/nnano.2012.97.

[51] C. Genes, D. Vitali, P. Tombesi, S. Gigan, and M. Aspelmeyer. "Ground-state cooling of a micromechanical oscillator: Comparing cold damping and cavity-assisted cooling schemes." In: *Phys. Rev. A* 77 (3 Mar. 2008), p. 033804. DOI: 10.1103/PhysRevA.77.033804. URL: https://link.aps.org/doi/10.1103/PhysRevA.77.033804.

[52] Andrew A. Geraci, Scott B. Papp, and John Kitching. "Short-Range Force Detection Using Optically Cooled Levitated Microspheres." In: *Phys. Rev. Lett.* 105 (10 Aug. 2010), p. 101101. DOI: 10.1103/PhysRevLett.105.101101. URL: https://link.aps.org/doi/10.1103/PhysRevLett.105.101101.

[53] Roy J. Glauber. "The Quantum Theory of Optical Coherence." In: *PR* 130.6 (June 1963), pp. 2529–2539. DOI: 10.1103/PhysRev.130.2529. URL: https://link.aps.org/doi/10.1103/PhysRev.130.2529.

[54] C. Gonzalez-Ballestero, M. Aspelmeyer, L. Novotny, R. Quidant, and O. Romero-Isart. "Levitodynamics: Levitation and control of microscopic objects in vacuum." In: *Science* 374.6564 (Jan. 2023), eabg3027. DOI: 10.1126/science.abg3027. URL: https://doi.org/10.1126/science.abg3027.

[55] C. Gonzalez-Ballestero, P. Maurer, D. Windey, L. Novotny, R. Reimann, and O. Romero-Isart. "Theory for cavity cooling of levitated nanoparticles via coherent scattering: Master equation approach." In: *Phys. Rev. A* 100 (1 July 2019), p. 013805. DOI: 10.1103/PhysRevA.100.013805. URL: https://link.aps.org/doi/10.1103/PhysRevA.100.013805.

[56] David Grass. "Levitated optomechanics in vacuum using hollow core photonic crystal fibers and optical cavities." PhD thesis. Universität Wien, 2018. DOI: 10.25365/thesis.54138.

[57] Erik Hebestreit, Martin Frimmer, René Reimann, and Lukas Novotny. "Sensing Static Forces with Free-Falling Nanoparticles." In: *PRL* 121.6 (Aug. 2018), p. 063602. DOI: 10.1103/PhysRevLett.121.063602. URL: https://link.aps.org/doi/10.1103/PhysRevLett.121.063602.

[58] Erik Hebestreit, René Reimann, Martin Frimmer, and Lukas Novotny. "Measuring the internal temperature of a levitated nanoparticle in high vacuum." In: *Phys. Rev. A* 97 (4 Apr. 2018), p. 043803. DOI: 10.1103/PhysRevA.97.043803. URL: https://link.aps.org/doi/10.1103/PhysRevA.97.043803.

[59] Georg Heinrich, Max Ludwig, Jiang Qian, Björn Kubala, and Florian Marquardt. "Collective Dynamics in Optomechanical Arrays." In: *Phys. Rev. Lett.* 107 (4 July 2011), p. 043603. DOI: 10.1103/PhysRevLett.107.043603. URL: https://link.aps.org/doi/10.1103/PhysRevLett.107.043603.

[60] Jason Hoelscher-Obermaier. "Generation and detection of quantum entanglement in optomechanical systems." PhD thesis. Wien: University of Vienna, 2017, ix, 211 Seiten, Illustrationen, Diagramme. URL: https://ubdata.univie.ac.at/AC15151939.

[61] Wayne M. Itano and D. J. Wineland. "Laser cooling of ions stored in harmonic and Penning traps." In: *PRA* 25.1 (Jan. 1982), pp. 35–54. DOI: 10.1103/PhysRevA.25.35. URL: https://link.aps.org/doi/10.1103/PhysRevA.25.35.

[62] Vijay Jain. "Leviated optomechanics at the photon recoil limit." PhD thesis. ETH Zürich, 2017.

[63] Vijay Jain, Jan Gieseler, Clemens Moritz, Christoph Dellago, Romain Quidant, and Lukas Novotny. "Direct Measurement of Photon Recoil from a Levitated Nanoparticle." In: *Phys. Rev. Lett.* 116 (24 June 2016), p. 243601. DOI: 10.1103/PhysRevLett.116.243601. URL: https://link.aps.org/doi/10.1103/PhysRevLett.116.243601.

[64] K. Karrai, I. Favero, and C. Metzger. "Doppler Optomechanics of a Photonic Crystal." In: *Phys. Rev. Lett.* 100 (24 June 2008), p. 240801. DOI: 10.1103/PhysRevLett.100.240801. URL: https://link.aps.org/doi/10.1103/PhysRevLett.100.240801.

[65] Ayub Khodaee, Kahan Dare, Aisling Johnson, Uroš Delić, and Markus Aspelmeyer. "Dry launching of silica nanoparticles in vacuum." In: *AIP Advances* 12.12 (Dec. 2022), p. 125023. ISSN: 2158-3226. DOI: 10.1063/5.0124029. URL: https://doi.org/10.1063/5.0124029.

[66] Nikolai Kiesel, Florian Blaser, Uroš Delić, David Grass, Rainer Kaltenbaek, and Markus Aspelmeyer. "Cavity cooling of an optically levitated submicron particle." In: *Proceedings of the National Academy of Sciences* 110.35 (2013), pp. 14180–14185. DOI: 10.1073/pnas.1309167110. URL: http://www.pnas.org/content/110/35/14180.abstract.

[67] H. J. Kimble. "The quantum internet." In: *Nature* 453.7198 (2008), pp. 1023–1030. ISSN: 1476-4687. DOI: 10.1038/nature07127. URL: https://doi.org/10.1038/nature07127.

[68] T J Kippenberg, A Schliesser, and M L Gorodetsky. "Phase noise measurement of external cavity diode lasers and implications for optomechanical sideband cooling of GHz mechanical modes." In: *New Journal of Physics* 15.1 (2013), p. 015019. URL: http://stacks.iop.org/1367-2630/15/i=1/a=015019.

[69] Alexander G. Krause, Martin Winger, Tim D. Blasius, Qiang Lin, and Oskar Painter. "A high-resolution microchip optomechanical accelerometer." In: *Nature Photonics* 6.11 (2012), pp. 768–772. ISSN: 1749-4893. DOI: 10.1038/nphoton.2012.245. URL: https://doi.org/10.1038/nphoton.2012.245.

[70] R Kubo. "The fluctuation-dissipation theorem." In: *Reports on Progress in Physics* 29.1 (Jan. 1966), p. 255. DOI: 10.1088/0034-4885/29/1/306. URL: https://dx.doi.org/10.1088/0034-4885/29/1/306.

[71] Stefan Kuhn, Peter Asenbaum, Alon Kosloff, Michele Sclafani, Benjamin A. Stickler, Stefan Nimmrichter, Klaus Hornberger, Ori Cheshnovsky, Fernando Patolsky, and Markus Arndt. "Cavity-Assisted Manipulation of Freely Rotating Silicon Nanorods in High Vacuum." In: *Nano Lett.* 15.8 (Aug. 2015), pp. 5604–5608. ISSN: 1530-6984. DOI: 10.1021/acs.nanolett.5b02302. URL: https://doi.org/10.1021/acs.nanolett.5b02302.

[72] W. Lechner, S. J. M. Habraken, N. Kiesel, M. Aspelmeyer, and P. Zoller. "Cavity Optomechanics of Levitated Nanodumbbells: Nonequilibrium Phases and Self-Assembly." In: *Phys. Rev. Lett.* 110 (14 Apr. 2013), p. 143604. DOI: 10.1103/PhysRevLett.110.143604. URL: https://link.aps.org/doi/10.1103/PhysRevLett.110.143604.

[73] Aodong Li et al. "Exceptional points and non-Hermitian photonics at the nanoscale." In: *Nature Nanotechnology* 18.7 (2023), pp. 706–720. ISSN: 1748-3395. DOI: 10.1038/s41565-023-01408-0. URL: https://doi.org/10.1038/s41565-023-01408-0.

[74] Stefan Lindner, Paul Juschitz, Jakob Rieser, Yaakov Y. Fein, Maxime Debiossac, Mario A. Ciampini, Markus Aspelmeyer, and Nikolai Kiesel. "Hollow-core fiber loading of nanoparticles into ultra-high vacuum." In: *Appl. Phys. Lett.* 124.14 (Apr. 2024), p. 143501. ISSN: 0003-6951. DOI: 10.1063/5.0190658. URL: https://doi.org/10.1063/5.0190658.

[75] Shengyan Liu, Zhang-qi Yin, and Tongcang Li. "Prethermalization and Nonreciprocal Phonon Transport in a Levitated Optomechanical Array." In: *Advanced Quantum Technologies* 3.3 (Jan. 2020), p. 1900099. ISSN: 2511-9044. DOI: 10.1002/qute.201900099. URL: http://dx.doi.org/10.1002/qute.201900099.

[76] Vojtěch Liška, Tereza Zemánková, Vojtěch Svak, Petr Jákl, Jan Ježek, Martin Bránecký, Stephen H. Simpson, Pavel Zemánek, and Oto Brzobohatý. "Cold damping of levitated optically coupled nanoparticles." In: *Optica* 10.9 (Sept. 2023), pp. 1203–1209. DOI: 10.1364/OPTICA.496072. URL: https://opg.optica.org/optica/abstract.cfm?URI=optica-10-9-1203.

[77] Vojtěch Liška, Tereza Zemánková, Petr Jákl, Martin Šiler, Stephen H. Simpson, Pavel Zemánek, and Oto Brzobohatý. "PT-like phase transition and limit cycle oscillations in non-reciprocally coupled optomechanical oscillators levitated in vacuum." In: *Nature Physics* 20.10 (2024), pp. 1622–1628. ISSN: 1745-2481. DOI: 10.1038/s41567-024-02590-1. URL: https://doi.org/10.1038/s41567-024-02590-1.

[78] Sarah A. M. Loos and Sabine H. L. Klapp. "Irreversibility, heat and information flows induced by non-reciprocal interactions." In: *New Journal of Physics* 22.12 (2020), p. 123051. DOI: 10.1088/1367-2630/abcc1e. URL: https://doi.org/10.1088/1367-2630/abcc1e.

[79] R. Loudon. *The Quantum Theory of Light*. OUP Oxford, 2000. ISBN: 9780191589782. URL: https://books.google.at/books?id=AEkfajgqldoC.

[80] José A. S. Lourenço, Gerard Higgins, Chi Zhang, Markus Hennrich, and Tommaso Macrì. "Non-Hermitian dynamics and $\mathcal{PT}$-symmetry breaking in interacting mesoscopic Rydberg platforms." In: *PRA* 106.2 (Aug. 2022), p. 023309. DOI: 10.1103/PhysRevA.106.023309. URL: https://link.aps.org/doi/10.1103/PhysRevA.106.023309.

[81] Lorenzo Magrini, Philipp Rosenzweig, Constanze Bach, Andreas Deutschmann-Olek, Sebastian G. Hofer, Sungkun Hong, Nikolai Kiesel, Andreas Kugi, and Markus Aspelmeyer. "Real-time optimal quantum control of mechanical motion at room temperature." In: *Nature* 595.7867 (2021), pp. 373–377. ISSN: 1476-4687. DOI: 10.1038/s41586-021-03602-3. URL: https://doi.org/10.1038/s41586-021-03602-3.

[82] Daniel Malz, Johannes Knolle, and Andreas Nunnenkamp. "Topological magnon amplification." In: *Nature Communications* 10.1 (2019), p. 3937. ISSN: 2041-1723. DOI: 10.1038/s41467-019-11914-2. URL: https://doi.org/10.1038/s41467-019-11914-2.

[83] P. Maunz, T. Puppe, I. Schuster, N. Syassen, P. W. H. Pinkse, and G. Rempe. "Cavity cooling of a single atom." In: *Nature* 428.6978 (2004), pp. 50–52. ISSN: 1476-4687. DOI: 10.1038/nature02387. URL: https://doi.org/10.1038/nature02387.

[84] A. Metelmann and A. A. Clerk. "Nonreciprocal Photon Transmission and Amplification via Reservoir Engineering." In: *PRX* 5.2 (June 2015), p. 021025. DOI: 10.1103/PhysRevX.5.021025. URL: https://link.aps.org/doi/10.1103/PhysRevX.5.021025.

[85] Nadine Meyer, Andrés de los Rios Sommer, Pau Mestres, Jan Gieseler, Vijay Jain, Lukas Novotny, and Romain Quidant. "Resolved-Sideband Cooling of a Levitated Nanoparticle in the Presence of Laser Phase Noise." In: *Phys. Rev. Lett.* 123 (15 Oct. 2019), p. 153601. DOI: 10.1103/PhysRevLett.123.153601. URL: https://link.aps.org/doi/10.1103/PhysRevLett.123.153601.

[86] J. Millen, T. Deesuwan, P. Barker, and J. Anders. "Nanoscale temperature measurements using non-equilibrium Brownian dynamics of a levitated nanosphere." In: *Nature Nanotechnology* 9 (May 2014), p. 425. URL: https://doi.org/10.1038/nnano.2014.82.

[87] J. Millen, P. Z. G. Fonseca, T. Mavrogordatos, T. S. Monteiro, and P. F. Barker. "Cavity Cooling a Single Charged Levitated Nanosphere." In: *Phys. Rev. Lett.* 114 (12 Mar. 2015), p. 123602. DOI: 10.1103/PhysRevLett.114.123602. URL: https://link.aps.org/doi/10.1103/PhysRevLett.114.123602.

[88] Fernando Monteiro, Gadi Afek, Daniel Carney, Gordan Krnjaic, Jiaxiang Wang, and David C. Moore. "Search for Composite Dark Matter with Optically Levitated Sensors." In: *Phys. Rev. Lett.* 125 (18 Oct. 2020), p. 181102. DOI: 10.1103/PhysRevLett.125.181102. URL: https://link.aps.org/doi/10.1103/PhysRevLett.125.181102.

[89] David C Moore and Andrew A Geraci. "Searching for new physics using optically levitated sensors." In: *Quantum Science and Technology* 6.1 (Jan. 2021), p. 014008. DOI: 10.1088/2058-9565/abcf8a. URL: https://doi.org/10.1088/2058-9565/abcf8a.

[90] David C. Moore, Alexander D. Rider, and Giorgio Gratta. "Search for Millicharged Particles Using Optically Levitated Microspheres." In: *Phys. Rev. Lett.* 113 (25 Dec. 2014), p. 251801. DOI: 10.1103/PhysRevLett.113.251801. URL: https://link.aps.org/doi/10.1103/PhysRevLett.113.251801.

[91] Kater W. Murch, Kevin L. Moore, Subhadeep Gupta, and Dan M. Stamper-Kurn. "Observation of quantum-measurement backaction with an ultracold atomic gas." In: *Nature Physics* 4.7 (2008), pp. 561–564. ISSN: 1745-2481. DOI: 10.1038/nphys965. URL: https://doi.org/10.1038/nphys965.

[92] Lukas Novotny and Bert Hecht. *Principles of Nano-Optics*. 2nd ed. Cambridge: Cambridge University Press, 2012. DOI: 10.1017/CBO9780511794193. URL: https://www.cambridge.org/core/product/E884E5F4AA76DF179A1ECFDF77436452.

[93] Stefan Nußmann, Karim Murr, Markus Hijlkema, Bernhard Weber, Axel Kuhn, and Gerhard Rempe. "Vacuum-stimulated cooling of single atoms in three dimensions." In: *Nature Physics* 1.2 (2005), pp. 122–125. ISSN: 1745-2481. DOI: 10.1038/nphys120. URL: https://doi.org/10.1038/nphys120.

[94] A. Omran et al. "Generation and manipulation of Schrödinger cat states in Rydberg atom arrays." In: *Science* 365.6453 (Aug. 2019), pp. 570–574. DOI: 10.1126/science.aax9743. URL: https://doi.org/10.1126/science.aax9743.

[95] A. D. O'Connell et al. "Quantum ground state and single-phonon control of a mechanical resonator." In: *Nature* 464.7289 (2010), pp. 697–703. ISSN: 1476-4687. DOI: 10.1038/nature08967. URL: https://doi.org/10.1038/nature08967.

[96] Yogesh S. S. Patil, Judith Höller, Parker A. Henry, Chitres Guria, Yiming Zhang, Luyao Jiang, Nenad Kralj, Nicholas Read, and Jack G. E. Harris. "Measuring the knot of non-Hermitian degeneracies and non-commuting braids." In: *Nature* 607.7918 (2022), pp. 271–275. ISSN: 1476-4687. DOI: 10.1038/s41586-022-04796-w. URL: https://doi.org/10.1038/s41586-022-04796-w.

[97] V. Peano, C. Brendel, M. Schmidt, and F. Marquardt. "Topological Phases of Sound and Light." In: *Phys. Rev. X* 5 (3 July 2015), p. 031011. DOI: 10.1103/PhysRevX.5.031011. URL: https://link.aps.org/doi/10.1103/PhysRevX.5.031011.

[98] Vittorio Peano, Martin Houde, Florian Marquardt, and Aashish A. Clerk. "Topological Quantum Fluctuations and Traveling Wave Amplifiers." In: *Phys. Rev. X* 6 (4 Nov. 2016), p. 041026. DOI: 10.1103/PhysRevX.6.041026. URL: https://link.aps.org/doi/10.1103/PhysRevX.6.041026.

[99] Johannes Piotrowski, Dominik Windey, Jayadev Vijayan, Carlos Gonzalez-Ballestero, Andrés de los Ríos Sommer, Nadine Meyer, Romain Quidant, Oriol Romero-Isart, René Reimann, and Lukas Novotny. "Simultaneous ground-state cooling of two mechanical modes of a levitated nanoparticle." In: *Nature Physics* 19.7 (2023), pp. 1009–1013. ISSN: 1745-2481. DOI: 10.1038/s41567-023-01956-1. URL: https://doi.org/10.1038/s41567-023-01956-1.

[100] Paolo Polimeno et al. "Optical tweezers and their applications." In: *Journal of Quantitative Spectroscopy and Radiative Transfer* 218 (2018), pp. 131–150. ISSN: 0022-4073. DOI: 10.1016/j.jqsrt.

2018.07.013. URL: https://www.sciencedirect.com/science/article/pii/S002240731830445X.

[101] Diego Porras and Samuel Fernández-Lorenzo. "Topological Amplification in Photonic Lattices." In: *PRL* 122.14 (Apr. 2019), p. 143901. DOI: 10.1103/PhysRevLett.122.143901. URL: https://link.aps.org/doi/10.1103/PhysRevLett.122.143901.

[102] P. Rabl, C. Genes, K. Hammerer, and M. Aspelmeyer. "Phase-noise induced limitations on cooling and coherent evolution in optomechanical systems." In: *Phys. Rev. A* 80 (6 Dec. 2009), p. 063819. DOI: 10.1103/PhysRevA.80.063819. URL: https://link.aps.org/doi/10.1103/PhysRevA.80.063819.

[103] A. Ranfagni, K. Børkje, F. Marino, and F. Marin. "Two-dimensional quantum motion of a levitated nanosphere." In: *Phys. Rev. Res.* 4 (3 July 2022), p. 033051. DOI: 10.1103/PhysRevResearch.4.033051. URL: https://link.aps.org/doi/10.1103/PhysRevResearch.4.033051.

[104] Muddassar Rashid, Tommaso Tufarelli, James Bateman, Jamie Vovrosh, David Hempston, M. S. Kim, and Hendrik Ulbricht. "Experimental Realization of a Thermal Squeezed State of Levitated Optomechanics." In: *Phys. Rev. Lett.* 117 (27 Dec. 2016), p. 273601. DOI: 10.1103/PhysRevLett.117.273601. URL: https://link.aps.org/doi/10.1103/PhysRevLett.117.273601.

[105] Manuel Reisenbauer, Henning Rudolph, Livia Egyed, Klaus Hornberger, Anton V. Zasedatelev, Murad Abuzarli, Benjamin A. Stickler, and Uroš Delić. "Non-Hermitian dynamics and non-reciprocity of optically coupled nanoparticles." In: *Nature Physics* 20.10 (2024), pp. 1629–1635. ISSN: 1745-2481. DOI: 10.1038/s41567-024-02589-8. URL: https://doi.org/10.1038/s41567-024-02589-8.

[106] F. Ricci, R. A. Rica, M. Spasenović, J. Gieseler, L. Rondin, L. Novotny, and R. Quidant. "Optically levitated nanoparticle as a model system for stochastic bistable dynamics." In: *Nature Communications* 8.1 (2017), p. 15141. ISSN: 2041-1723. DOI: 10.1038/ncomms15141. URL: https://doi.org/10.1038/ncomms15141.

[107] Jakob Rieser, Mario A. Ciampini, Henning Rudolph, Nikolai Kiesel, Klaus Hornberger, Benjamin A. Stickler, Markus Aspelmeyer, and Uroš Delić. "Tunable light-induced dipole-dipole interaction between optically levitated nanoparticles." In: *Science* 377.6609 (Aug. 2022), pp. 987–990. DOI: 10.1126/science.abp9941. URL: https://doi.org/10.1126/science.abp9941.

[108] B. Rodenburg, L. P. Neukirch, A. N. Vamivakas, and M. Bhattacharya. "Quantum model of cooling and force sensing with an optically trapped nanoparticle." In: *Optica* 3.3 (2016), pp. 318–323. DOI: 10.1364/OPTICA.3.000318. URL: https://opg.optica.org/optica/abstract.cfm?URI=optica-3-3-318.

[109] O. Romero-Isart, A. C. Pflanzer, F. Blaser, R. Kaltenbaek, N. Kiesel, M. Aspelmeyer, and J. I. Cirac. "Large Quantum Superpositions and Interference of Massive Nanometer-Sized Objects." In: *Phys. Rev. Lett.* 107 (2 July 2011), p. 020405. DOI: 10.1103/PhysRevLett.107.020405. URL: https://link.aps.org/doi/10.1103/PhysRevLett.107.020405.

[110] Henning Rudolph, Uroš Delić, Klaus Hornberger, and Benjamin A. Stickler. "Quantum Optical Binding of Nanoscale Particles." In: *PRL* 133.23 (Dec. 2024), p. 233603. DOI: 10.1103/PhysRevLett.133.233603. URL: https://link.aps.org/doi/10.1103/PhysRevLett.133.233603.

[111] Henning Rudolph, Uroš Delić, Klaus Hornberger, and Benjamin A. Stickler. "Quantum theory of non-Hermitian optical binding between nanoparticles." In: *PRA* 110.6 (Dec. 2024), p. 063507. DOI: 10.1103/PhysRevA.110.063507. URL: https://link.aps.org/doi/10.1103/PhysRevA.110.063507.

[112] Henning Rudolph, Klaus Hornberger, and Benjamin A. Stickler. "Entangling levitated nanoparticles by coherent scattering." In: *Phys. Rev. A* 101 (1 Jan. 2020), p. 011804. DOI: 10.1103/PhysRevA.101.011804. URL: https://link.aps.org/doi/10.1103/PhysRevA.101.011804.

[113] Amir H Safavi-Naeini, Jasper Chan, Jeff T Hill, Simon Gröblacher, Haixing Miao, Yanbei Chen, Markus Aspelmeyer, and Oskar Painter. "Laser noise in cavity-optomechanical cooling and thermometry." In: *New Journal of Physics* 15.3 (2013), p. 035007. URL: http://stacks.iop.org/1367-2630/15/i=3/a=035007.

[114] Marc Sansa et al. "Optomechanical mass spectrometry." In: *Nature Communications* 11.1 (2020), p. 3781. ISSN: 2041-1723. DOI: 10.1038/s41467-020-17592-9. URL: https://doi.org/10.1038/s41467-020-17592-9.

[115] T. A. Savard, K. M. O'Hara, and J. E. Thomas. "Laser-noise-induced heating in far-off resonance optical traps." In: *Phys. Rev. A* 56 (2 Aug. 1997), R1095–R1098. DOI: 10.1103/PhysRevA.56.R1095. URL: https://link.aps.org/doi/10.1103/PhysRevA.56.R1095.

[116] A. Schliesser, G. Anetsberger, R. Rivière, O. Arcizet, and T. J. Kippenberg. "High-sensitivity monitoring of micromechanical vibration using optical whispering gallery mode resonators." In: *New Journal of Physics* 10.9 (2008), p. 095015. DOI: 10.1088/

1367-2630/10/9/095015. URL: https://dx.doi.org/10.1088/1367-2630/10/9/095015.

[117] Sandeep Sharma, A. Kani, and M. Bhattacharya. "$\mathcal{PT}$ symmetry, induced mechanical lasing, and tunable force sensing in a coupled-mode optically levitated nanoparticle." In: *PRA* 105.4 (Apr. 2022), p. 043505. DOI: 10.1103/PhysRevA.105.043505. URL: https://link.aps.org/doi/10.1103/PhysRevA.105.043505.

[118] Wolfgang Singer, Manfred Frick, Stefan Bernet, and Monika Ritsch-Marte. "Self-organized array of regularly spaced microbeads in a fiber-optical trap." In: *J. Opt. Soc. Am. B* 20.7 (July 2003), pp. 1568–1574. DOI: 10.1364/JOSAB.20.001568. URL: https://opg.optica.org/josab/abstract.cfm?URI=josab-20-7-1568.

[119] Vojtěch Svak, Jana Flajšmanová, Lukáš Chvátal, Martin Šiler, Alexandr Jonáš, Jan Ježek, Stephen H. Simpson, Pavel Zemánek, and Oto Brzobohatý. "Stochastic dynamics of optically bound matter levitated in vacuum." In: *Optica* 8.2 (Feb. 2021), pp. 220–229. DOI: 10.1364/OPTICA.404851. URL: https://opg.optica.org/optica/abstract.cfm?URI=optica-8-2-220.

[120] S. A. Tatarkova, A. E. Carruthers, and K. Dholakia. "One-Dimensional Optically Bound Arrays of Microscopic Particles." In: *Phys. Rev. Lett.* 89 (28 Dec. 2002), p. 283901. DOI: 10.1103/PhysRevLett.89.283901. URL: https://link.aps.org/doi/10.1103/PhysRevLett.89.283901.

[121] Felix Tebbenjohanns, Martin Frimmer, and Lukas Novotny. "Optimal position detection of a dipolar scatterer in a focused field." In: *Phys. Rev. A* 100 (4 Oct. 2019), p. 043821. DOI: 10.1103/PhysRevA.100.043821. URL: https://link.aps.org/doi/10.1103/PhysRevA.100.043821.

[122] Felix Tebbenjohanns, M. Luisa Mattana, Massimiliano Rossi, Martin Frimmer, and Lukas Novotny. "Quantum control of a nanoparticle optically levitated in cryogenic free space." In: *Nature* 595.7867 (2021), pp. 378–382. ISSN: 1476-4687. DOI: 10.1038/s41586-021-03617-w. URL: https://doi.org/10.1038/s41586-021-03617-w.

[123] J. D. Teufel, T. Donner, Dale Li, J. W. Harlow, M. S. Allman, K. Cicak, A. J. Sirois, J. D. Whittaker, K. W. Lehnert, and R. W. Simmonds. "Sideband cooling of micromechanical motion to the quantum ground state." In: *Nature* 475.7356 (2011), pp. 359–363. ISSN: 1476-4687. URL: https://doi.org/10.1038/nature10261.

[124] J. D. Thompson, B. M. Zwickl, A. M. Jayich, Florian Marquardt, S. M. Girvin, and J. G. E. Harris. "Strong dispersive coupling of a high-finesse cavity to a micromechanical membrane." In:

Nature 452.7183 (2008), pp. 72–75. ISSN: 1476-4687. DOI: 10.1038/nature06715. URL: https://doi.org/10.1038/nature06715.

[125] M. Toroš and T. S. Monteiro. "Quantum sensing and cooling in three-dimensional levitated cavity optomechanics." In: *PRRESEARCH* 2.2 (May 2020), p. 023228. DOI: 10.1103/PhysRevResearch.2.023228. URL: https://link.aps.org/doi/10.1103/PhysRevResearch.2.023228.

[126] R. Uberna, A. Bratcher, and B. G. Tiemann. "Coherent Polarization Beam Combination." In: *IEEE Journal of Quantum Electronics* 46.8 (Aug. 2010), pp. 1191–1196. DOI: 10.1109/JQE.2010.2044976.

[127] Jayadev Vijayan, Johannes Piotrowski, Carlos Gonzalez-Ballestero, Kevin Weber, Oriol Romero-Isart, and Lukas Novotny. "Cavity-mediated long-range interactions in levitated optomechanics." In: *Nature Physics* 20.5 (2024), pp. 859–864. ISSN: 1745-2481. DOI: 10.1038/s41567-024-02405-3. URL: https://doi.org/10.1038/s41567-024-02405-3.

[128] Jayadev Vijayan, Zhao Zhang, Johannes Piotrowski, Dominik Windey, Fons van der Laan, Martin Frimmer, and Lukas Novotny. "Scalable all-optical cold damping of levitated nanoparticles." In: *Nature Nanotechnology* 18.1 (2023), pp. 49–54. ISSN: 1748-3395. DOI: 10.1038/s41565-022-01254-6. URL: https://doi.org/10.1038/s41565-022-01254-6.

[129] Giovanni Volpe et al. "Roadmap for optical tweezers." In: *Journal of Physics: Photonics* 5.2 (Apr. 2023), p. 022501. DOI: 10.1088/2515-7647/acb57b. URL: https://doi.org/10.1088/2515-7647/acb57b.

[130] Vladan Vuletić, Hilton W. Chan, and Adam T. Black. "Three-dimensional cavity Doppler cooling and cavity sideband cooling by coherent scattering." In: *Phys. Rev. A* 64 (3 Aug. 2001), p. 033405. DOI: 10.1103/PhysRevA.64.033405. URL: https://link.aps.org/doi/10.1103/PhysRevA.64.033405.

[131] Vladan Vuletić and Steven Chu. "Laser Cooling of Atoms, Ions, or Molecules by Coherent Scattering." In: *PRL* 84.17 (Apr. 2000), pp. 3787–3790. DOI: 10.1103/PhysRevLett.84.3787. URL: https://link.aps.org/doi/10.1103/PhysRevLett.84.3787.

[132] Gerard J. Milburn Warwick P. Bowen. *Quantum Optomechanics*. 1st ed. CRC Press, 2015. ISBN: 148225915X. DOI: https://doi.org/10.1201/b19379.

[133] Norman Hodgson; Horst Weber. *Laser Resonators and Beam Propagation*. Springer Berlin, Heidelberg, 2005. ISBN: 978-0-387-40078-5. DOI: https://doi.org/10.1007/b106789.

[134] Jan Wiersig. "Prospects and fundamental limits in exceptional point-based sensing." In: *Nature Communications* 11.1 (2020), p. 2454. ISSN: 2041-1723. DOI: 10.1038/s41467-020-16373-8. URL: https://doi.org/10.1038/s41467-020-16373-8.

[135] H. Xu, D. Mason, Luyao Jiang, and J. G. E. Harris. "Topological energy transfer in an optomechanical system with exceptional points." In: *Nature* 537.7618 (2016), pp. 80–83. ISSN: 1476-4687. DOI: 10.1038/nature18604. URL: https://doi.org/10.1038/nature18604.

[136] Haowei Xu, Uroš Delić, Guoqing Wang, Changhao Li, Paola Cappellaro, and Ju Li. "Exponentially Enhanced Non-Hermitian Cooling." In: *PRL* 132.11 (Mar. 2024), p. 110402. DOI: 10.1103/PhysRevLett.132.110402. URL: https://link.aps.org/doi/10.1103/PhysRevLett.132.110402.

[137] André Xuereb, Claudiu Genes, and Aurélien Dantan. "Strong Coupling and Long-Range Collective Interactions in Optomechanical Arrays." In: *Phys. Rev. Lett.* 109 (22 Nov. 2012), p. 223601. DOI: 10.1103/PhysRevLett.109.223601. URL: https://link.aps.org/doi/10.1103/PhysRevLett.109.223601.

[138] Jiangwei Yan, Xudong Yu, Zheng Vitto Han, Tongcang Li, and Jing Zhang. "On-demand assembly of optically levitated nanoparticle arrays in vacuum." In: *Photonics Research* 11.4 (2023). Photonics Research, p. 600. DOI: 10.1364/PRJ.471547. URL: https://opg.optica.org/prj/abstract.cfm?URI=prj-11-4-600.

[139] Jing Zhang, Bo Peng, Şahin Kaya Özdemir, Kevin Pichler, Dmitry O. Krimer, Guangming Zhao, Franco Nori, Yu-xi Liu, Stefan Rotter, and Lan Yang. "A phonon laser operating at an exceptional point." In: *Nature Photonics* 12.8 (2018), pp. 479–484. ISSN: 1749-4893. DOI: 10.1038/s41566-018-0213-5. URL: https://doi.org/10.1038/s41566-018-0213-5.

[140] Lei-Ming Zhou, Ke-Wen Xiao, Jun Chen, and Nan Zhao. "Optical levitation of nanodiamonds by doughnut beams in vacuum." In: *Laser & Photonics Reviews* 11.2 (Mar. 2017), p. 1600284. ISSN: 1863-8880. DOI: 10.1002/lpor.201600284. URL: https://doi.org/10.1002/lpor.201600284.